Quantitative PET Imaging with Hybrid MR-PET Scanners

Von der Fakultät für Mathematik, Informatik und Naturwissenschaften der RWTH Aachen University zur Erlangung des akademischen Grades eines Doktors der Ingenieurwissenschaften genehmigte Dissertation

vorgelegt von
Dipl.-Ing. Christoph Peter Weirich
aus Trier

Berichter:
Universitätsprofessor Dr. rer. nat. N. Jon Shah
Universitätsprofessor Dr. rer. nat. Achim Stahl
Universitätsprofessor Dr.-Ing. Dirk Heberling

Tag der mündlichen Prüfung: 18. März 2014

Diese Dissertation ist auf den Internetseiten der Hochschulbibliothek online verfügbar.

Kurzfassung

Diese Arbeit behandelt die quantitative PET Bildgebung mit MR-PET Hybridtomographen. Dabei wurden verschiedene Korrekturverfahren zur Quantifizierung und zur Verbesserung der Bildqualität entwickelt und implementiert. Verfahren, die bereits verfügbar waren, wurden angepasst und optimiert. Eine Implementierung der Korrekturen zusammen mit der Bildrekonstruktion und anschließender Bildkalibrierung wurden für die 3T und 9,4T MR-BrainPET Hybridtomografen bereitgestellt. Eine detaillierte Evaluierung der Korrekturen sowie die quantitative Bewertung des Gesamtverfahrens wurden durchgeführt. Damit ist die Quantifizierung der PET-Bilder in Phantomstudien und letztlich auch Humanstudien mit simultanem MR-PET möglich.

Abstract

This work deals with the quantification of PET images with the new hybrid imaging technology of MR-PET. Data correction methods have been developed and implemented, allowing for quantification and improvement in image quality. Procedures already available have been adapted and optimised. An implementation of the correction procedures together with the image reconstruction and the calibration is provided for the 3T and 9.4T MR-BrainPET hybrid scanners. A detailed evaluation of the correction procedures as well as the quantification of the entire workflow have been performed. With this, quantitative PET imaging in phantom studies and also in human studies with simultaneous MR-PET is possible.

Contents

List of Figures

List of Tables

1. Introduction

Positron emission tomography (PET) is a powerful non-invasive imaging modality in nuclear medicine. It allows quantitative imaging of biochemical processes *in vivo*. Applying the tracer principle, PET offers the advantage of bio-compatible tracers and the relatively short half life of the positron emitting isotopes. Combined with the unchallenged sensitivity of PET scanners and the availability of correction methods for physical effects and measurement imperfections, a excellent image quality and quantification as well as a low radiation dose for the patient can be achieved. Quantitative PET refers to the accurate spatial and temporal representation of the radioactivity distribution within the subject. This includes image homogeneity within the entire field of view and quantitative accuracy for all measured activity concentrations. The knowledge of accuracy and limitations of the measurement are also crucial. A second aspect of quantitative PET is the modelling and quantification of metabolic processes to parametric images, which is, however, beyond the focus of this work [19].
Although PET shows metabolic processes in detail, it is often demanding to assign these findings to the corresponding anatomical structures, especially when highly specific tracers are applied. Therefore, the use of complementary anatomical imaging such as x-ray computed tomography (CT) is highly desirable. Today, the combination of CT with PET is clinically established [100]. However, a drawback of combining PET and CT is the additional radiation dose of the CT scan, particularly for children and young adults. Furthermore, the soft-tissue contrast of CT images is limited, compared to magnetic resonance imaging (MRI). Besides various anatomical contrasts MRI provides functional information, such as perfusion, diffusion, spectroscopy, angiography, and brain activity. A combination of PET and MRI offers many advantages in pre-clinical research and clinical applications, especially in neuroscience. In contrast to PET/CT, where the image volumes are acquired sequentially, an integrated hybrid PET/MR allows the simultaneous acquisition of the same volume, for instance the human brain. A second effect is the potential shortening of the measurement time, compared to the approach with subsequent scans. Although preferable, the integration of PET and MRI in

one system is technologically challenging. Mutual interference of both systems has to be minimised. Dedicated MR compatible PET detector technology and proper shielding have to be used in order to avoid electromagnetic interaction. Furthermore, the information needed for photon attenuation correction, which is derived from transmission scans in standalone PET imaging or from CT scans in PET/CT imaging, has to be derived from the MR images in hybrid PET/MR [39].
In 2008, a hybrid MR-BrainPET scanner developed by Siemens Healthcare for human application has been delivered to the Forschungszentrum Jülich. The BrainPET component offers a high image resolution [37] and is especially advantageous in this respect compared to whole body scanners. By combining versatile MR imaging with imaging of PET tracers the BrainPET allows for a detailed analysis of, for example, brain tumours and of neuro-degenereative disorders, such as Alzheimer's disease, Parkinson's disease and others. The aim of this work is the quantification of PET images acquired with the simultaneously measuring MR-BrainPET which was not guaranteed by the manufacturer of the scanner. The quantitatively accurate representation of activity concentration in the image has to be achieved within the entire field of view of the PET scanner. Dynamic effects at variable countrates and activity distributions within the scanner have to be described and corrected. Furthermore, the new aspect of MRI interference on PET imaging has to be considered. The entire imaging process has to be evaluated regarding the quantitative accuracy. All these procedures are implemented in a workflow, routinely applicable for human studies.
In this work, Chapter 2 provides a short introduction of the principles of PET and Chapter 3 gives an introduction on MR imaging. The upcoming research on hybrid MR-PET imaging is introduced in Chapter 4. Besides, the hybrid MR-BrainPET scanner is presented and characterised. Methods have been designed in order to characterise the interference of simultaneous MRI on PET images. In Chapter 5, the design, optimisation and evaluation of methods and procedures for quantification of PET images are described. Tools for scatter simulation and image reconstruction, which are vendor provided, have been evaluated and included in the procedure. The tools for deadtime and pileup-correction have been envolved and combined with the component-based normalisation. Moreover, a correction method for the MRI interference of certain MR sequences on PET imaging has been developed and implemented. The complex interplay of methods is described in the section "Workflow and Implementation". Chapter 6 includes the evaluation of the overall image quality and quantification accuracy in different phantom studies applying several isotopes. The long term system stability is examined to ensure

comparability of images in studies with a duration of weeks and months. The application of the entire procedure on simultaneous MR-PET studies on human subjects is evaluated in Chapter 6.2, where examples from clinical human studies performed with the 3T MR-BrainPET are demonstrated. The discussion of the presented results is given in Chapter 7, followed by the conclusions and outlook on future developments in Chapter 8.

2. Basics of Positron Emission Tomography

During the last four decades nuclear medicine technology has developed different devices for molecular imaging. Molecules are labelled with a radionuclide and administered to the patient for the visualization of normal and diseased metabolism and physiology. The decaying atomic nuclei emit - possibly after intermediate steps - high energy photons. These photons are recorded by dedicated detector systems and processed to two or three dimensional images showing the distribution of the labelled molecules within the patient. Depending on the decay mode, different instruments are available. Gamma cameras allow for 2D planar scintigraphy, whereas Single Photon Emission Computed Tomography (SPECT) and PET provide 3D tomographic images. Besides imaging of the spatial radiotracer distribution, temporal dynamic of tracer uptake can be evaluated as a parameter.

2.1. Historical Overview

The beginning of radionuclide imaging goes back to the 1940s when a scanner for point-wise rectilinear sampling of a defined matrix was introduced. In 1953, the gamma camera, or Anger scintillation camera, was described and is still the basis of modern gamma cameras and SPECT systems. First suggestions towards PET and SPECT were made in the 1960s by Kuhl and Rankowitz. However, due to insufficient computational power and reconstruction algorithms at that time, its realisation was not achieved until more than a decade later. Nuclear tomographic imaging machines benefited from the improvement of computer systems and the introduction of CT by Cormack and Houndsfield in the 1970s. To realize SPECT, a gamma camera was mounted on a gantry allowing for rotation around the patient. Later on, two or three gamma cameras were used to improve sensitivity. In parallel to the development of SPECT, first PET devices were introduced. PET applies electronic collimation instead of lead collimators, which increases the sensitivity dramatically. A further advantage is the application of bio-compatible

radiotracers with short half lifes, such as water labelled with ^{15}O. Progress in detector technology, data processing and reconstruction procedures have resulted in a continuous quality improvement in nuclear imaging. Advances in detectors and instrumentation technology permit the combination of different imaging modalities. SPECT/CT has been introduced in the early 1990s by Hasegawa et al. [34] and PET/CT in the early 2000s by Townsend et al. [13]. In this way the specific strengths of both, anatomical and functional imaging are combined. Whereas PET/CT and SPECT/CT are already in clinical use, hybrid scanners combining MRI and PET are just being introduced. Even before the introduction of PET/CT, first developments towards combined PET/MRI were done, driven by the idea of resolution enhancement of PET measurements at high magnetic fields [44, 80, 79]. A first hybrid PET-NMR scanner has been realized by Hammer and Christensen [32], followed by a first single slice PET scanner mounted within the RF coil of the MR scanner [92]. Early designs applied a guiding of scintillation light via optical fibres to detectors located outside of the strong static magnetic field. The drawback was a reduced timing and energy resolution of the measured events. However, a first pre-clinical PET/1.5T MR scanner applying this approach was developed [21, 58]. With the development of non-magneto sensitive silicon based photodetectors, integrated hybrid PET/MRI scanners for simultaneous acquisition of PET and MRI became possible. A prototype of integrated PET/MRI small animal scanners combining a 7T MRI and a PET insert has been realised [74]. Furthermore, designs applying the fast SiPMs in pre-clinical MR-PET have also been presented and realised [90, 108]. Also the possibilities of RF shielding have been steadily improved [27].

The first human hybrid MR-PET scanner constructed by Siemens consisted of a prototype of a dedicated head scanner BrainPET and a slightly modified 3T MAGNETOM Tim Trio [30, 88, 16]. Such a prototype was installed at the Forschungszentrum Jülich in 2008 [37], where a second BrainPET detector can be operated within a 9.4 T human MR scanner. Meanwhile, whole body hybrid MR-PET systems are commercially available: The 3T MR scanners combined with a PET scanner are the sequential Philips Ingenuity TF [38] and the simultaneous Siemens mMR [112]. While enhancing the technology of one modality in PET/MRI, it has to be ensured that interference and influences of the complementary modality is kept at a minimum. Currently, the development of hybrid MR-PET instrumentation and methods is an active field in research and engineering [91, 106].

2.2. Physics of PET

2.2.1. Radioactive Decay

Radioactivity of naturally appearing radioisotopes has been discovered by Bequerel in 1896. Thereby an unstable or metastable nucleus transforms into a more stable configuration of protons and neutrons and releases energy by emission of particles and/or radiation. In this process the mass is converted into energy according to Einstein's mass-energy equivalent with conservation of energy, mass, momentum and charge. The sum of rest masses of all particles involved is reduced. Hereby, the transition energy, which corresponds to the energy-equivalent of the difference in rest mass, is often transferred as kinetic energy to emitted particles or is converted into photons. The stability of the nucleus depends on the ratio of the number of neutrons and protons. Spontaneous radioactive decay is a quantum mechanical phenomenon. It can be described statistically by the transition probability of an excited nucleus to a more stable one per time unit. In quantum mechanics it is expressed by the transition amplitude and the decay operator. Furthermore, the nucleus wave functions at the initial state and the final state contribute to this relationship. In general, the decay probability depends on quantum mechanical quantities and is independent of macroscopic quantities, such as temperature, pressure or external fields. Different radioactive decay modes are known and are denominated in temporal order of their discovery α-, β- or γ-decay. The α-radiation consists of a helium nucleus ($^4He^{2+}$) and is rather unimportant in molecular imaging, because of its very limited penetration depth and hazardous interaction with living tissue. The β-decay is subdivided into three different modes.

i) β^--decay, a neutron (n) is converted into a proton (p) by emission of an electron (e^-) and an antineutrino ($\bar{\nu}$);

ii) β^+-decay, a proton is converted into a neutron by emission of a positron (e^+) and a neutrino (ν);

iii) Electron Capture (EC) converts a proton into a neutron by capturing an electron mostly from the inner shell emitting a neutrino;

Whereas β^+ -decay is crucial for PET, EC is a competing decay mode to positron emission and for quantitative PET imaging. The so called branching factor (BF) as the ratio of β^+ modes to the total number of decays corrects for this effect. The existence of the positron has been predicted by Dirac in 1928 and experimentally

proved by Anderson in 1932. The existence of the neutrino has been postulated by Pauli in 1933 already, but the experimental detection has not been realised until 1953. The basic theory of the β-decay has been explained by Fermi in 1934, taking into account the weak interaction, stating that atomic nuclei with a low ratio of neutrons to the sum of neutrons and protons in respect to the nearest stable nucleus are likely to undergo β^+-decay.
For a sample with only one radionuclide, the average decay rate is a specific parameter. The activity and the number of residual radioactive nuclei N in the sample are decreasing exponentially over time. The kinetics of decay is described by

$$\frac{dN}{dt} = -\lambda N, \tag{2.1}$$

leading to

$$N(t) = N(t_0)e^{-\lambda t}, \tag{2.2}$$

$$A(t) = A(t_0)e^{-\lambda t} \quad \text{with} \quad \lambda = \frac{\ln 2}{T_{1/2}}. \tag{2.3}$$

The macroscopic activity concentration $A(t)$ at a certain time t has decreased from the initial activity $A(t_0)$ since the time t_0 according to Equation 2.3. Consequently, the half-life $T_{1/2}$ defines the period of time during which half of the atoms have undergone radioactive decay [22]. Since a decay event occurs spontaneously and independently from other decay events, the actual number of decaying atoms per time unit fluctuates about an expected mean value λ. This is of vital importance in counting experiments, such as PET imaging, especially in short term measurements. The statistics is described by the Poisson distribution, where the probability P for n decay events occurring within a defined time interval Δt is

$$P(n, \Delta t) = \frac{(\lambda \Delta t)^n}{n!} e^{-\lambda \Delta t}. \tag{2.4}$$

with λ again denoting the expected number of decays during the time interval Δt. For an experiment with n detected events, the best estimator can be given as $n \pm \sqrt{n}$, with the uncertainty $\sqrt{n}$ [22].

2.2.2. Interaction of Positrons with Matter

The interaction of charged particles, such as positrons and electrons, differs from that of electromagnetic radiation. Whereas charged particles have a reduced penetration depth compared to uncharged particles (also referred to as non-penetrating

radiation), high energy photons may travel longer distances within tissue and materials (referred to as penetrating radiation). In the following, both types of interaction are described.
The energetic positron is emitted from the nucleus and it may undergo interactions while passing through the surrounding matter and dispensing its kinetic energy. In general, the form of interaction of charged particles with matter depends also on its kinetic energy. A measure for the probability of interaction are the effective cross section σ as an integral of the differential cross section $\frac{d\sigma}{d\Omega}$. The resulting effects for the particle are changes in direction of motion and energy. Basically, four different types of interaction of positrons with matter are distinguished:

- Multiple elastic scattering (Rutherford scattering)
- Ionization, inelastic scattering
- Annihilation
- Bremsstrahlung

The Rutherford scattering of a charged particle in the Coulomb field of the atomic nucleus is an elastic scattering. The cross section for small angles is much higher and the total scattering angle results from the sum of all scatter events during transition of a medium. For a large number of single scatter events, the central limit theorem describes a Gaussian distribution of the angle. In contrast, during inelastic scattering, the charged particle transfers larger fractions of its kinetic energy. In case of positron emission, the positron transfers its energy to the shell electrons of surrounding atoms. As a consequence, the atom is excited or ionized. The mean transfer of energy from a particle transitioning the material is given by the Bethe-Bloch equation. When nearly at rest, the positron and an electron may annihilate immediately or previously form a metastable positronium with a mean lifetime of approximately 10^{-7}s before annihilation. The mass-energy equivalent of the electron-positron system is given by the two rest masses $2m_e$ and is converted into two 511 keV photons (Figure 2.1).
For electron-positron pairs with no kinetic energy the two photons leave the annihilation site back to back due to momentum conservation. In cases, the kinetic energy is finite, so that the angle varies by about $\pm$ 0.5° full-width at half maximum (FWHM) around the ideal angle of 180°. This acollinearity is one physical reason for degradation in image resolution in PET. The cross section of annihilation is low for high kinetic energy and increases after the inelastic scattering of

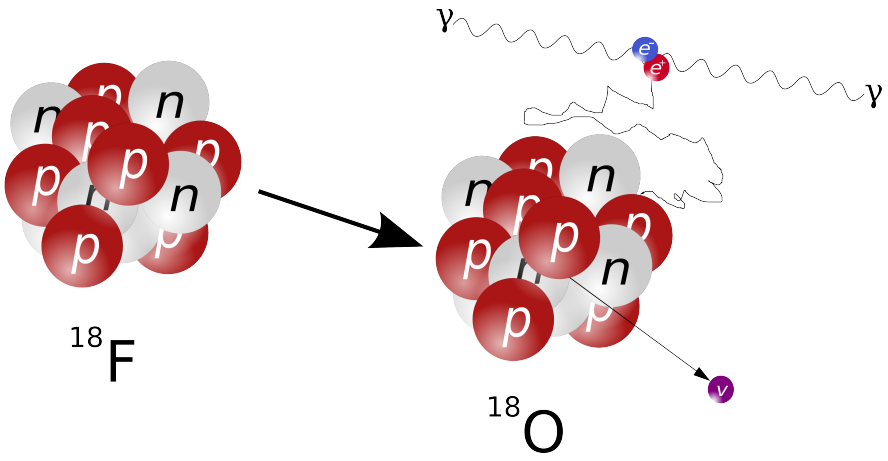

Figure 2.1.: Positron decay of an ^{18}F atom to ^{18}O and annihilation of the emitted positron with an electron.

the positron. This may rupture chemical bindings and thus cause biological hazard to living tissue. Bremsstrahlung does not play a dominant role for standard positron emitters applied in PET. However, Bremsstrahlung affects image quality tremendously, for example imaging the isotope ^{90}Y.

2.2.3. Positron Range

The interactions of ionization, Bremsstrahlung and annihilation limit the physically possible image resolution in PET. The positron range depends on the kinetic energy of the positron and the density of the surrounding matter. Typical mean ranges for PET radio nuclides in water which has similar attenuation properties as soft tissue are given in Table 2.1. The positron range poses a fundamental limit of the achievable image resolution in PET. For positron emitters with a high positron energy and consequently a lower achievable image resolution, the advantages of the application of a strong external magnetic field becomes evident. In this respect ultra high field MR/PET has the potential of improving PET image resolution in image planes perpendicular to the main magnetic field [36, 44], (Figure 2.2).

2.2.4. Non-pure Positron Emitters

A favourable property of standard positron emitters, such as ^{18}F, is their short half life leading to a low radiation dose for the patient. Furthermore, no other high energy photons are emitted during the decay (see Figure 2.3(a)). How-

PET Radionuclides

Nuclide	Half life	Positron Energy	Max. positron range in water	Avg. positron range in water
^{15}O	2.04 min	1740 keV	8.0 mm	1.80 mm
^{11}C	20.39 min	970 keV	3.8 mm	0.85 mm
^{18}F	109.77 min	640 keV	2.2 mm	0.46 mm
^{13}N	9.97 min	1200 keV	5.0 mm	1.15 mm
^{68}Ga	67.63 min	1900 keV	9.0 mm	2.15 mm

Table 2.1.: Main properties of commonly used PET isotopes [76].

ever, for imaging of slow biological processes a longer half life may be desirable. Non-standard positron emitters such as ^{120}I or ^{86}Y with half lifes of 4.2 days and 14 hours, respectively, are available. Also ^{68}Ga is applied in human studies. For quality control, ^{68}Ge/^{68}Ga filled cylinders are used, with a rather complex decay scheme (see Figure 2.3(b)) [95]. A drawback of non-pure positron emitters are additional single photons, emitted practically simultaneously with the positrons, leading to instrumental challenges such as additional detector deadtime and the need for an accurate energy discrimination. The resulting effects may be a reduction of image quality and quantitative accuracy. An unfavourable property of many non-standard positron emitters can be a much larger positron range before annihilation, resulting in a further decrease of image resolution (see Figure 2.2).

2.3. Interactions of Photons with Matter

Annihilation photons escaping from the subject under study are detected by interactions with the detector material. Two mechanisms for interaction of 511 keV photons with matter are relevant for PET, the photoelectric effect and the Compton effect. These effects have to be well understood, since they may compromise the image quality and quantification when they occur within the field of view. On the other hand they are fundamental mechanisms for event detection within the scintillator.

(a) ^{120}I-filled Iida brain phantom at 0 T.

(b) ^{120}I-filled Iida brain phantom at 9.4 T.

(c) ^{18}F-filled Iida brain phantom at 3 T.

Figure 2.2.: Effect of magnetic fields on positron range in reconstructed images. The isotope with a high positron range shows a clear improvement at 9.4 T (b) compared to 0 T (a). Image quality is degraded due to additional gammas of the ^{120}I. The image of the ^{18}F-filled phantom at 3 T is depicted for comparison (c).

2.3.1. Photoelectric Effect

The photoelectric effect describes the absorption of a photon by an atomic bound electron, mostly from an inner K shell and at lower photon energies. The interaction leads to the ejection of the involved electron from the atom while the photon's energy is passed to the electron. Due to the momentum conservation the photoelectric effect can only occur with atomic electrons where the nucleus acts as a third collision partner and takes the recoil momentum. Therefore, the cross section is particularly high for electrons in the inner most K shell due to the proximity to the atomic nucleus. Subsequent to the release of an electron from an inner shell, secondary effects may occur. The missing electron's place may be filled by an electron from an outer shell, leading to a cascade of x-ray emissions with energy of the x-rays as given by Moseley's law. Another form of interaction is the Auger effect where the energy is passed to another electron of the same atom. If that energy is sufficient the electron may escape from the atom [22].

2.3.2. Compton Scatter

Compton scatter is the dominating effect of interaction of photons with energies from 100 keV to 10 MeV with electrons or other charged particles. The scattering

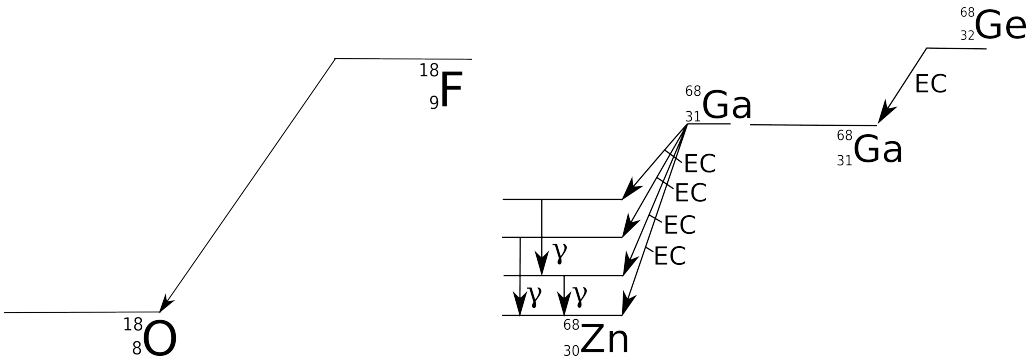

(a) Decay Scheme of ^{18}F (b) Decay Scheme of ^{68}Ge/^{68}Ga

Figure 2.3.: Decay schemes of ^{18}F (a) as a pure positron emitter and ^{68}Ge/^{68}Ga (b) decaying with additional gamma lines.

of 511 keV photon on free or weakly-bound electrons decreases its energy. This process is a strict electron-photon interaction. In contrast to the photoelectric effect, the photon's energy cannot be transferred completely to the electron and a less energetic photon is emitted after the scattering process. The amount of transferred energy depends on the scattering angle of the photon and can be derived from the conservation of energy and momentum. The cross section for the corresponding energies is derived from the Klein-Nishina formula. The main relation between angle and energy, where Θ is the scattering angle and E_γ is the photon energy, is described by the Equations 2.5 and 2.6. When the photon scatters within the subject to scan, this effect is an important source for degradation of contrast in reconstructed PET images. Scattering of the photon within the detector material is the dominating mechanism to determine the position and energy of incidence. Taking into account the different materials, different scatter properties have to be considered. In the living subject, mainly soft tissue and bone have to be distinguished, whereas the MR head coil, the patient bed and other devices may cause, but also absorb scattered events. The energy of the photon $E_\nu^{'}$ and the kinetic energy of the recoil electron $E_e^{'}$ after interaction read

$$E_\gamma^{'}(\Theta) = \frac{E_\gamma}{1 + \frac{E_\gamma}{m_e c^2}(1 - \cos(\Theta))} \tag{2.5}$$

and

$$E_e^{'}(\Theta) = E_\gamma - E_\gamma^{'}(\Theta) = E_\gamma(1 - \frac{1}{1 + \frac{E_\gamma}{m_e c^2}(1 - \cos(\Theta))}, \tag{2.6}$$

respectively. Due to the fact that photons with a larger deflection Θ have lost a higher amount of energy, a larger fraction of scattered photons may be detected by scanners with high energy resolution. Consequently, these events can be excluded.

2.4. PET Instrumentation

A PET scanner is a detection device for photon pairs originating from annihilation events after a β^+-decay. It is applied in medical diagnostics, therapy control and clinical research. The relatively high energy of 511 keV results in low absorption probability in a scanned subject compared to the usually lower-energetic radionuclides used in SPECT. However, due to the lower cross section for interaction with matter the detection of 511 keV photons becomes more challenging. Typically, thousands of crystals are mounted on rings around the subject to determine the moment of incidence, energy and position of one annihilation photon. The detectors are driven in coincidence mode to define a unique crystal combination with fixed geometry, referred to as line of response (LOR) or tube of response (TOR), as drafted in Figure 2.6(a). An annihilation event is detected when two photons with the energy of 511 keV are detected simultaneously by the two detectors. Here, the term simultaneously is defined by the coincidence time window, which is in the range of approximately 3 to 12 ns, depending on the detector technology, the object size and the diameter of the field of view (FOV). The minimal timing window is given by the time that a photon needs to travel along the inner diameter from any point of annihilation to any detector. For time of flight (TOF) PET, the time difference between the detection of the two events can be evaluated in order to render the point of annihilation more precisely [56, 47]. However, this requires different algorithms for image reconstuction and a sophisticated detector technology. In a typical PET scan, millions of coincidence events originating from the decay of the positron emitter are detected, providing information on the projection of the actual tracer distribution. Several hardware components are necessary in order to detect the annihilation photons and acquire coincidence data. The PET instrumentation in combination with the radiotracer principle makes PET a highly sensitive device for metabolic imaging.

2.4.1. Radiotracer Principle

The tracer principle has been introduced in 1912 by de Hevesy and is the most fundamental principle in nuclear medicine [26, 25]. Radioactive elements have

identical chemical properties compared to the non radioactive isotopes. Therefore, they may be used to trace biochemical processes in living subjects. Substances labelled with radionuclides are referred to as radiotracers or radiopharmaceuticals. Usually, one or more stable atoms of a molecule are replaced by an unstable or metastable radioactive analogue. This may be either a radioisotope of the atom (for instance replacement of ^{12}C by ^{11}C in order to generate ^{11}C-glucose) or a chemical analogue (e.g. replacement of hydroxyl group OH by ^{18}F in a glucose analogue). The most widely used PET radionuclides are ^{11}C and ^{18}F with half lifes of 20 min and 109 min, respectively. ^{11}C requires a cyclotron near the site of radiotracer production because of its fast radioactive decay. As an advantage, a short half-life of the radioactive tracer reduces the potentially harmful effects of radiation significantly due to the shorter exposition time. After its administration by injection or inhalation the radiotracer is involved in metabolic processes within the body and allows for functional analysis. The radionuclide within the subject decays and emits gamma photons which may be recorded by the detector. This provides information about the radiotracer's spatial and temporal distribution within the patient's body. Due to the unchallenged sensitivity of nuclear imaging devices, only very low amounts, i.e. tracer amounts, of the labelled molecules need to be administered. Consequently, the metabolic processes are not influenced or disturbed by the radiotracer. The applied positron emitters are produced by a cyclotron which uses a high energy proton beam of usually 4 MeV up to 30 MeV to bombard target atoms, for example ^{18}O for the production of ^{18}F. For clinical studies, the requirements on radiochemistry are rather demanding. Production and quality control of tracers with high purity and specific activity have to be realized, taking into account the short half lifes of PET isotopes (see Table 2.1). In order to achieve clinical relevance, a fast chemistry for synthesis of the radiopharmacon and also a fast quality control have to be realised.
When scanning living subjects the biochemical processes, such as uptake and excretion, lead to additional half lifes, referred to as biological half life, in the specific areas. This is the large field of tracer kinetic modelling. The total half live, however, can be written as

$$\frac{1}{T_h} = \frac{1}{T_{h,biol}} + \frac{1}{T_{h,phys}}. \tag{2.7}$$

The instrumentation treats only the physical half life, while the biological half life is treated by the tracer kinetic modelling. However, for noise considerations and estimations the overall half live is an important figure. In contrast to SPECT,

where ^{99m}Tc is the dominating radiotracer, PET applies mostly biocompatible radiotracers. The short half lifes, which are a infrastructural drawback with regard to the maximal distance to cyclotrons, are advantageous for the patient due to the lower radiation doses.

2.4.2. Scintillators

Most imaging devices in nuclear medicine apply scintillation detectors. Scintillation crystal materials convert high energy photons into photons with a characteristic spectrum in the visible or ultra violet range. This light may than be detected by photodetectors and converted into an electrical signal for further processing. To provide good information about the incident gamma, several scintillator properties are desirable which, however, are partly excluding each other. The dominating properties of clinical detector systems in molecular imaging are sensitivity and localisation accuracy, besides timing properties, energy resolution and costs. Numerous scintillation materials are available with different properties, qualified for different applications (see Table 2.2). Ideally, the number of scintillation photons in a scintillator is directly proportional to the energy deposited in the scintillation material. To assure high sensitivity, a high conversion efficiency of the incident photon energy into scintillation photons is crucial. With increased stopping power of the crystal, more photons at the expected energy range are stopped and cause scintillation light within the crystal. Therefore, the density of the crystal material and the length of the crystal are critical, since longer crystals increase the sensitivity but on the other hand increase the parallax error and reduce the localisation accuracy. Transparency of the crystal to its own scintillation light is relevant to allow for an efficient detection and a high light yield. The dominant effect of interaction between a photon of 511 keV and the crystal lattice is the Compton effect. As described in Section 2.3.2, its probability increases with the material's atomic number. Annihilation photons that undergo Compton scattering within the crystal deposit mostly only a small fraction of their energy at a single interaction. This energy ranges from zero to a maximum value and causes the Compton edge in the spectrum. The scattered annihilation photon, however, may also escape from the crystal. In all cases the absorption process creates an energetic electron which is able to move through the crystal and to interact with other atomic electrons. Finally, it leads to the disposal of scintillation light. A major mechanism for absorption of the photon within the crystal is the photoelectric effect, which becomes more dominant at lower energies, i.e. after single or multiple scatter events of the

photon within the crystal. Here, the photon is completely absorbed depositing all its energy in the crystal. Most likely, this energy is absorbed entirely by the crystal, resulting in the photo peak of the spectrum. In case of incomplete absorption, e.g. the x-ray photon escapes from the crystal without being detected, the assumed photon energy is reduced.

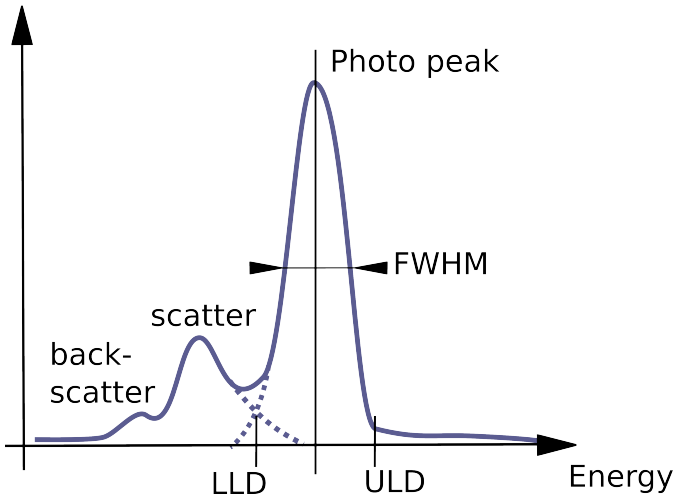

Figure 2.4.: Schematics of a typical energy spectrum in PET. The events found between LLD (lower level discriminator) and ULD (upper level discriminator) are assumed to belong to the photopeak. Events with lower energy are assumed to be scattered and events with higher energy are assumed to have undergone pulse pile-up. Both, scattered and pile-up events are rejected.

Furthermore, the annihilation photon may pass the crystal without any interaction but may be back scattered from the shielding or the glass envelope of the photodetector or the optical coupling. If the scattering angle is relatively high the scattered photon may end up back in the crystal. These photons then have a significantly lower energy and are represented by the backscatter peak of the spectrum (see Figure 2.4). In case when the Compton interactions and the photoelectric absorption occur within the same detector block, the energy of the gamma photon may be computed correctly, otherwise it will be rejected by the electronics. These effects are more likely at corner and edge crystals of detector blocks, manifesting themselves in lower sensitivity [105].
The design and the scanner geometry as well as the scintillator material, size and type of photodetector influence the performance of the scanner essentially.

Different figures of merit direct the optimal application for the scintillator material. A small decay constant of the scintillator is important for timing resolution and thus a high countrate performance. A high light yield and a high linearity is crucial for the energy resolution of the photon, and thus for separation of scattered and unscattered photons (see Figure 2.4). Besides a good geometrical coupling, which is achieved by an optical coupling, the optimal matching of wavelength to the photodetector is important to exploit the functional light output of the crystal and to avoid back reflection into the crystal.
Scintillation material may possess also intrinsic background activity. The today widely used cerium doped lutetium oxy-orthosilicate (Lu_2SiO_5:Ce, LSO:Ce) possesses a background activity due to the natural abundance of ^{176}Lu with 2.6% with approximately 300 Bq/cm^3. LSO produces gamma rays at 89, 202 and 307 keV [60, 61].
Finally, the scintillator has to be selected for the specific application. Important properties of commonly used scintillation materials NaI (sodium iodine), CsI (caeseum iodine), BGO (bismuth germanate), LSO (lutetium oxy-orthosilicate) and LYSO (lutetium yttrium oxy-orthosilicate) are listed in Table 2.2.

PET Scintillator Materials

Material	Density (g/cm^3)	Decay Time (ns)	Photon Yield (keV^{-1})	Peak emission (nm)	Main Application
NaI:Tl	3.6	230	44	415	SPECT
CsI:Tl	4.5	1000	52	540	SPECT
BGO	7.1	300	8	480	PET
LSO:Ce	7.4	40	26	420	PET
LYSO	7.1	41	27	397	PET

Table 2.2.: Scintillator materials with their main properties and the preferred application.

2.4.3. Photodetectors

Photomultiplier The photomultiplier tube (PMT) is a device capable of detection and amplification of very weak light signals. It generates an electric output signal which is proportional to the incoming optical photons. The device is used widely in nuclear medicine and its properties are well known and understood. It

consists of an evacuated glass tube with photocathode, subsequentially arranged dynodes, and an anode. The photocathode is located at the entrance window of the PMT which is optically matched with the scintillation crystals. Photons penetrating the cathode surface eject electrons from the material via the photoelectric effect, where the number of electrons is proportional to the number of incident photons. The conversion efficiency from photons into electrons is referred to as quantum efficiency (QE) or photon detection efficiency (PDE). The amplification of the electric signal is performed by dynodes which are electrodes with a positive voltage relative to the previous stage. Electrons ejected from the photocathode are accelerated towards the first dynode due to the positive voltage of 200 to 400 V. Each electron is then capable of ejecting several secondary electrons from the dynode, resulting in an avalanche effect along the cascade of dynodes, giving an overall amplification factor of 10^4 to 10^7. The electrons reaching the anode produce an amplified current pulse which is proportional to the amount of incoming light. PMTs require a stable high-voltage supply to achieve a stable amplification factor. Since the focusing of the electrons towards the dynodes is sensitive to even low external electro-magnetic fields, PMTs are often shielded for magnetic fields by metal foils. This property makes the PMTs not applicable in integrated hybrid MR-PET scanners [81].

Avalanche Photodiodes Avalanche photodiodes (APD) have been introduced in PET imaging insead of PMTs for the design of hybrid MR-PET scanners. The main advantages are the compact geometry and the non-magneto sensitivity, so that they can be applied within MRI scanners. Furthermore, they require low currents and have a high quantum efficiency (QE) of up to 90 % compared to the 25 % of the PMTs.

The device is a silicon-based semiconductor containing a *pn* junction, which consists of a positively doped p region and a negatively doped n region. These diodes provide an amplification by the generation of electron-hole pairs from an energetic electron resulting in the avalanche effect of electrons in the substrate. Low energetic photons, as produced by the scintillator, enter the diode and pass through the silicon dioxide layer. Depending on the semiconductor material, the sensitivity to the photons depends on the photon's energy. Thus, the scintillator and the APD have to be matched.

The produced electrons travel through the n and p layers before entering the depletion region. In the depletion area free electron-hole pairs are excited, which migrate to cathode and anode, respectively. Applying a reverse bias voltage and

illuminating the crystal junction between the p and n layers, a current proportional to the number of photons incident on the junction is measurable. The design of APDs shows a relatively thin depletion layer, giving rise to a very steep local electrical field across the junction, resulting in a reduced sensitivity to magnetic fields. In operation, high reverse-bias voltages in the range of 500 V are applied across the device. With increasing bias voltage, electrons generated in the p layer continue to increase in energy as they undergo multiple collisions with the crystalline silicon lattice. This avalanche effect of electrons results in electron multiplication similar to the mechanism occurring in one of the dynodes of a PMT, but with relatively low gains between 200 to 1000. Besides the degraded SNR, the APDs have rather poor timing properties.
Another drawback of APDs is the dependency of dark current as a function of the bias voltage. Furthermore, APDs are highly temperature dependent, which may cause stability problems in terms of linearity. As consequence, PET detectors applying APDs have to appropriately control the temperature. Besides, APDs are sources of RF noise and have to be shielded in order to prevent the MR signal from noise pickup [75].

Silicon Photomultiplier Silicon photomultipliers (SiPM) are also silicon-based devices, sensitive to single photons. They consist of APD-arrays operating in Geiger mode on a silicon substrate. With dimensions of each single APD of 20 to 100 μm, a density of 1000 APDs/mm^2 is achieved. The APDs are coupled by silicon quenching resistors. The microcells are read in parallel leading to output signals within a dynamic range from a single photon to 1000 photons/mm^2 of sinsitive area on the device. The supply voltage is APD technology specific and typically varies between 25 V and 90 V, thus being 1 to 2 orders of magnitude lower than the voltage required for traditional PMTs or conventional APDs. With a total QE of about 20 – 30 % and a gain of approximately 10^5 to 10^6, these values are similar to a traditional PMT. In contrast to APDs, the timing jitter of SiPMs is optimised to have a photon arrival time resolution of about 100 ps, making the device capable of TOF. Most important for application in MR-PET systems, the signal parameters are practically independent of external magnetic fields and the small dimensions permit extremely compact and robust mechanical design of detector modules [81, 85, 110]. Drawbacks are here the high dark currents resulting in a certain dark countrate and the limited dynamic range. The possibility of direct coupling of the crystal to the photodetector is advantageous for the image resolution in PET.

Photodetectors in PET

Detector	PMT	APD	SiPM
Dimensions	large	small	small
Amplification	$10^6 - 10^7$	$10^2 - 10^3$	$10^5 - 10^6$
SNR	very high	low	high
QE	20%	60%	30%
Bias Voltage	800-1500 V	100-200 V	25-90 V
MR compatible	no	yes	yes

Table 2.3.: Main properties of the photodetectors PMT, APD and SiPM applied in PET.

2.4.4. Detector Design

The PET detector front-end usually consists of several detector rings, which are mounted around the patient bed. The subunits are panels or cassettes housing the detector blocks with the main components, i.e. scintillation crystal, photodetector and pre-processing electronics.

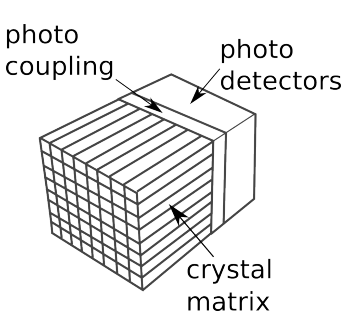

(a) Schematics of a PET detector block.

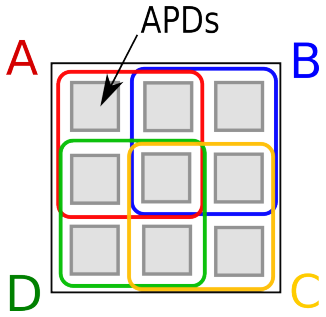

(b) Schematics of the Anger logic of a detector block.

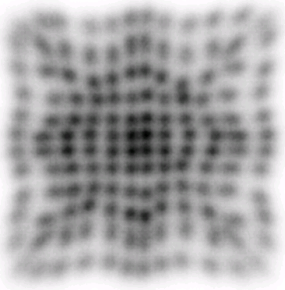

(c) Position profile measured with a detector block of the BrainPET (12 × 12 crystals).

Figure 2.5.: Schematics of a PET detector block with an 8 × 8 crystal array and photo detector (a). Schematics of the Anger logic with a 3 × 3 APD array (b), as applied in the BrainPET. The measured position profile of a detector block (c).

Global parameters that influence the image quality are

- timing resolution,
- energy resolution,
- sensitivity,
- homogeneity and
- capability of processing high countrates.

The output signal of the photodetector is amplified and pre-processed in subsequent steps. The first level of qualification is the determination, whether the temporal integral of the signals exceeds a certain noise level. A threshold is defined which is referred to as the constant fraction discriminator (CFD). An event passing this level is called a CFD single event. The CFD single event's energy is further analysed to be within a defined window between LLD (low level discriminator) and ULD (upper level discriminator). Low energy indicates that the event has undergone Compton scatter and has not been fully absorbed, whereas a high energy indicates a multiple single within a very short time period (pile-up). Only events within the applied energy window are accepted and referred to as energy qualified events. Generally, the number of crystals in a detector block is larger than the number of photodetectors. The Anger logic (Figure 2.5(b)) allows the localisation on the detector crystal and is applied in most SPECT and PET detectors. This logic is based on a weighting scheme of signals originating from the photodetectors. As a result the position of the impinging photon is determined by the ratio of the 4 signals s_i (with $i = A, B, C, D$) see Figure 2.4.4

$$X = \frac{A + D}{E} \text{ and } Y = \frac{A + B}{E}. \tag{2.8}$$

The energy E is the sum of all 4 signals $s_i(t)$ integrated over time according to

$$E = \sum_{i=A,B,C,D} \int_{t_a}^{t_e} s_i(t) dt. \tag{2.9}$$

The position and energy qualified single event is taken into account for coincidence search. In non-ideal detectors, the produced pulses have a finite length during which the detector is not able to accept further events. This effect is referred to as deadtime. Dedicated front-end ASICs (Application Specific Integrated Circuit)

with high countrate performance and low power consumption are applied. Especially if applying temperature dependent APDs and SiPMs, the heat dissipation of the front-end electronics is a concern [108].
The parallax effect is related to the penetration depth and the transfer of photons into adjacent crystals. A photon impinging on a crystal matrix oblique to the photons's propagation path may deposit its energy in more than one crystal, resulting in a wrong assignment of the crystal of incidence. Efforts to increase the spatial resolution result in shorter crystals and block geometries [45]. The combination of smaller crystals with the Anger Logic principle for determination of the photon's position and energy leads to higher probability of mis-assignment of events to crystals.

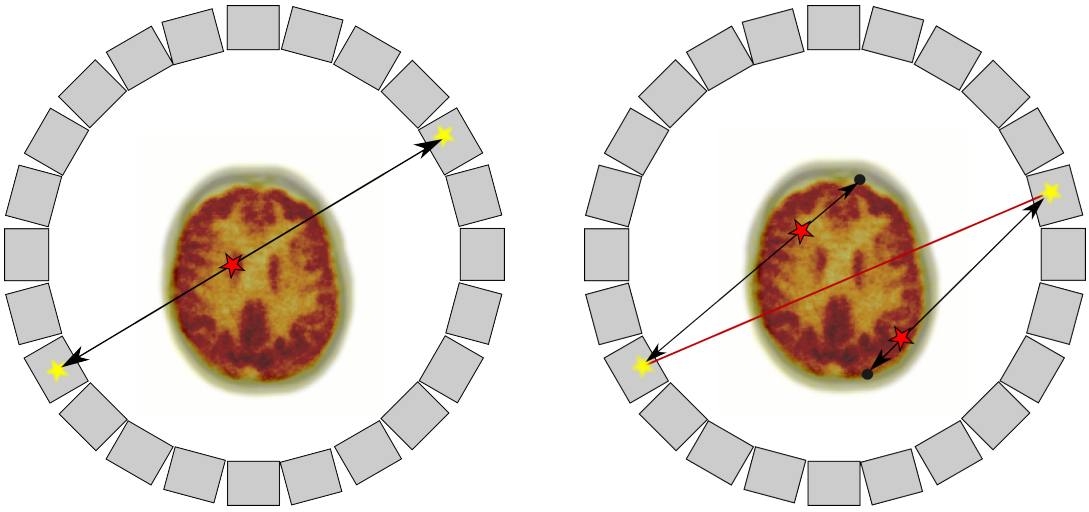

(a) True coincidence detection. (b) Random coincidence detection.

Figure 2.6.: Example of a true (a) and random (b) coincidences.

2.4.5. Coincidence Detection

Passing all these steps of assessment, the energy and position qualified single event is forwarded to the coincidence search. If two qualified singles are detected within the defined timing window, they are assumed to originate from one annihilation event along the LOR between these two detectors (see Figure 2.6(a)). Since the direction of coincidence is well defined and scattered events are assumed to be eliminated, the events are already collimated and no further collimator, as applied

in SPECT, is needed. This aspect is referred to as electronic collimation and increases the PET sensitivity tremendously compared to SPECT. Also 3D PET has a superior sensitivity to 2D PET, where septa are applied between adjacent detector rings. To exploit the high timing resolution of the detector blocks at system level a careful timing calibration has to be performed [3].

2.4.6. Scattered Events and Energy Resolution

Most photons travelling from the point of annihilation towards the detector undergo Compton scattering at material located within the FOV. This may be tissue of the patient himself, i.e. bone or soft-tissue, but may also be devices used, such as the MR RF coil during hybrid MR-PET measurements or shielding (see Figure 2.7(a)). As described in Subsection 2.3.2 the photon loses energy as a function of the scattering angle. In order to accept only photons with reasonable image information, the energy resolution has to be as good as possible. Depending on the energy resolution of the detector, the events with large scattering angles can be rejected. However, a significant fraction of scattered events remains in the acquired data and has to be considered by correction methods.

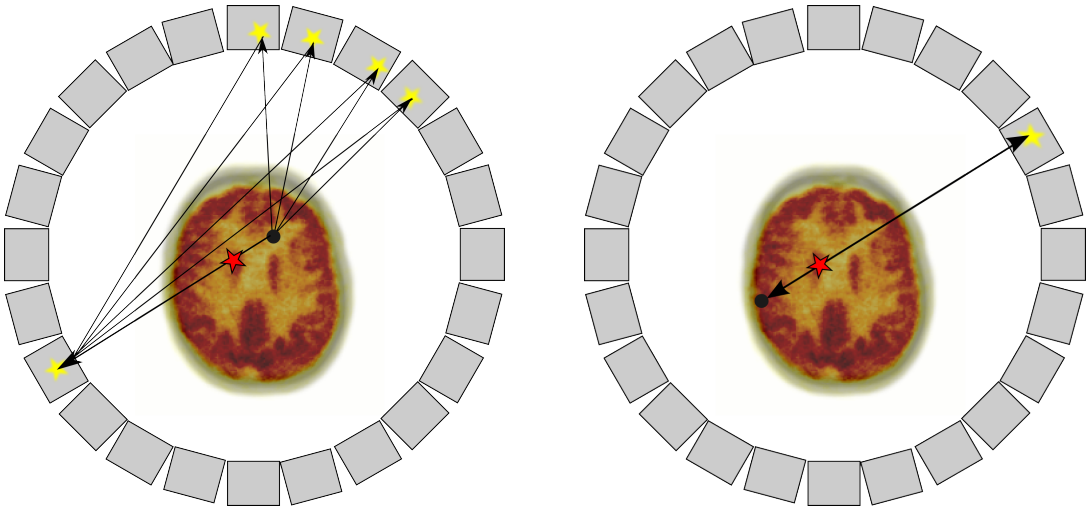

(a) Scattered coincidences.

(b) Effect of photon absorption.

Figure 2.7.: Example of a scattered (a) and an absorbed (b) coincidence. The effect of attenuation is mainly due to scattered coincidences that were not detected in the correct LOR but also, less frequent due to photon absorption.

2.4.7. Random Coincidences

Two qualified single events originating from different annihilation events can be accidentally recorded by the scanner within the defined coincidence window and may be detected as a coincidence. In this case they are denominated as a random coincidence. The random coincidence rate for a specific LOR is related to the product of the single event rates detected by the crystals defining that LOR. Random coincidences occur homogeneously across the FOV and add a homogeneous background folded with the sensitivity to the reconstructed image (see Figure 2.6(b)). This leads to an overestimation of tracer distributions and reduction in image contrast if not corrected appropriately.

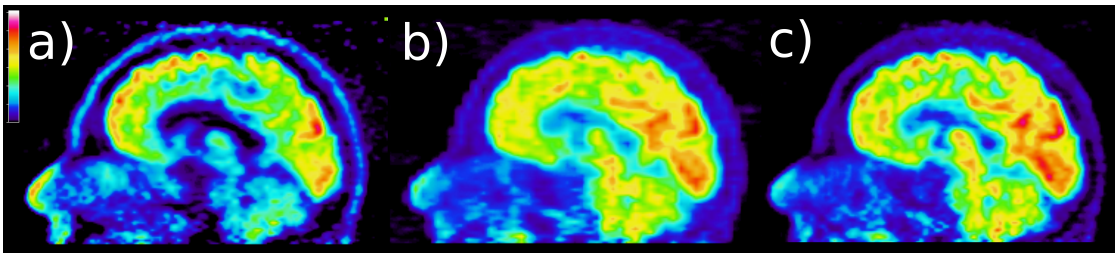

Figure 2.8.: Example of corrections in the reconstructed images. Leftmost image (a) is not corrected for attenuation and scatter, the middle image (b) not corrected for scatter but for attenuation, and the rightmost image (c) is fully corrected. All images are corrected for randoms and normalisation.

2.4.8. Multiple Coincidences

Multiple coincidences are related to random coincidences and occur when more than two qualified singles are detected within the timing window. In this case, the LOR cannot be uniquely determined. Depending on the scanner firmware the treatment may differ. One policy is the definition of the two photons with the highest detected energy as the coincidence. Due to the relatively small likelihood of this event, the scanner may reject all singles involved in a multiple coincidence.

2.4.9. Normalisation

It has to be ensured that all LORs joining detectors in coincidence have the same effective sensitivity. Hereby, variations in the geometric sensitivity as well as the

crystal efficiency have to be compensated. The normalisation accounts for low frequency inhomogeneities in the image, in case of sensitivity gradients along the patient axis as well as high frequency artefacts caused by sentivity patterns among the detector block.

2.4.10. Deadtime and Event Overlap

The deadtime τ is the time that a detector needs to process an incoming event, while no further event can be processed. Assuming that the events do not interfere, the process can be described by the Poisson distribution. With increasing activity, the probability of at least two events occurring within the time period τ increases. When an event cannot be processed because it arrives during the processing time of the previous one, but it does not prolong the deadtime of the detector, the deadtime is assumed as non-paralysable. Increasing the countrate, the actually detected countrate reaches the maximum $1/\tau$ asymptotically. If an impinging event prolongs the deadtime, the actually measured countrate can also decrease with increasing activity. In non-ideal systems the deadtime behaves as a mixture of both special types. However, in modern architectures, the non-paralysable effect dominates at countrates relevant for human studies.

2.5. Data Organisation and Image Reconstruction

2.5.1. Data Organisation of the BrainPET Scanner

As described earlier, a coincidence event is an event in one LOR connecting two detector crystals. The geometric properties of an LOR can be defined by radial offset r, view angle ϕ in 2D, and in 3D additionally by the axial offset z, and azimuthal angle θ of a defined coordinate system relative to the scanner.

LOR Histogram The LOR histogram is a data format for the temporally integrated coincidences measured in every crystal combination. Consequently, the bins for the combination of detector heads can be respresented as headpairs (see Figure 2.9). It contains spatially uncompressed data and is the basis for LOR reconstruction [86, 46], avoiding additional loss of information due to sinogram binning and compression.

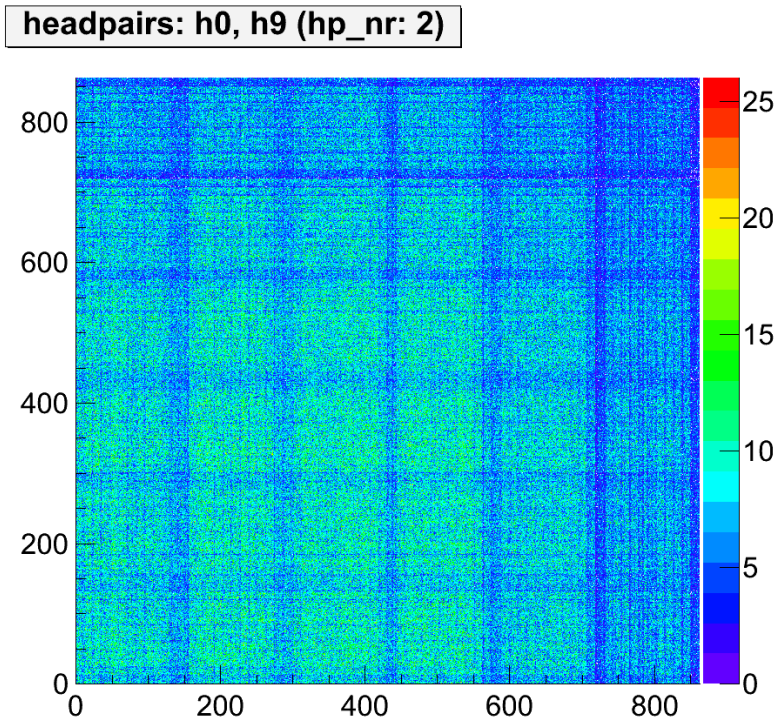

Figure 2.9.: LOR histogram: Illustration of one of the 304 headpairs. Here the coincidences measured in the crystal combinations of all 864 crystals of head 0 with all 864 crystals with the oblique opposed head 9 are displayed. The structure of the 6×6 blocks is visible.

Hitmap A detector hitmap contains the counts for every single crystal on the detector. For prompts or delayeds coincidence hitmaps (PCMAP or DCMAP, respectively) the bin value for each of the two crystals involved in a coincidence is increased by one. Usually, these maps are considered for daily Quality Control (dailyQC) purposes. The DCMAP is also the basis for variance reduction on randoms, as described later. Figure 2.10 contains the measured prompt coincidences from a point source. The unrolled BrainPET detector map represents the 32 cassettes with each 6 detector blocks, containing a 12×12 crystal matrix.

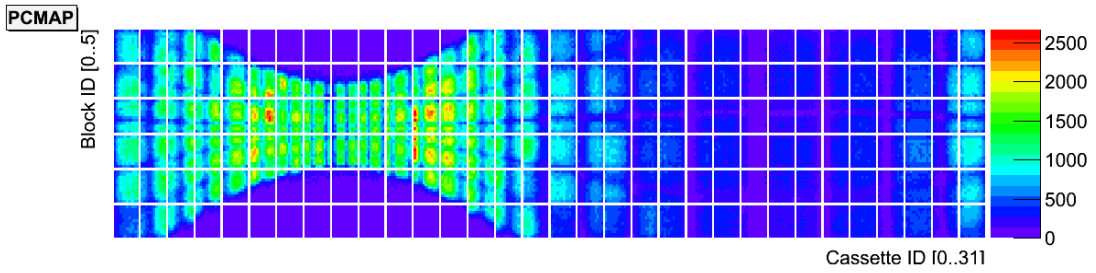

Figure 2.10.: Detector hitmap of the BrainPET scanner. The map shows the unrolled detector map with its 32 cassettes, containing 6 blocks each, with a 12×12 LSO-crystal matrix. The data represent an off-centre positioned point source.

Sinogram The widely used sinogram is a compressed data format for coincidence data, which can be used directly for image reconstruction. The horizontal lines contain a projection set of the emission data from one single view. With this arrangement of data, a point source is represented as a sinusoidal curve, as can be seen in the measured sinogram in Figure 2.11.

Listmode File Standard data acquisition with the BrainPET is performed in listmode. A listmode file contains all information on prompt and random coincidences, together with block single counters, such as CFD, XYE and qualified single counters. Time marks with a high temporal resolution are inserted (every 200 μs for the BrainPET) for the offline framing of the listmode data. With dedicated I/O interfaces on the hardware it is possible to insert further trigger data, e.g. for tagging the start of MRI sequences with the same temporal accuracy as the event decoding.

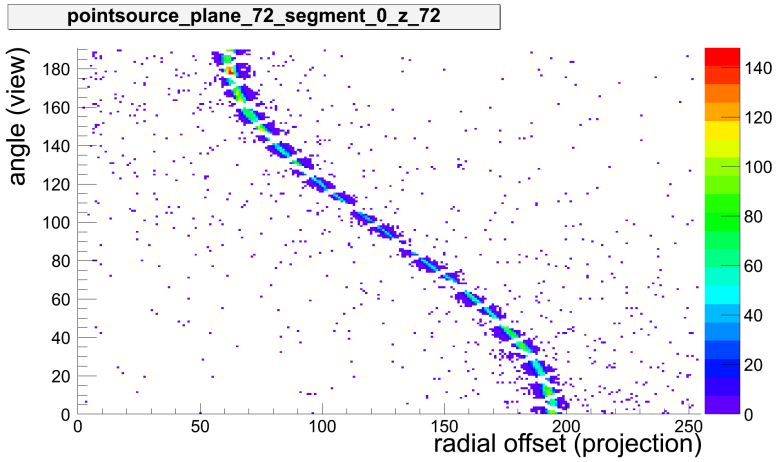

Figure 2.11.: Sinogram of a measured point source. The gap structure of the BrainPET's geometry is clearly visible.

Image An image in nuclear medicine is a matrix of discrete values, representing the estimate of the tracer distribution within the FOV. The standard reconstructed image for the BrainPET stores the intensity values in a matrix with 256×256 pixel transaxially and 153 image planes. The assigned voxel size is $1.25\,\mathrm{mm}^3$. This format is referred to as flat format and has no further header information. Therefore, the ECAT7 format is used, which can store information on the patient and study. Additionally, their format is capable of storing multiple frames, as required for dynamic studies. The DICOM format is a powerful format used in many image applications and a standard in MRI. For dynamic PET, however, the ECAT7 is currently the more conventient solution.

2.5.2. Image Reconstruction

Two basic approaches for PET image reconstruction exist to obtain images from the acquired projection data. The analytic reconstruction is computationally fast and straight-forward with well known properties. However, it has the drawback of poor noise properties, which is a major issue in clinical scans.
Iterative reconstruction is computationally demanding, but offers a more elaborated noise handling, due to a more accurate modelling of the imaging process and the entire system response. Image reconstruction is crucial also for quantification, since the correction factors have to be considered correctly according to the selected model.

Analytic Image Reconstruction

Analytic reconstruction algorithms assume the emission data to be ideal, which is an oversimplification of the underlying physics of the measurement process. Prior to the reconstruction, the acquired data need to be corrected for random coincidences, deadtime, scatter, attenuation and the varying crystal efficiencies. For a long period of time, filtered backprojection (FBP) has been the standard reconstruction algorithm applied in PET.
The information on the exact position of annihilation along the LORs is not available. Thus, a constant value along the LOR is assumed. An essential step in analytic reconstruction is the backprojection of the measured data from the projection space into image space. By superposition of the Fourier transforms of all backprojections the result equals the Fourier transform of the image, weighted or filtered with the inverse distance from the origin in Fourier space. In this way, the reconstructed image suffers from an oversampling of the centre of the Fourier transform, which amplifies low frequencies and attenuates high frequencies. The result is a blurred version of the measured distribution. In order to compute the tracer distribution from the projections, the filtered backprojection (FBP) is available. The projection data are filtered with a ramp filter before backprojection, which implies a pre-correction for the aforementioned central oversampling in frequency space. Originally, filtered backprojection was defined only in 2D, but has been extended to 3D space. The line integral along the activity distribution $f(x, y)$ under a certain angle ϕ and radial offset x_r is a projection p. Equation 2.10 is referred to as the Radon transform. Its inversion is subject to image reconstruction.

$$p(x_r, \phi) = \int_{-\infty}^{\infty} f(x, y) dy_r \tag{2.10}$$

Besides the lower computational burden, the high linearity of this reconstruction method is advantageous, not only for estimating performance parameters of the scanner (such as image resolution). However, the FBP is defined for complete projection data. For scanners exhibiting gaps in the detector geometry such as the Siemens HRRT or the BrainPET scanners, iterative methods are mandatory to handle the incomplete projection data [17].

Iterative Image Reconstruction

In PET the iterative reconstruction approach is superior to the analytical methods due to a more realistic modelling of the imaging system [93, 43]. A more general

formulation of the statistical measurement and reconstruction process may improve the accuracy of the image reconstruction. Models for iterative image reconstruction usually consist of five components:

- Model of the Image Space
- Model of the Measurement Process
- Model of the Projection Data
- Objective Function
- Optimization Strategy

Usually, approximations have to be made to keep the method practical with regard to computational effort. The image space is subdivided into a grid of I discrete voxels, where the estimated image intensity values x_i with i=1...I, represent the assumed distribution of the actual tracer concentration $\lambda(r)$. Most algorithms apply pixel basis functions $b(r)$ that are constant within small, non-overlapping rectangular regions arranged in a Cartesian grid according to

$$\lambda(r) = \sum_{j=1}^{J} \lambda_i b_j(r). \tag{2.11}$$

Since x_i is the realisation of a Poisson random process, the likelihood P for the number of actually emitted events k, when λ events were expected, is

$$P(x_i = k) = e^{-\lambda} \cdot \frac{\lambda^k}{k!} \text{ with } k \in \mathbb{N}. \tag{2.12}$$

The number of predicted events y_j contained in one of the J LORs j is described by

$$\hat{y_j} = \sum_{i=1}^{I} a_{i,j} x_j, \tag{2.13}$$

for a discretised activity distribution in the image space. The coefficients a_{ij} contain the probabilities that an annihilation in image element i is seen by the LOR j. Equation 2.13 describes the forward projection of the data. However, the detected number of events $\hat{y_i}$ may differ from the expected ones $E[y_i]$, especially during short acquisition times, which results in additional noise (Equation 2.12). Since x_i

represents the realisation of independent statistical Poissonian random processes, their linear combination is also Poissonian

$$E[y_j] \stackrel{!}{=} \hat{y_j} = \sum_{i=1}^{I} a_{i,j}\lambda_j. \tag{2.14}$$

However, the assumption that the detection of coincidences is independent of other detections is only valid for negligible deadtime and pile-up at lower countrates [111]. With this assumption, the likelihood P is modelled by a Poisson random variable

$$p(y|\lambda) = \prod_{i=1}^{J} e^{-\hat{y_i}} \frac{\hat{y_i}^{y_i}}{y_i!}. \tag{2.15}$$

This relation can be transferred to the likelihood function $L(x)$ or respectively to the log-likelihood function $l(x)$, which is easier to handle. Combining the data model with the image model, the reconstruction problem can be described by a set of linear equations with the elements of the system matrix $\mathbf{A}$ with its elements a_{ij}. The system matrix $\mathbf{A}$ is a main component of the model of the measurement process. This matrix connects the unknown activity distribution λ within the FOV with the expected number of events detected within each LOR $E[\mathbf{y}]$

$$E[\mathbf{y}] = \mathbf{A}\lambda. \tag{2.16}$$

Besides the geometric detection probabilities, a_{ij} can contain also multiplicative effects of probabilities for attenuation, normalisation and deadtime. For an accurate modelling of additive noise such as random coincidences $\mathbf{R}$ and scattered coincidences $\mathbf{S}$, the expectation may be formulated as

$$E[\mathbf{y}] = \mathbf{A}\lambda + \mathbf{R} + \mathbf{S}, \tag{2.17}$$

denominated as the ordinary Poisson (OP) model. Thereby, preservation of the Poisson nature of the emission data during data correction and image reconstruction is of vital importance. Reconstructing precorrected data, the true coincidences are corrected for random coincidences, Compton scatter, crystal efficiency variations, detector deadtime, and photon attenuation before image reconstruction. This, however, disturbs the Poission characteristics of the emission data [63] and compromises image quality and noise control.
The solution of this equation is sensitive to noise within the measurement vector $\mathbf{y}$ and thus is performed with iterative methods. Furthermore, a direct inversion

of this linear matrix equation is computationally demanding or even not existing. The inversion is solved iteratively, calculating successive approximations of the tracer distribution, estimating a solution that fits with the acquired data.
A further important component of the iterative approach is the cost function or objective function. This statistical function defines the criterion to determine which estimation of the tracer distribution is considered as the best one. The objective is to maximise the consistency between the observed emission data and the reconstructed image. Today, the most commonly used function is the Maximum-Likelihood (ML), beside Least-Squares (LS) or maximum a posteriori (MAP) methods. The ML estimation assumes that the observed data are acquired according to the underlying Poisson distribution. The image that maximises the likelihood $l(y|\lambda)$ is assumed to be the best estimate to the measured data. The maximum-likelihood expectation-maximisation (ML-EM) algorithm and its variants are the most commonly used iterative reconstruction algorithms in emission tomography.
The cost function in this algorithm is the Poisson likelihood and the equation for updating the image estimate is given by

$$x_i^{k+1} = \frac{x_i^k}{\sum_{j=1}^{J} a_{i,j}} \cdot \frac{\sum_{j=1}^{J} a_{i,j} y_j}{\sum_{i=1}^{I} a_{i,j} x_i}. \tag{2.18}$$

The first estimate of the image (k=0) for all voxels x_i is usually assumed to be a uniform, non-negative distribution. The ML-EM algorithm is consistent and predictable in its convergence behaviour even with noisy emission data. One drawback of ML-EM is the relatively slow convergence. Furthermore, it depends on the additive components, namely the scatter and random contribution. In datasets with higher background activity, the convergence is achieved at later iterations steps. Consequently, the optimal number of ML-EM iterations is data dependent. The calculation of a converged solution requires computational effort as orders of magnitude higher compared to FBP. Furthermore, the algorithm yields images that increase in noise with the number of iterations, mainly due to statistical errors and remaining inconsistencies in the system model. From Equation 2.13 it follows that the number of counts in the image represents the number of detected events, which is a pre-requisite for quantification. Furthermore, the introduction of the stochastic model of the projection measurement combined with OP-OSEM accounts for the Poisson nature of the counting experiment and provides a better noise treatment compared to pre-corrected ML-EM or even the FBP approach. A model proposed in [46] includes the additive noise, such as randoms r and scatter s,

as modeled in Equation 2.17

$$x_i^{k+1} = \frac{x_i^k}{\sum_{j=1}^{J} a_{i,j}} \cdot \frac{\sum_{j=1}^{J} a_{i,j} y_j}{\sum_{i=1}^{I} a_{i,j} x_i + r_i + s_i}. \tag{2.19}$$

The block iterative reconstruction procedure applying the ordered – subset expectation – maximisation algorithm (OSEM) is derived from the ML-EM. It has been developed for SPECT and later translated to PET [53]. The data is subdivided into ordered disjoint subsets and a ML-EM iteration is applied on the data from only one subset at a time. The subsets are defined to have a maximum angular separation. At each update a different subset of projection data is used and the subsets are usually processed in a periodic pattern. The OSEM algorithm accelerates convergence by a factor roughly equal to the number of subsets. However, the organisation into subsets has to be chosen carefully because it is crucial to the convergence of the algorithm and may also be critical in regards of image artefacts [71]. The convergence in presence of noise is not guaranteed. However, high acceleration and clinically useful image quality have made OP-OSEM to be the clinical standard today. Very accurate modelling of the imaging process can lead to a significant improvement of image quality, as shown by the development of the reconstruction platform PRESTO [86] at the Forschungszentrum Jülich. The reduction of the long reconstruction times using highly parallel computer architectures is currently an issue of optimisation.

2.5.3. Image Calibration

Once the image is reconstructed with all corrections taken into account, the image intensity values are proportional to the actual concentration of radioactivity. However, in order to convert the intensity (in pseudo counts/s/ml) into the quantitative activity concentration (in Bq/ml), a calibration has to be performed. This is usually done by the measurement of an object with known activity concentration and computing the valid calibration factor. The validity of this factor, especially over time, is an issue of the long term stability and working daily quality control (dailyQC) of the scanners.

3. Basics of Magnetic Resonance Imaging

The discovery of nuclear magnetic resonance (NMR) by Felix Bloch and Edward Purcell in 1946 [14, 78] was the basis for nuclear magnetic spectroscopy (NMS), a method to analyse molecular structure and diffusion in physics and chemistry. The application of MR imaging (MRI) was first reported by Peter Lauterbur in 1973 [55]. This initial proof of concept has driven the development of MRI devices that are capable of imaging the human body, up to the point where MRI has become one of the most important imaging modalities in medicine. From the beginning image quality has improved tremendously due to a steady and ongoing development of MR systems and methods which lasts until today. Modern MRI systems are capable to deliver images with various contrasts of subjects *in vivo*. Imaging of anatomical structures with high spatial resolution and superior soft tissue contrast together with the delivery of information on perfusion, diffusion and local chemical composition of tissue and metabolites are clinically established. The discovery of the change of magnetic properties in oxygenated blood, known as the BOLD effect, is the fundamental basis of functional MRI (fMRI) applied in neuroscience, which allows to visualise neuronal activation of the brain. Furthermore, MRI is not only capable of providing imaging of protons (^{1}H), but also other nuclei less abundant in living tissue such as sodium (^{23}Na), phosphorous (^{32}P), and oxygen (^{17}O), denominated as x-nuclei. Compared to CT imaging, MRI provides superior soft tissue contrast and at the same time avoids potentially harmful radiation doses.

3.1. Physics of MRI

3.1.1. Nuclear Spins and Magnetic Resonance

An odd number of protons and/or neutrons in the atom's nucleus gives rise to the quantum mechanical property of nuclear magnetic resonance. The so called

spin angular momentum $\mathbf{S}$ is related to the magnetic dipole moment $\boldsymbol{\mu}$ via the gyromagnetic ratio γ

$$\boldsymbol{\mu} = \gamma \mathbf{S}, \tag{3.1}$$

where γ depends on the type of nucleus. Then quantum mechanics allows only two energy states for protons, parallel and anti-parallel to the field

$$E_{up} = \frac{1}{2}\gamma\hbar B_0 \tag{3.2}$$

and

$$E_{down} = -\frac{1}{2}\gamma\hbar B_0, \tag{3.3}$$

known as the Zeeman effect. A transition from one state to the other can only be achieved by absorption or release of a photon with the energy difference of $\gamma\hbar B_0 = \hbar\omega_{RF}$, with a frequency corresponding to the Larmor frequency.
When considering larger samples, the net magnetisation vector, as a superposition of the single spins, has no longer to be described by quantum mechanics, but it is sufficient to be treated as a classical magnetic moment. By application of external magnetic fields, the macroscopic vector $\mathbf{M}$ tends to align along that external field. Powerful magnets generate homogeneous fields up to field strengths larger than 14 Tesla. Whole-body human imaging systems use magnetic fields of up to 9.4 T with 1.5 T and 3 T being the clinical standard. The static field is denominated B_0 and is aligned along the patient axis (z-axis). The spin-system reaches an equilibrium where a net magnetisation M_0 exists along the direction of B_0. The phenomenological Bloch equation describes the dynamics of the magnetic momentum $\mathbf{M}$, subject to a time varying magnetic field $\mathbf{B}$, as given by

$$\frac{d\mathbf{M}(t)}{dt} = \gamma \mathbf{M}(t) \times \mathbf{B}(t) \tag{3.4}$$

resulting in a Larmor precession $\boldsymbol{\mu} \times \mathbf{B}$ of the atomic nucleus with an angular frequency of $\omega = \gamma B$. Manipulation of the magnetisation by a radio frequency field B_1 (magnitude of usually several μT) oriented perpendicular to B_0 and tuned to the Larmor frequency is usually termed as excitation. The induced torque on the total magnetization vector $\mathbf{M}$ tips the vector away from its initial state. The flip angle α, by which the net magnetisation vector is rotated away from the z-axis (assuming perfect on-resonant excitation) is given by

$$\alpha = \int_0^t \gamma B_1(\tau) d\tau. \tag{3.5}$$

For example, the time integral of the RF pulse determines the flip angle. Maximum (pure) transverse magnetisation is consequently achieved by a 90° pulse while 180° pulses that invert magnetisation from $+M_0$ to $-M_0$ are usually referred to as inversion pulses [31, 68].

3.1.2. Relaxation

The term relaxation describes the behaviour of $\mathbf{M}$ returning to the thermodynamic equilibrium. The T_1 relaxation refers to the spin-lattice or longitudinal relaxation and denominates the average time constant for the longitudinal magnetisation to return to its thermal equilibrium state along the main magnetic field. The modified Bloch-equation for M_z reads

$$\frac{dM_z(t)}{dt} = \gamma(\mathbf{M}(t) \times \mathbf{B}(t))_z - \frac{M_z(t) - M_0}{T_1}. \tag{3.6}$$

Neighbouring precessing nuclei can fall out of phase coherence. This results in a reduction of the macroscopic transversal component M_{xy} and thus in signal loss. The constant for this spin-spin relaxation is referred to as T_2 or transverse relaxation, giving rise to the modified Bloch equations for the transverse magnetisation

$$\frac{dM_x(t)}{dt} = \gamma(\mathbf{M}(t) \times \mathbf{B}(t))_x - \frac{M_x(t)}{T_2}, \tag{3.7}$$

$$\frac{dM_y(t)}{dt} = \gamma(\mathbf{M}(t) \times \mathbf{B}(t))_y - \frac{M_y(t)}{T_2}. \tag{3.8}$$

Thereby, the time constant for T_1 is usually larger than T_2. Both T_1 and T_2 depend on the rate of molecular motions as well as on the molecular structure. Thus, T_1 and T_2 depend on the tissue under investigation. In practice, one observes a further reduced relaxation time constant T_2^* which is caused by pure T_2 decay and static field inhomogeneities. This is the actually observed decay time of the observed free induction decay (FID) and may differ significantly from T_2 in larger samples or living subjects (see Figure 3.1).

3.1.3. Linear Gradient Fields and Selective Excitation

Spins of a sample located in the B_0 field precess at nearly the same Larmor frequency. The FID signal induced in the RF receiver coil does not contain information about the position of individual spins, which, however, is the prerequisite

for imaging. Therefore, a gradient field $\mathbf{G}$ is superimposed on the B_0 field. The gradient field can be switched independently in the physical x-, y- and z-direction and is consequently denominated as G_x, G_y and G_z. Gradient fields are approximately two to three orders of magnitude lower than the B_0 field, but have high demands on temporal accuracy and geometric linearity within the FOV. The superposition of gradient fields force the spins at different locations to precess at different frequencies according to

$$\omega(\mathbf{x}, t) = \gamma(B_0 + G(\mathbf{x}, t)) \tag{3.9}$$

allowing for a frequency based position encoding of spins. The short term execution of a gradient field forces the spins to accumulate a position dependent phase. With phase and frequency encoding, usually performed in perpendicular directions within one slice 2D imaging sequences can be developed. Not only the reception of signals can be influenced, but also the excitation. By execution of a gradient during irradiation of a RF pulse with well defined bandwidth, only those spins which precess within the irradiated frequency bandwidth are excited. This principle is applied in order to excite one single slice of desired thickness (often perpendicular to the patient's z-axis).

Signal Detection

According to Faraday's law, the precessing magnetisation induces an electromagnetic force in the receiver coil located nearby the sample. The basic signal equation relates the magnetisation $\mathbf{M}$ with the expected signal s according to

$$s_r(t) \sim \int_{\text{vol}} M(r, t) d\mathbf{r} \tag{3.10}$$

$$s(t) = \int_{\mathbf{r}} \mathbf{M} e^{-ik(t)\mathbf{r}} d\mathbf{r} \tag{3.11}$$

with $k(t) = \frac{\gamma}{2\pi} \int_0^t \mathbf{G}(\tau) d\tau$, which allows for the description of almost every imaging method [68], neglecting the intermediate step of induction and signal demodulation.

Image Reconstruction

The MR signal is stored in a Fourier plane called k space. Since the spin resonance data is frequency- and phase-encoded according to the spatial location, it can be

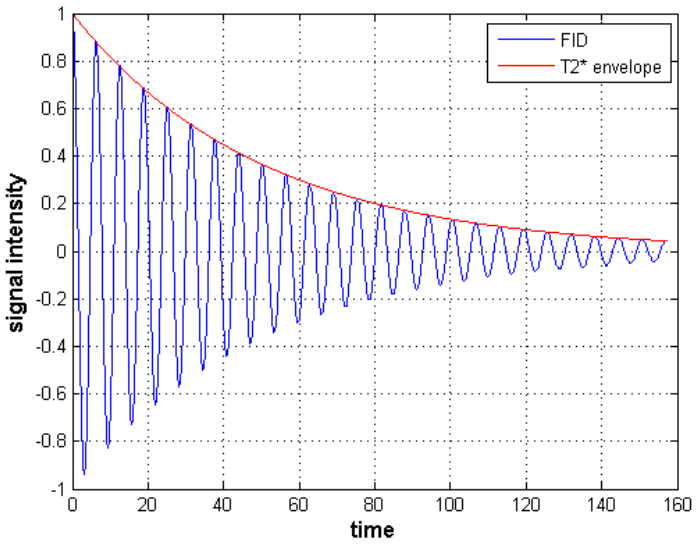

Figure 3.1.: Free Induction Decay (FID). The measurable signal induced in the RF coil show an oszillating, exponentially decaying function (blue curve). The red curves shows the T_2^*-envelope.

analysed by the Fourier transform. In k-space, f_x-coordinates (horizontal spatial frequencies) and f_y-coordinates (vertical spatial frequencies) of the Fourier plane are replaced by k_x and k_y-coordinates. A classic spin echo sequence fills the k-space line by line. For this purpose a single slice is excited which is in the following readout by several phase-encoding steps followed by a readout gradient. The k-space location (k_x and k_y coordinates) of data is governed by the time integral of the gradient after excitation. Different encoding steps allow for moving along the k-space in order to acquire the complete data. Image reconstruction in MRI can be performed by application of an inverse Fourier transform of the k-space data (see Figure 3.2). Due to the k-theorem, the time signal $s(t)$ can be interpreted as equivalent to the Fourier Transform F of the weighted proton density $f(x, y, z)$ as

$$s(t) = F\{f(x,y,z)\}(k_x,k_y,k_z) = \iiint_{-\infty}^{\infty} f(x,y,z)e^{-i2\pi(k_x x+k_y y+k_z y)}\mathrm{d}x\mathrm{d}y\mathrm{d}z. \quad (3.12)$$

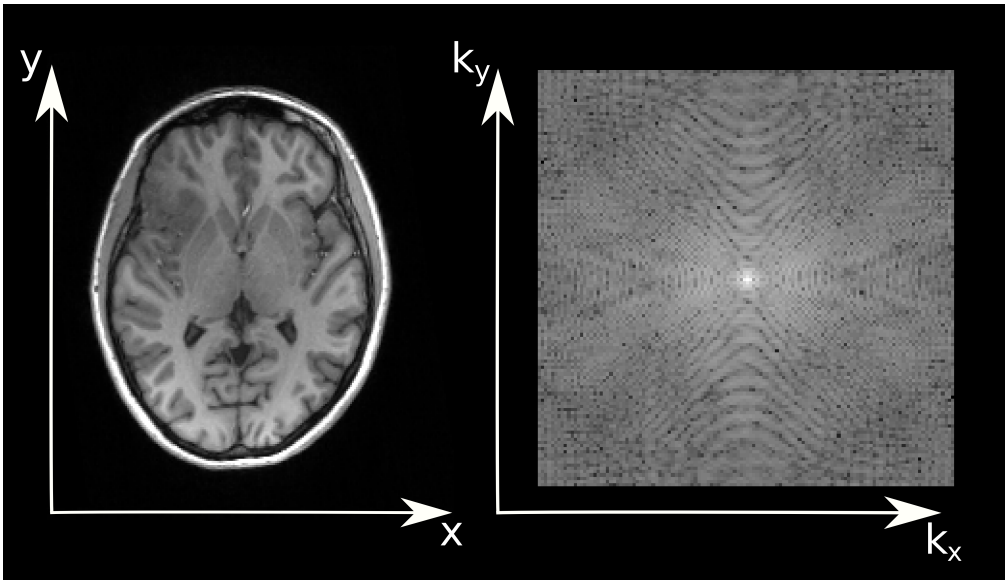

Figure 3.2.: The reconstructed MR image (left) as the inverse Fourier transform of the acquired k-space data (right).

3.2. Methods and Contrasts in MRI

3.2.1. Spin Echo

The concept of echoes in MR was first applied in NMR and fully explained by Erwin Hahn in 1950 [12]. It was further developed by Carr, pointing out more aspects of a train of 180° refocusing pulses. After spin excitation, the spins precess at slightly different frequencies, followed by defocusing after a short time. In nuclear magnetic resonance, spin echo refers to the refocusing of precessing spin magnetisation by a 180° pulse at Larmor frequency. The MR signal observed after the initial excitation pulse decays with time due to spin-spin relaxation and magnetic field inhomogenietis (T_2^*). This loss of transverse magnetisation is partly reversible and can be recovered by a 180° refocussing pulse. A refocussing pulse is applied after the time period T of dephasing and the inhomogeneous evolution will rephase to form a so called spin echo at time $2T$. The intensity of the echo relative to the initial signal is given by e^{-2T/T_2}.

3.2.2. Gradient Echo

The major difference between gradient and spin echo sequences is the application of flip angles that are usually smaller than 90° and the absence of the 180° rephasing pulse. The reduced flip angle leads to a smaller amount of magnetization that is tipped into the transverse plane. Consequently, recovery of longitudinal magnetization is faster. This allows a shorter repetition time (T_R) and echo time (T_E) and hence potentially reduces the measurement time. The decay of the transverse magnetization is due to T_2^* relaxation and to B_0 field inhomogeneity and to static magnetic susceptibility effects. The relaxation is not reversed and the loss of signal results from T_2^* effects. The signal obtained is thus T_2^*-weighted rather than T_2-weighted. These sequences are more sensitive to magnetic susceptibility artefacts than spin echo sequences.

3.2.3. Applications

A major perturbation of the resonance frequency of atomic nuclei is due to the shielding effect of surrounding electrons. This electronic shielding reduces the effective magnetic field at the atomic nucleus. Consequently, the Larmor frequency is reduced. This shift in the resonance frequency due to the electrons' molecular orbital coupling to the external magnetic field is referred to as chemical shift. This effect allows to probe the chemical structure of tissue which depends on the electron density distribution in the corresponding molecular orbitals. This is a source for image deformation, but also the basis of a powerful tool referred to as NMR spectroscopy. Beside the T_1, T_2 and T_2^* weighted images, the fMRI methods have been established in MRI. With fMRI it is possible to detect changes in the cerebral blood flow, mainly by the blood-oxygen-level-dependend contrast (BOLD) [70]. With this technique, the neural activity in the brain which is related to the energy consumption, can be imaged. Since the data suffer from noise, a preprocessing together with statistical analysis is crucial to obtain reliable results. With a temporal resolution of 4 s down to 1 s, and a spatial resolution down to 1 – 2 mm, fMRI is a powerful modality in neuroscience and provides valuable information in hybrid MR-PET studies. Further contrasts, such as the MR based angiography (MRA) and ultra short echo time (UTE) sequences for bone detection can provide hybrid MR-PET imaging with additional information (see Figure 3.3). As described in Section 5.2 the segmentation of bone, tissue and air from MR images is a major concern for attenuation and scatter correction for PET in hybrid MR-PET and thus for the quantification of PET images [12].

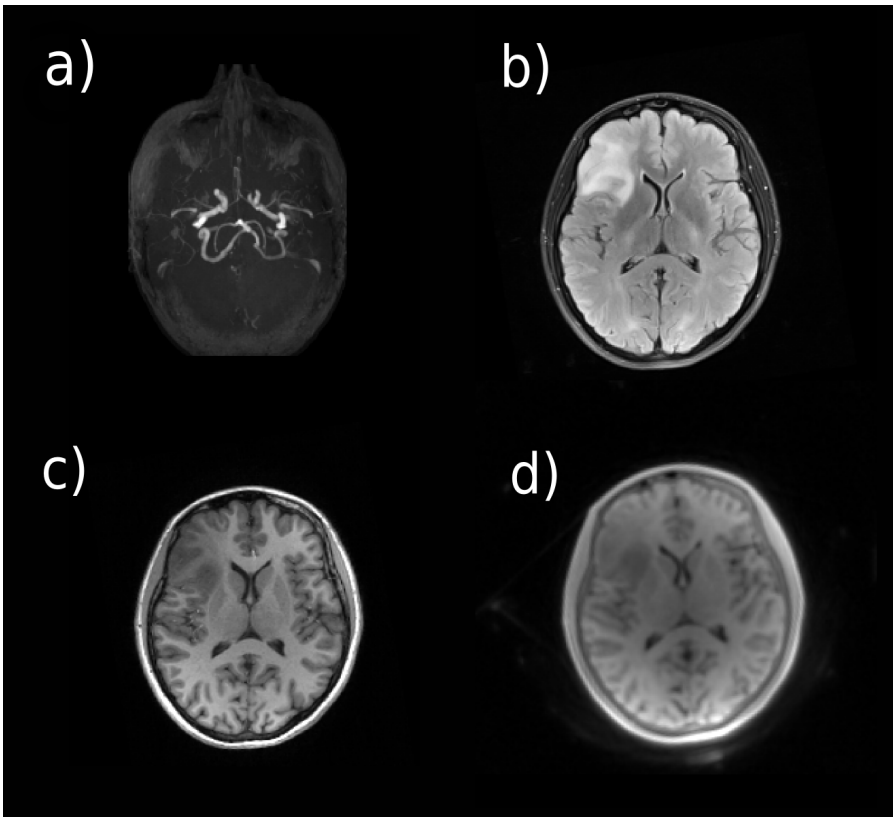

Figure 3.3.: Versatile MR contrasts acquired with the 3T MR-BrainPET. Figure (a) shows an MR Angiography acquired with a time-of-flight (TOF) sequence. Figure (b) shows a T_2-weighted image, (c) an anatomical T_1-weighted image (MP-RAGE) and Figure (d) the first echo of the UTE sequence used for PET attenuation correction with bone detection. In the UTE sequence, even structures of the MR coil become visible.

3.2.4. MR Hardware Architecture

The previously described magnetic fields are generated by different electromagnetic coils. Since the field strength and temporal behaviour differ by several orders of magnitude, shape and material of these coils are also very different. The main magnetic B_0 field is constant over time and requested to be homogeneous over the entire FOV. Modern magnets apply helium cooled superconducting materials wired in a cylindrical shape in order to provide a clinically relevant magnetic field in the range of 1 to 11 Tesla. For lower field strengths, permanent or resistive magnets can be applied, but these are limited to specialised applications. For spatial encoding, gradient coils with a maximum field strength in the order of 80 mT/m are integrated in the MR bore. Different coils are applied for the different physical gradient directions G_x, G_y and G_z. These gradient fields are switched fast, with rise times up to 5 μs/mT/m, and also require a very linear field in order to minimise spatial distortions. The fast changing gradient fields may also induce eddy currents in conductive material within the MR scanner, reducing the effective gradient fields. The B_0 field is known to suffer from imperfections, especially susceptibility effects when positioning a subject in the field.
A shift in the overall field strength may be corrected by changing the RF frequency for transmit and receive, which corresponds to a constant field correction. Linear corrections are accounted for by an offset current to the gradient coils. Higher order corrections may be done applying metal shim plates to modify the existing magnetic field or electromagnetic shim coils to generate additional magnetic fields. These corrections are performed in the range of parts per million (ppm) of the B_0 field strength. RF coils with single channel or arrays with multiple channels are applied, transmitting and receiving RF fields in the range of the Larmor frequency of the nucleus. Since the received energy is orders of magnitude lower than the excitation energy, different channels for reception and transmission are applied. For acceleration of the imaging process, parallel reception hardware is available and applied together with the respective MR sequences and image reconstruction procedures. Shorter wavelengths, especially for proton imaging with ultra high field (UHF) MRI, make parallel excitation (pTX) concepts necessary, which may improve image homogeneity, but on the other hand are more demanding in regards of safety control of the SAR (specific absorption rate).

4. Simultaneous MR-PET Imaging

Parts of this chapter have been published in [104].

4.1. Challenges and Advantages

The novel hybrid imaging technology of MR-PET offers versatile advantages compared to other established technologies. A reduced radiation dose compared to PET/CT is not only important for pediatric applications, but also for therapy control with several subsequent scans. Besides, the measurement time can be reduced due to the simultaneous acquisition of both modalities, since often MRI scans are required additionally to PET/CT scans. This increases the patient convenience especially scanning infants and critically ill patients and holds the potential for a higher patient throughput, compared to sequential MR/PET. With the fast acquisition of MR images with EPI readout in the range of seconds, the motion information of the patient may be derived from the MR images. Thus, not only PET data but also MR data may be motion corrected without applying external motion tracking [87]. Alternatively, the information from MR navigator sequences can be used to correct MR and PET data for motion. A physical effect that may contribute to a better PET image resolution in the image planes perpendicular to the magnetic field is the effectively reduced positron range. At high magnetic fields, the image quality of positron emitters with a high positron energy, such as ^{68}Ga ($E_{\max} = 1.89\,\mathrm{MeV}$) or ^{15}O ($E_{\max} = 1.7\,\mathrm{MeV}$) can be improved [36]. With the truly hybrid technology, the spatial and temporal co-registration of the two modalities can be guaranteed which is important for example in neuroscience, combining neuroreceptor PET with fMRI. However, clinically relevant protocols have to be implemented and optimised to exploit the high potential of hybrid MR-PET imaging with the variety of anatomical contrasts and functional parameters [66].
To realise simultaneous PET and MRI the technological challenge of possible mutual interferences had to be overcome. The interference of the PET device with the strong static magnetic field B_0 and the fast switching gradient fields G as well

as the irradiated RF power had to be excluded. Therefore, the conventional PMTs are replaced by the non-magneto sensitive APDs [30] or SiPMs [85]. Furthermore, the PET electronics is shielded against the RF field B_1. In turn, the presence of the PET insert within the MR scanner may result in degradation of the MR image homogeneity and SNR. The homogeneity of B_0 may be compromised, which has to be compensated by appropriate passive and active shimming. Besides, the RF receiver coil is influenced and detuned by the RF shielding of the PET component and has to be adapted to the new settings. Additionally, noise pickup by the receiver coil from the PET electronics has to be excluded [112, 104].
An additional challenge and presently active field of research is the determination of accurate attenuation properties of the scanned subject. Since no device for the acquisition of transmission data is available within the MR bore, the attenuation data have to be derived from MR images [39]. Also the scatter simulation relies on an accurate estimation of scattering medium, defined by the attenuation map. So not only the quantitative tansmission properties, but also the exact alignment is of vital importance [15]. For the determination of the image derived input function (IDIF), high resolution of the PET image is a prerequisite in order to avoid uncertainties related to the partial volume effect [65]. The IDIF is often needed in tracer kinetic modelling [19]. Besides using the high resolution of the BrainPET, the IDIF can be further improved taking into account additional morphological information from MR angiography or other structural MR image contrasts [23].
Section 4.2 gives a description and characterisation of the utilised MR-PET hybrid scanners and Section 4.4 gives a detailed investigation of influences of MRI on PET measurements.

4.2. MR-BrainPET Scanners

The experimental results presented in this work are mainly acquired with the Siemens 3T and 9.4T MR-BrainPET scanners. These hybrid MR-PET scanners consist of a BrainPET insert and an MR scanner. The MR component of the 3T MR-BrainPET (see Figure 4.1(a)) is essentially the commercially available Siemens 3T TIM Trio with minor modifications, such as a vertically fixed patient bed and an adapted head coil with low attenuation for 511 keV photons. For the 9.4T MR-BrainPET (see Figure 4.1(b)) the MR scanner is developed by the Forschungszentrum Jülich in collaboration with Siemens Healthcare. It contains the same BrainPET scanner model but with longer cables for signal transmission.

(a) 3T MR-BrainPET.

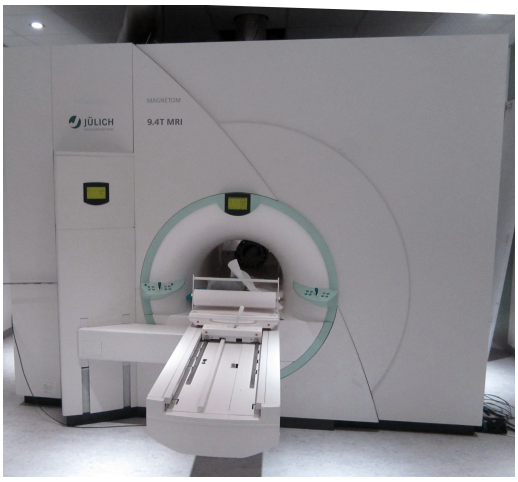

(b) 9.4T MR-BrainPET.

Figure 4.1.: 3T (a) and 9.4 T (b) hybrid MR-BrainPET scanners installed in Jülich.

4.2.1. MR Component

As described above, the characteristic instrumental features of the MR scanner are the static magnetic field (B_0), the temporal and spatially varying gradient fields in x- y- and z-directions, denoted by G_x, G_y and G_z, and the RF field, denoted by B_1. In both scanners, the B_0 field of 3T and 9.4T, respectively, is directed along the scanner's z-axis. The static field determines the necessary RF carrier frequency of approximately 126 MHz, which corresponds to the Larmor frequency of protons at 3T. The Larmor frequency for protons at 9.4 T corresponds to 400 MHz. This results in higher demands on RF technology and homogeneity of the applied magnetic fields and spin excitation. During execution of an MR sequence, RF pulses of typical durations ranging from less than 1 ms up to a few ms and a magnitude in the range of 10 to 20 μT are applied. The RF pulses may be modulated in amplitude and phase. The reference setting for both scanners is a transmitter voltage of 215 V for a rectangular pulse duration of 1 ms to generate a 180° flip angle *in vivo*. The total power deposited by the application of RF pulses is subject to hardware supervision, which ensures that the induced specific absorption rate (SAR) remains below the safety limit. This effectively regulates the amplitude, spacing and duration of the RF pulses. The gradient fields, i.e. additional spatially-varying magnetic fields, define the spatial encoding of MR imaging and are generated by gradient coils mounted within the MR scanner. The

gradient coils are identical for both scanners and applied in a pulsed manner with durations of a few milliseconds and amplitudes up to 40 mT/m in each physical direction. The time to reach a given amplitude is determined by the unit rise time which can be on the order of 10 μs/mT/m.
An MR sequence consists of well-defined gradient and RF pulses. These pulses usually constitute a common block, which is repeated with a predefined spacing (repetition time, T_R) as depicted in Figure 4.5.

4.2.2. BrainPET Component

The BrainPET component is designed as an insert to be placed in the bore of the MR scanner. It consists of 32 copper-shielded detector cassettes. Copper has good shielding properties regarding RF radiation of the applied wavelength. Each detector cassette contains 6 detector blocks each with a 12×12 LSO crystal matrix, consisting of crystals of $2.5 \times 2.5 \times 20$ mm^3 size. The crystal matrix is read out by a 3×3 array of magnetic field-insensitive APDs. The pre-amplified analogue signals of each detector cassette are transmitted via shielded cables of 10 m length at the 3T MR-BrainPET and 12 m length at the 9.4T MR-BrainPET scanner to the filter plate. The main PET electronics is decoupled from the MR cabin by the filter plate, the shielding of cables and the detector cassettes. Digitisation of the PET signals, energy and position determination of single events and coincidence search is performed on dedicated hardware mounted outside the MR cabin [67, 6]. A CFD single event is checked regarding its energy (here 420 keV to 580 keV) and its position (within a certain area of the detector block), resulting in an XYE[1]-qualified account for coincidence lookup.

4.2.3. PET Detector Setup

In order to bring the PET scanner in an optimal status in terms of homogeneity of detection efficienccy, the detector setup has to be adapted and verified. This involves

- Crystal Lookup Table (CLU),
- Energy Lookup Table (ELU) and

[1]XYE-single event: X denominates the x-position on block, Y the y-position on block and E the photon energy

- Timing Lookup Table (TLU).

The block-individual CLU denotes the assignment matrix of a nearly continous position among the detector (512×512) to discrete crystal number (12×12) (see Section 2.4.4). Misalignments influence the positioning of events and lead to inhomogeneities in the crystal sensitivity. Due to shifts in the APD gains, a regular check of the validity of the CLUs have to be performed, in order to have the system in a propper status. The correct values in the ELU assure that the energies of accepted events are in the desired range and only measured energies within the thresholds defined by LLD and ULD are accepted. The TLU corrects for timing differences between the blocks in order to find coincidences within the definded coincidence timing window. All these setup parameters have to be checked and updated in order to allow for optimal PET data acquisition.

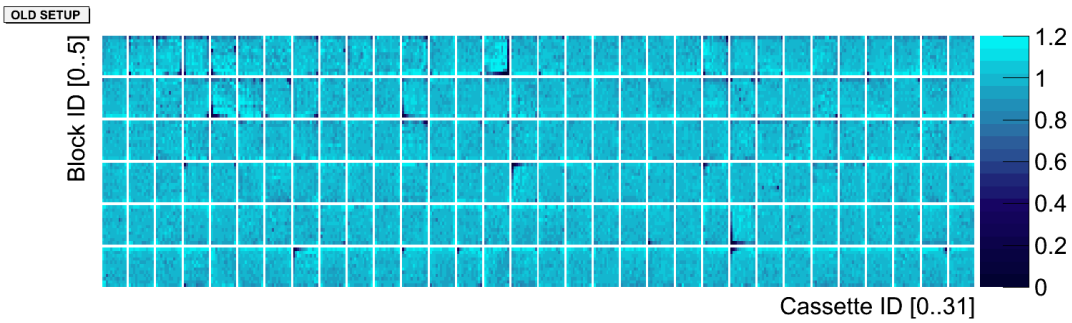

(a) Detector Setup before tuning.

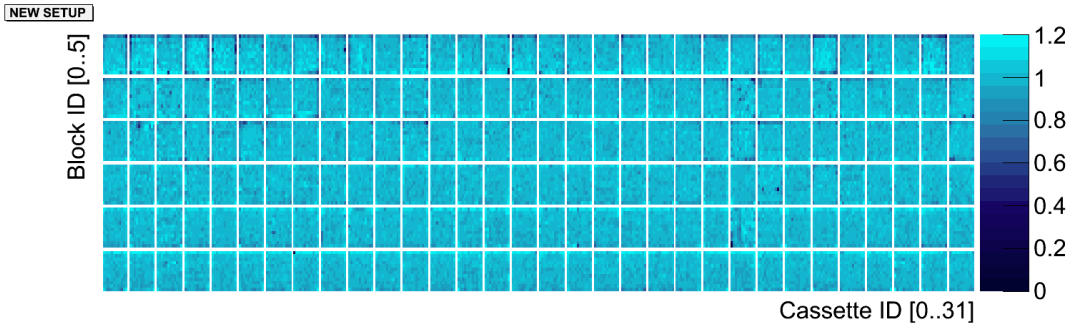

(b) Detector Setup after tuning.

Figure 4.2.: Cystal efficiencies ε (without geometric component g) before (a) and after (b) tuning of the setup. The improvement of homogeneity, especially for corner and edge crystals, is clearly visible.

The result of setup optimisation should be a more homogeneous crystal efficiency distribution among the detector (see Figure 4.2.3). The verification of the setup is an issue of long term stability which is assessed by the DailyQC measurements (see Section 5.9).

4.3. Characterisation

The characterisation of PET scanners is proposed by the NEMA standards [1, 2, 4] in order to assure comparability of the characterised scanners. Two standards exist, one for whole body scanners with an inner diameter of 70 – 80 cm and one for small animal scanners with an inner diameter of 10 – 20 cm. The BrainPET scanner with its inner diameter of 36 cm is a special case regarding the size of the FOV. Thus, some of the standards had to be adapted to make this study feasible.

4.3.1. Countrate Performance

The LSO crystals contain the radioactive isotope ^{176}Lu with an activity of about 100 Bq/cm^3 emitting photons with energies above 350 keV [60]. This background activity becomes dominant at very low activity concentrations within the FOV and leads to a more significant amount of random coincidences. Besides, the photo peak detection of the detector shifts from the 511 keV peak and responds to the 350 keV peak of ^{176}Lu, assuming the dominant peak always at 511 keV. This affects the energy determination and finally results in a rejection of 511 keV photons.
Measurements were performed to find the limit of countrate above where this problem is not observed. A lowest countrate of approximately 11 true kcps has been defined (as depicted in Figure 4.3). When activity is brought into the scanner, the system needs some time to detect the 511 keV peak and to detect true coincidences which related to the automatic peakfinding. This becomes important, when patients are injected within the scanner and data are acquired starting from the time of injection.
To assess the noise equivalent countrate (NEC), a cylinder phantom of 20 cm length and 14 cm diameter was filled with ^{11}C and placed transaxially and axially centered into the PET scanner. The decay process was measured until the remanent activity fell below a measurable threshold.
The maximum NEC countrate of 164 kcps was found for an activity concentration of 26 kBq/ml, using the cylinder phantom with 14 cm diameter (see Figure 4.4) which is in good agreement with [57] and [51].

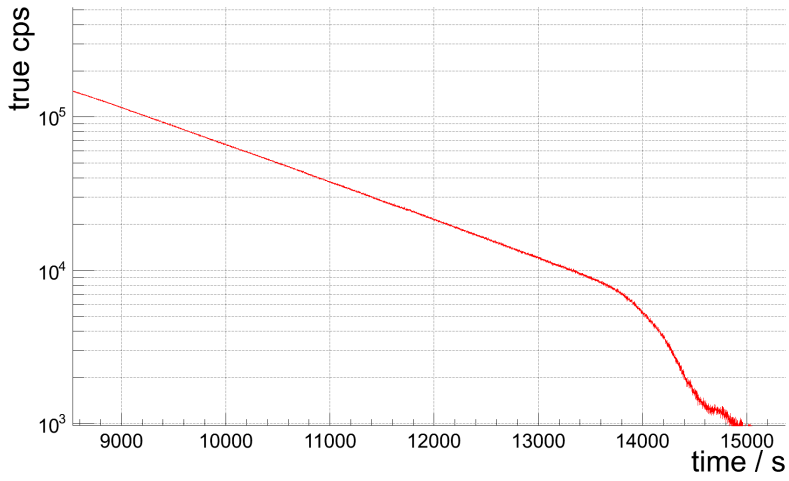

Figure 4.3.: Plot of the headcurve illustrates the problem of finding the photopeak at true countrates lower than 11 kcps due to the ^{176}Lu photon background.

4.3.2. Sensitivity

The sensitivity of the BrainPET was measured according to the NEMA standard with a point source and with a line source. For the line source positioned along the axial direction and transaxially centered, the sensitivity was found to be 0.6 % and for a transaxial offset of 10 mm the sensitivity was 0.9 % [57, 51]. For point sources, the peak sensitivity is detected at the centre of the FOV with 6.7 % (5.3 % at 10 cm radial offset).

4.3.3. Spatial Resolution

The spatial resolution of the scanner is limited by physical effects and the instrumentation. Physical effects are mainly the positron range, the acollinearity of the two annihilation photons and the penetration depth of the annihilation photons in the scintillation crystals, referred to as depth of interaction (DOI). According to the NEMA standard, the point sources were reconstructed with a FBP algorithm [1]. The measured image resolution in radial direction was found to be 2.8 mm (2.7 mm tangential, 3.4 mm axial) at the centre of the FOV and 3.3 mm (3.0 mm tangential, 4.1 mm axial) at 50 mm radial offset [57]. The approximation of image resolution r in the centre of the FOV for the BrainPET applying the empirical

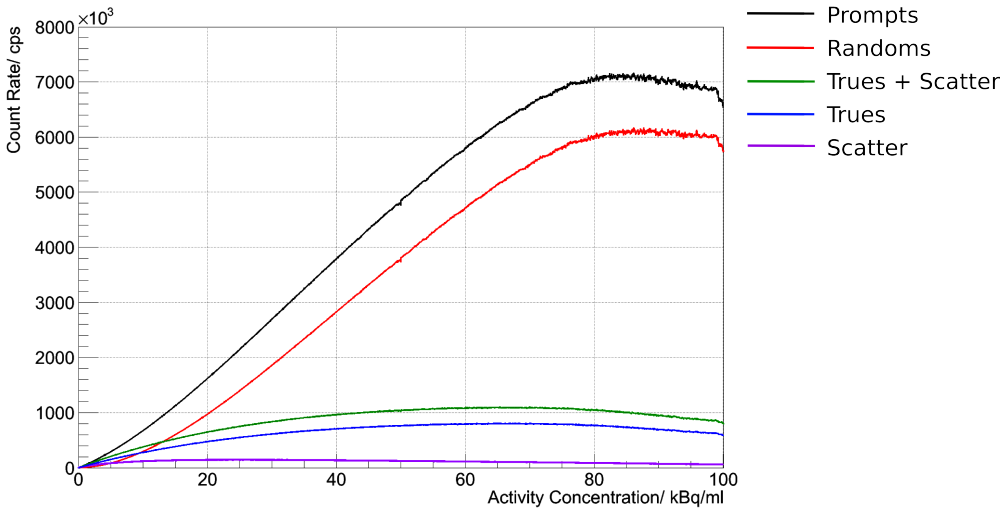

(a) Coincidence countrates of prompts and randoms for a high range of countrates.

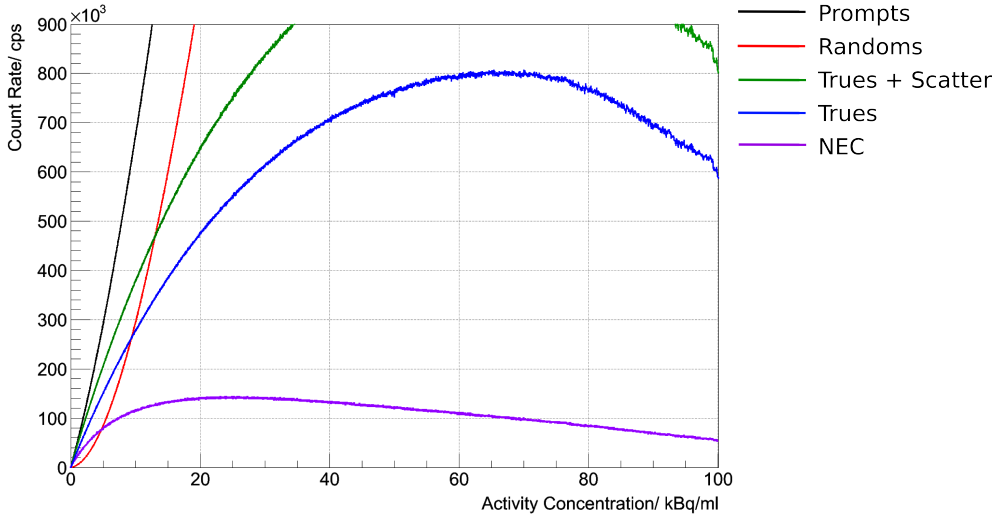

(b) NEC peak countrate and Trues+Scatter peak countrate.

Figure 4.4.: Noise equivalent countrate (NEC) showing the full dynamic range of the decay experiment in (a) and the relevant range for human studies in (b).

equation publised by Moses et al. [64]

$$r = 1.25\sqrt{\frac{d^2}{4} + (0.0022\ D)^2 + R^2 + b^2} \tag{4.1}$$

with detector size of $d = 2.5\,\text{mm}$, the system diameter of $D = 360\,\text{mm}$, the positron range of $R = 0.46$ mm for ^{18}F and the coefficient for the block design $b = 2$ results in a resolution of 3.1 mm. This estimation is in good agreement with the resolution measurements.
The scatter fraction measured according to the NEMA standard was determined to be 38 % - 42 % [51].

4.4. Influences of MRI on PET

During simultaneous MR-PET studies, a minor but reproducible and MR sequence-dependent countrate reduction has been observed. A more detailed analysis of this effect is presented in the following. A correction procedure is derived and evaluated in Chapter 5.6. As the combination of gradient and RF modulation in an MR sequence may be almost arbitrarily complex, a systematic investigation of the influence of each component is necessary and was performed in the present study. Nonetheless, the examined gradient and RF waveforms were similar to those applied in clinical MR sequences [104].

4.4.1. Influence of MR-Gradients

In order to test the influences of the gradient field a ^{68}Ge-cylinder phantom was positioned inside the BrainPET. In this test the RF head coil was removed to avoid any further interference. The gradient system offers different parameters: the amplitude (G_{max}), the repetition time (T_R), and the rise time (t_{rise}). The MR gradients G_{x}, G_{y} and G_{z} were switched separately with different parameters (see Figure 4.5). RF transmission was disabled during this test.

Influence of Gradient Amplitude First, the gradient amplitude was varied. The pulse duration was 1 ms, T_R was fixed to 2.5 ms and the rise time was 6.5 μs/mT/m. The amplitude was subsequently set from 5, 10, 15 to 20 mT/m. The duration of each sequence was 52 s with a pause of 60 s. The decrease in the prompt coincidence countrate was found to increase nearly linearly with the amplitude of the gradient pulses (Figure 4.6 and Table 4.1). The number of CFD singles, which denominate

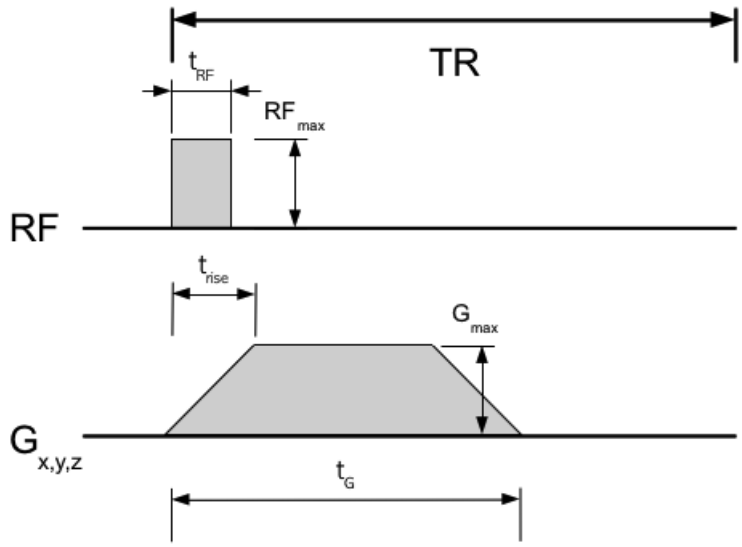

Figure 4.5.: Relevant MR sequence parameters, as separated and applied in dedicated test sequences.

the first qualification level for single events was not affected (Figure 4.6, red curve). As shown in Figure 4.6 (blue curve), the energy and position determination was, however, disturbed so that the XYE qualified singles were found to be reduced up to 0.47 %. This results in the observed instantaneous countrate drops of the prompt coincidences as well as delayed coincidences which are not shown here.

Gradient	$G_x(\%)$	$G_y(\%)$	$G_z(\%)$
5 mT/m	-0.12 ± 0.009	-0.11 ± 0.002	-0.55 ± 0.02
10 mT/m	-0.23 ± 0.013	-0.22 ± 0.0018	-0.76 ± 0.16
15 mT/m	-0.36 ± 0.014	-0.29 ± 0.015	-1.0 ± 0.063
20 mT/m	-0.47 ± 0.028	-0.41 ± 0.012	-1.1 ± 0.11

Table 4.1.: Influences of MR gradient amplitude. Measured prompt coincidence countrate change in percent (mean ± standard deviation (SD), n=3). The repetition time was 2.5 ms and the gradient duration was 1 ms.

Influence of Gradient Repetition Time The TR, i.e. the number of gradient switching operations within a fixed time period, was studied by shortening it from 20 to 10, 5, 2.5 and finally to 1.2 ms. The pulse duration was 1 ms, the amplitude

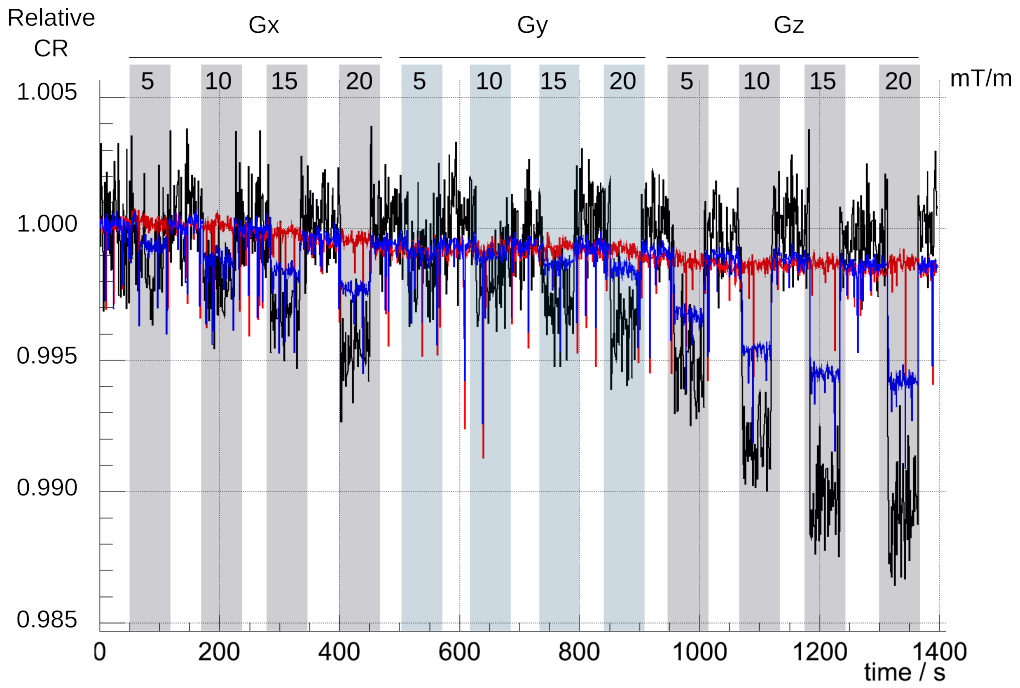

Figure 4.6.: Countrate of over time showing influences of MR gradient amplitude. Rates of CFD single events (red curve), XYE single events (blue curve), prompt coincidences (black curve) are depicted. The parameters were applied according to Table 4.1.

was 20 mT/m and the rise time was 6.5 μs/mT/m. The duration of each MR sequence was 52 s with a pause of 60 s. When varying the gradient repetition time, again a nearly linear influence on the prompt coincidence countrate was observed (Table 4.2 and Figure 4.7). The prompt coincidence rate was reduced with decreasing repetition time and depended additionally on the gradient direction. The most severe drop of 2.15 % was found for the shortest repetition time of 1.2 ms with the gradient in z-direction.

Gradient	$G_x(\%)$	$G_y(\%)$	$G_z(\%)$
20 ms	-0.10 ± 0.0061	-0.09 ± 0.0016	-0.17 ± 0.018
10 ms	-0.16 ± 0.0021	-0.09 ± 0.009	-0.31 ± 0.007
5 ms	-0.19 ± 0.09	-0.19 ± 0.0078	-0.53 ± 0.0041
2.5 ms	-0.48 ± 0.13	-0.42 ± 0.0038	-1.08 ± 0.14
1.2 ms	-1.04 ± 0.17	-0.84 ± 0.121	-2.15 ± 0.41

Table 4.2.: Influences of gradient repetition time (T_R). Measured prompt coincidence countrate change in percent (mean ± SD, n=3) The amplitude was 20 mT/m and the gradient duration was 1 ms.

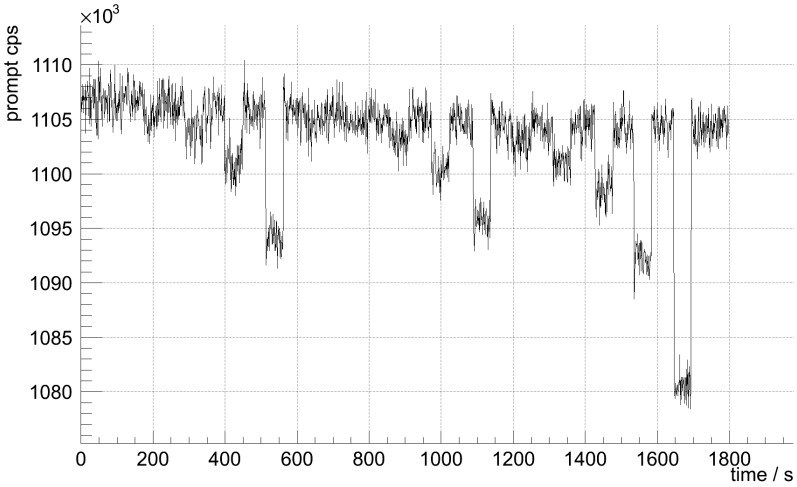

Figure 4.7.: Measured prompts coincidence countrate at varying TR according to Table 4.2.

Influence of Gradient Rise Time The influence of the gradient rise time was studied with unit rise time values of 6.5, 15, and 30 μs/mT/m. In order to reach the top of the gradient even at longer rise time, the pulse duration of 2 ms was used, the T_R of 2.5 ms and the amplitude of 20 mT/m. Increasing the rise time to 50, 75 and 100 μs/mT/m, the trapezoid gradient degenerates to a triangular shape ($t_{\text{flattop}} = 0\,\text{s}$). In the last two settings, the maximum amplitude is limited to 10 and 5 mT/m, respectively. The duration of each sequence was 57 s, with a pause of 60 s. In contrast to the amplitude and repetition time, variations in unit rise time did not cause a linear dependency of the rise time over the tested range (Table 4.3). The PET count rate showed an expected characteristic for variations of unit rise time in G_z. The most severe drop of 1.2 % was found for the fastest unit rise time of 6.5 μs/mT/m with the gradient in z-direction. For G_x and G_y the countrate reduction was also reproducible for all parameters, and the characteristics for G_x and G_y were similar. However, a linear dependency between the countrate reduction of the PET data and the increasing slope was only found as long as the gradients had a trapezoid shape and the rising and falling edges were well separated by the flattop. For a unit rise time of 50, 75 and 100 μs/mT/m and a triangular gradient shape, the countrate reduction was found to be more severe than for trapezoid gradient shapes.

Gradient	G_x(%)	G_y(%)	G_z(%)
6.5 μs/mT/m	-0.51 ± 0.011	-0.46 ± 0.018	-1.2 ± 0.078
15 μs/mT/m	-0.22 ± 0.022	-0.23 ± 0.032	-0.31 ± 0.041
30 μs/mT/m	-0.15 ± 0.041	-0.14 ± 0.041	-0.19 ± 0.043
50 μs/mT/m	-0.36 ± 0.038	-0.38 ± 0.021	-0.09 ± 0.007
75 μs/mT/m	-0.26 ± 0.029	-0.26 ± 0.031	-0.07 ± 0.0039
100 μs/mT/m	-0.21 ± 0.031	-0.17 ± 0.033	-0.06 ± 0.0079

Table 4.3.: Influences of gradient rise time (t_{rise}) on PET countrate. With rise times ≤ 50 μs/mT/m, the trapezoidal pulse degenerates to a triangular pulse.

4.4.2. Gradient Superposition

Investigating the linear superposition of the gradient directions it was shown that the countrate drop increases when gradient fields originating from different gradient coils are switched simultaneously (see Table 4.4 and Figure 4.9).

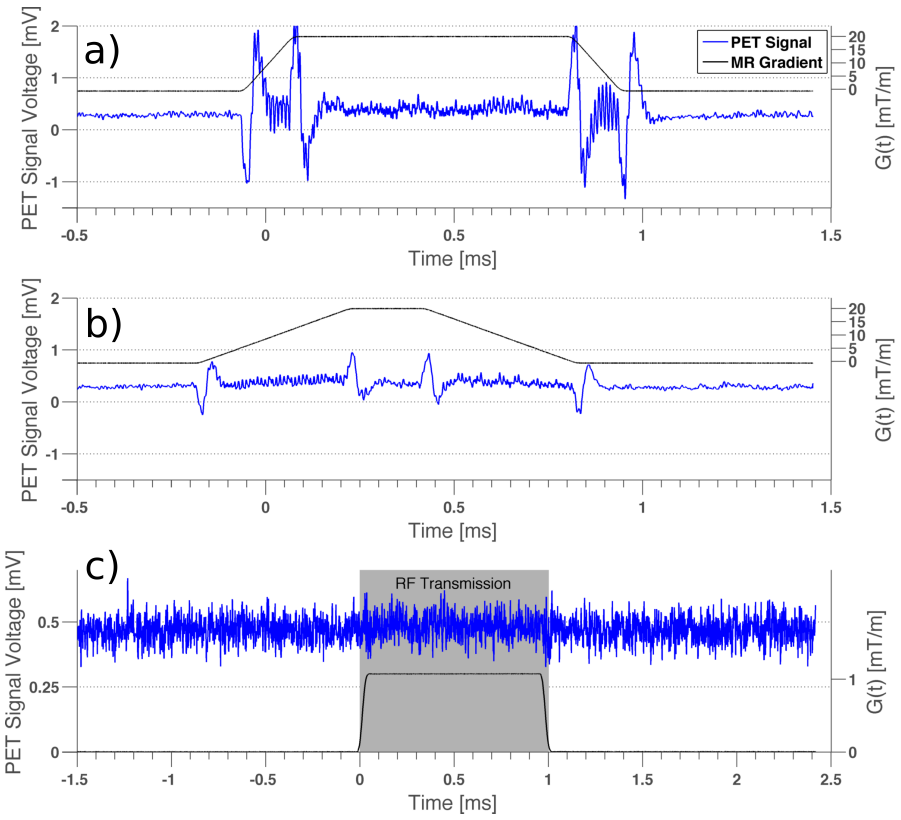

Figure 4.8.: Analog PET detector signal during execution of gradients with short rise time (6.5 μs/mT/m), Figure (a) and long rise time (30 μs/mT/m), Figure (b). The transmission of RF pulses showed no influence on the PET detector signal (c) [104].

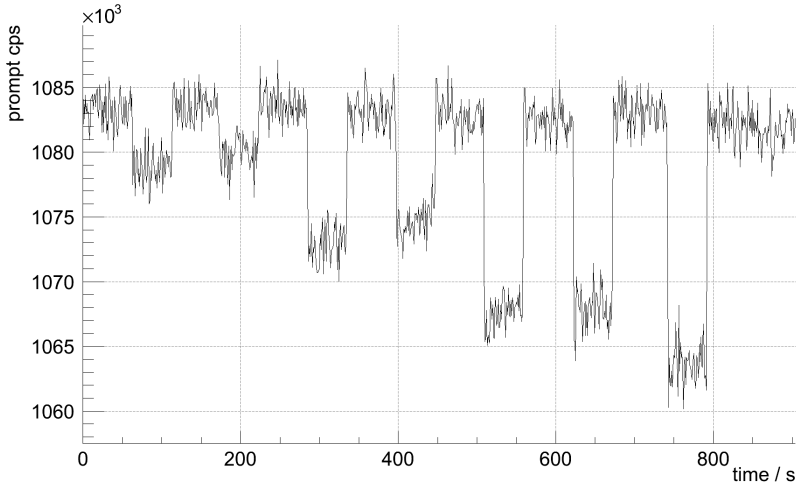

Figure 4.9.: PET headcurve during switching of MR gradients in different combinations of G_x, G_y, and/or G_z as described in Table 4.4.

Thus, the total prompts countrate reduction (ΔP) caused by simultaneously switched G_x, G_y, and/or G_z corresponds to the sum of countrate reductions caused by the single gradients switched separately according to

$$\Delta P(Gx + Gy + Gz) = \Delta P(Gx) + \Delta P(Gy) + \Delta P(Gz). \tag{4.2}$$

Gradient	Measured Value	Calculated Value
G_x	0.41%	–
G_y	0.33%	–
G_z	0.99%	–
$G_x + G_y$	0.81%	0.74%
$G_x + G_z$	1.38%	1.40%
$G_y + G_z$	1.35%	1.32%
$G_x + G_y + G_z$	1.79%	1.73%

Table 4.4.: Prompt coincidence countrate reduction for superposition of gradients fields in all combinations.

As a source for the countrate reduction, the switching gradients were found to induce an additional signal to the baseline of the PET detector signal during ramp up and ramp down (Figure 4.8 (a) and (b)). The signal is proportional to dB/dt,

i.e. the first derivative of the gradient, and provides a basic explanation of the findings of the previous experiments, varying gradient amplitude, repetition time and rise time. Consequently, rising and falling gradient ramps give rise to mirrored PET signals, as evident in Figure 4.8 (a). The oscillations seen by the analog PET detector signal explain the finding that triangular gradient pulses may have stronger effects on the PET countrate. With a flat top time of the gradient close to zero, induced signals of the increasing and decreasing gradient superimpose. This results in analogy to wave theory in constructive or destructive interferences affecting the PET countrate to a higher or lower extent. It depends on the gradient rise time as a global parameter as well as on the frequencies and phase difference of the induced analog PET signals.

4.4.3. Influence of RF Pulses

The impact of RF pulses was studied with the ^{68}Ge-cylinder phantom located inside the two RF head coils. In this test, sequences consisting of RF pulses only (no MR gradients) were performed. The flip angle and thus the amplitude of the transmitter voltage was tested for 100 V, 200 V, 300 V, 400 V and 500 V with durations of the RF pulses varying from 0.5 ms up to 1.5 ms, which is equivalent to flip angles of up to 625° *in vivo*. With this setup the MR scanner was operated at the maximum allowed SAR level. Each specific parameter set was tested for one minute of repeated RF pulsed with minimal possible spacing (dictated by the SAR limits). The RF pulses showed no measurable effect on the countrate, neither on the single block counter nor on the prompt or delayed coincidences, even when reaching the maximum SAR allowed by the MR scanner hardware (see Figure 4.8 (c)). Furthermore, no effect of the RF transmission on the PET temperature was observed.

4.4.4. Influence of Temperature

APDs are known to be sensitive to variations of temperature [30]. The increase of temperature in the detector cassettes is a secondary effect, caused by eddy currents induced by the temporally changing magnetic field gradients. The observed increase of temperature during standard measurements is simulated by a controlled variation of the temperature of the air flow by changing the cooler temperature. In order to measure under steady state conditions, the time between temperature adjustments and measurements was 1 hour. The effect on the PET data

was analysed. One temperature sensor is located within each detector cassette near the detector electronics and can be read out from the PET console. The air temperature within the detector cassettes is usually kept at the nominal value of 306 K (33°C), employing temperature-controlled airflow. Experiments, in which the cooler temperature was adjusted manually, revealed a small dependency of the countrate on the temperature with variations from -0.5 %/K to -1%/K. Running clinical MR sequences with standard parameters, the temperature control restricts temperature fluctuations within a range of $\Delta T = \pm 0.6$ K about the nominal temperature. The steepest temperature slope of still less than 0.1 K/s was observed during DTI sequences with an EPI readout. The temperature dependent countrate variations show a delayed and retarded decrease compared to the instantaneous countrate drops induced by the gradients with values up to 4 %/s. Thus, the sequence related temperature variations in the cassettes can be minimised or excluded as a cause of the immediate countrate reduction.

4.4.5. Conclusions

The influence of MRI on PET during simultaneous measurements with the Siemens 3T MR-BrainPET has been investigated and described as function of relevant MR parameters. The parameters include the influence of the static B_0 field, the RF field as well as the direction, amplitude, rise time and repetition time of the gradient fields. The gradient fields were identified as the primary source of countrate reduction of a few percent during simultaneous MR-BrainPET measurements. The main reason is the distortion of the analog signals on the PET hardware. This affects the baseline signal during the ramping of the MR gradients. RF pulses were found to have no measurable influence. However, future designs of hybrid MR-PET scanner may further reduce the reported decreases of countrate by appropriate changes in detector hardware, such as optimisation of the analog boads for filtering the PET detector signal.

5. Procedures for Quantification of PET Images

Parts of this chapter have been published in [104, 107, 105].

The coincidence data acquired with a PET scanner contain information about projections of the tracer distribution and can be used to reconstruct 3D images. However, the measured and uncorrected prompt data P_{ij} are affected by different sources of errors compromising the image quality and quantification. Corrections essential for PET are:

- Normalisation ($N_{i,j}$)
- Random Correction ($R_{i,j}$)
- Attenuation Correction ($A_{i,j}$)
- Scatter Correction ($S_{i,j}$)
- Normalisation for Scattered Events ($N_{i,j}^{scat}$)
- Deadtime Correction ($D_{k,l}$)
- Pileup Correction ($U_{i,j}$)

The development and optimisation of methods for quantitative PET imaging together with evaluation and implementation in a reconstruction framework are described in the following. The different corrections contribute to the estimated true number of coincidences $T_{i,j}$ in a specific LOR connecting the crystals i and j, which are mounted on the blocks k and l, respectively, according to

$$\mathrm{T_{i,j}} = (\mathrm{P_{i,j}} - \mathrm{R_{i,j}}) \cdot \mathrm{N_{i,j}} \cdot \mathrm{A_{i,j}} \cdot \mathrm{D_{k,l}} \cdot \mathrm{U_{i,j}} - \mathrm{S_{i,j}} \cdot \mathrm{N_{i,j}^{scat}}. \tag{5.1}$$

This formula is used when pre-correcting the data prior to reconstruction. However, in order to avoid a bias in low statistics frames and the reduction of noise

in the reconstructed images the correction parameters have to be included in a reconstruction model, rather than pre-correcting the data (see [63, 62] and Section 2.5.2). The central limit theorem states that a sufficiently large number of independent random variables with a finite mean μ and variation σ can be approximated by a Gaussian distribution. For additive contributions such as random and scattered coincidences, the propagation error for the variance is given by

$$\sigma_{A+B} = \sqrt{\sigma_A^2 + \sigma_B^2}. \tag{5.2}$$

It is crucial to determine the corrections as accurately as possible, not only to improve the quantitative accuracy and to eliminate systematic artefacts, but also to reduce the noise within the image. With long acquisition times it is possible to obtain data with low statistical variance. Methods wich are applicable to measured corrections, such as the normalisation or the random correction, are variance reduction (VR) algorithms.

5.1. Random Correction

The rate of detected random coincidences (Section 2.4.7) is a function of the singles countrate. The described background becomes more prominent with increasing countrates (see Figure 5.1) and leads to a reduced contrast. Since the rate of random coincidences is proportional to the length of the timing window and proportional to the activity within the FOV, a good temporal resolution is crucial in order to keep the random coincidence rates low.
Random correction is a major correction in PET and several methods are available. A first method proposed for random correction was the constant background subtraction [94]. This method can be used to verify the remaining background in the data, when estimated randoms are compared to the randoms in the prompts outside the object. Furthermore, it can be applied as a second order random correction to provide a better data basis for the scaling of the scatter sinogram. The classical approach determines the random coincidences from measured single event rates of each crystal, which also reduces the noise in the data [8]. Here, a channel connecting the crystals i and j with the single rates S_i and S_j, respectively. With a coincidence time window of 2τ the random rate can be estimated by

$$R_{i,j} = 2\tau S_i S_j, \tag{5.3}$$

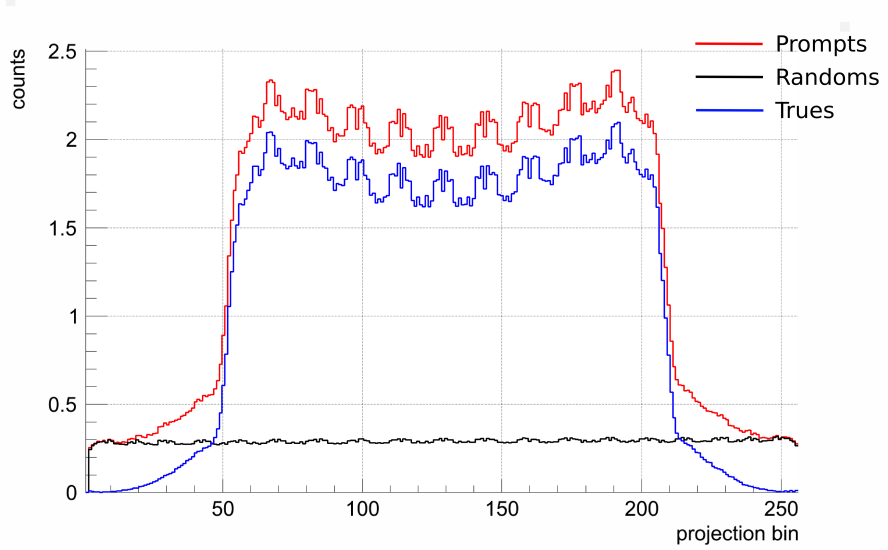

(a) Profile of sinograms at low countrate

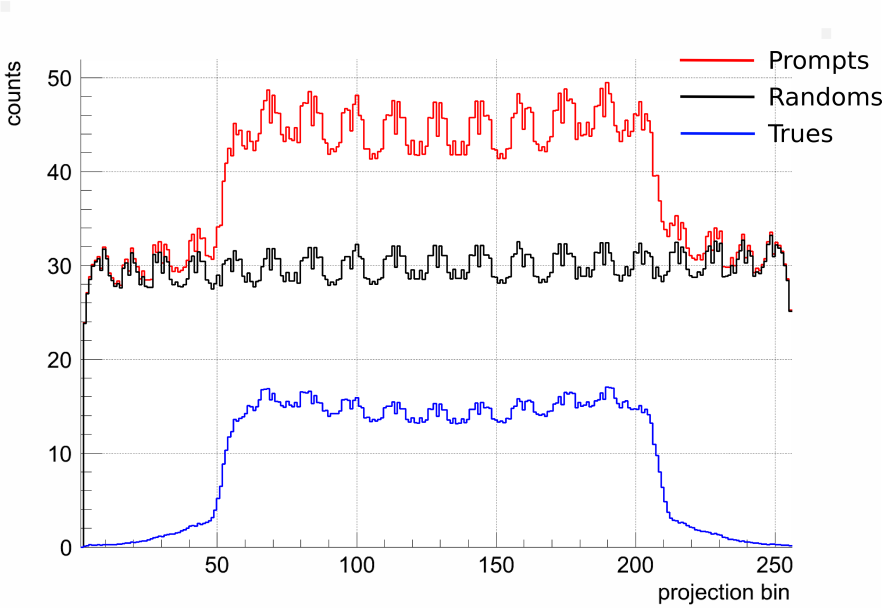

(b) Profile of sinograms at high countrate

Figure 5.1.: Radial profile of sinograms with high (b) and low (a) total countrate. The constant background caused by the random coincidences (black curve) has a vital contribution at high countrate.

where τ is set according to the range of the timing resolution of a detector block. The advantage of this approach is that the singles rates possess much lower statistical uncertainties compared to the measured delayed coincidence rates when using the delayed window approach (DW). This reduces the variance in the estimated randoms. Today's PET scanners implement a delayed window. To estimate the constribution of the random events contained in the prompt coincidences, usually an additional but delayed timing window detects random coincidences in each channel. These measured coincidences comprise two singles events with a time difference significantly beyond the coincidence timing resolution of the scanner. Thus, the delayed window technique only samples random events and provides an estimate of the amount of random coincidences contributing to the prompt coincidences for each LOR. The decomposition of single events from measured delayed coincidences holds the advantage that prompts and delayeds experience the same deadtime effect.

However, the direct subtraction of randoms measured in the DW results in a bias especially for short measurements [101]. Consequently, the measured delayed coincidences are further processed using variance reduction techniques. This is important for quantification in short dynamic frames with low overall count sum. Applying the ordinary Poisson model for iterative reconstruction together with the VR randoms this bias can be significantly reduced. One approach which has been implemented for the BrainPET is the variance reduction on random coincidences (VRR) from delayed coincidence histograms firstly applied for the Siemens HRRT (High Resolution Research Tomograph) [17]. In order to preserve the crystal efficiencies and the deadtime properties of the DW coincidence data, some adaptions of Equation 5.3 have to be made.

Firstly, the expected single rates have to be found. Starting from uncorrelated singles acquired with the DW method this algorithm finds iteratively the crystal single rates compatible with the delayed coincidence events S_j. Finally, the classical Equation 5.3 is applied [17].

The method has been validated with a ^{68}Ge-cylinder measurement with an activity of approximately 50 MBq. Data have been acquired in LOR-histogram mode for 10 min and 8 h. Figure 5.2 indicates the performance of the algorithm, comparing the VRR processed data from the 10 min scan with the acquisition of a 8 h scan. It can be clearly seen that the crystal efficiencies are maintained (Figure 5.2(b)). Furthermore, the 10 min VRR data have an even reduced noise level compared to the 8 h acquisition (Figure 5.2(c)). Since the VR algorithm is not expected to induce systematic structures in the sinogram data, the difference image is expected

to exhibit noise with the mean value of zero (Figure 5.3).
Besides the sensitivity pattern of the VRR and the conservation of counts it is important to verify the influence of randoms on the reconstructed images with a quantitative analysis. Data of the described ^{68}Ge-cylinder phantom were acquired with different acquisition times and were reconstructed applying only normalisation (CBN) and attenuation correction. Scatter is not corrected, since it may further bias the evaluation due to a more problematic tail fit on low count frames. However, scatter fraction is assumed to be constant for a fixed geometry, thus not affecting the evaluation. From the diagram in Figure 5.4 it can be seen that the VRR algorithm performs much better than the delayed window approach, especially for low statistics frames.
Due to implementation issues, the prompts and delayeds window may have different sensitivity which also has to be taken into account by a global scaling factor. Performing digital coincidence processing, the time stamp has a limited precision, leading to a temporal quantisation. The precision is defined by the least significant bit (LSB) of the time stamp and a maximal resolution of τ_{LSB}. Singles from two blocks are defined to be in coincidence if their timestamps do not differ more than W, with $W \cdot \tau_{LSB}$ usually in the range of the temporal resolution of the block. The effective coincidence window size for accepting the two singles as a coincident event is thus $(2W+1) \cdot \tau_{LSB}$. Here, the clock cycles have a defined length of $M \cdot \tau_{LSB}$ and the implementation of the DW is realised that events from different clock cycles are not detected as coincidence. Therefore, random coincidences contained in the prompts window is slightly reduced to the ones in the delayed window [96]. For the APD based BrainPET the measured timing resolution of one detector was found to be below 5.9 ns FWHM. Therefore, the coincidence window for the BrainPET was set to $2\tau = 12$ ns. Due to this relatively large coincidence window, a high rate of random coincidences is accepted and has to be corrected (see Figure 5.1). Figure 5.5 shows the measured sensitivity of randoms in the prompt window and the delayed window, compared to the theoretically computed value. The fitted value of $0.96298 \pm 2.26 \cdot 10^{-5}$ is in good agreement with the computed value of 0.96194. At very low countrates, the peak tracking algorithm fails and the sensitivity of the two windows starts to diverge. However, this range of countrates is not relevant for human studies.

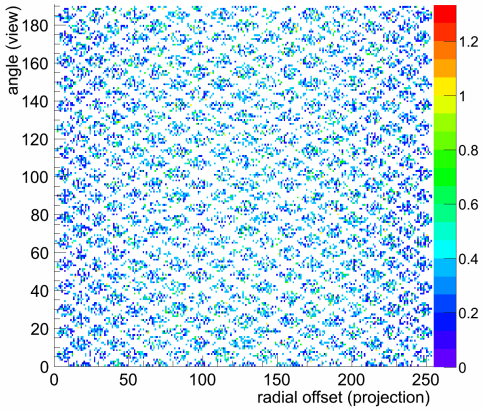

(a) Delayed coincidences of 10 min acquisition time, measured in the delayed window (DW).

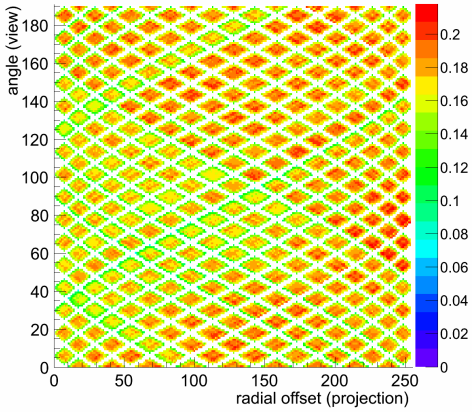

(b) Variance Reduced Randoms (VRR) from the 10 min scan (in Figure (a)).

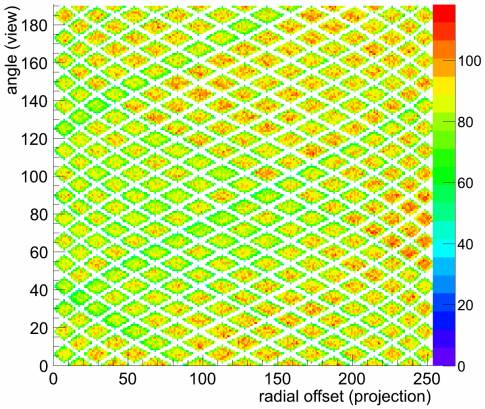

(c) Delayed coincidences of 8 h acquisition time, measured in the delayed window (DW).

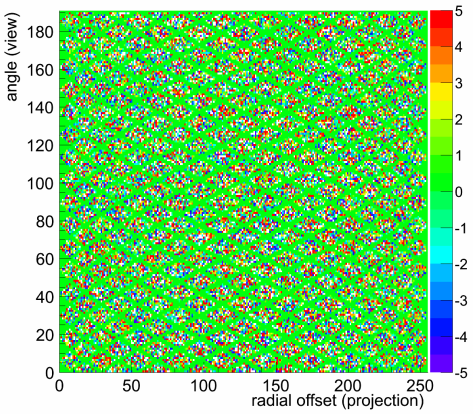

(d) Difference image of VRR and DW method.

Figure 5.2.: Depiction of sinogram planes of a cylinder measurement. Figure 5.2(a) shows a 10 min acquisition with the DW method, the same data are processed with the VRR method and displayed in Figure 5.2(b). For comparison, a 8 h acquisition of delayed coincidences is shown in Figure 5.2(c). The difference image of VRR and DW method is depicted in Figure 5.2(d).

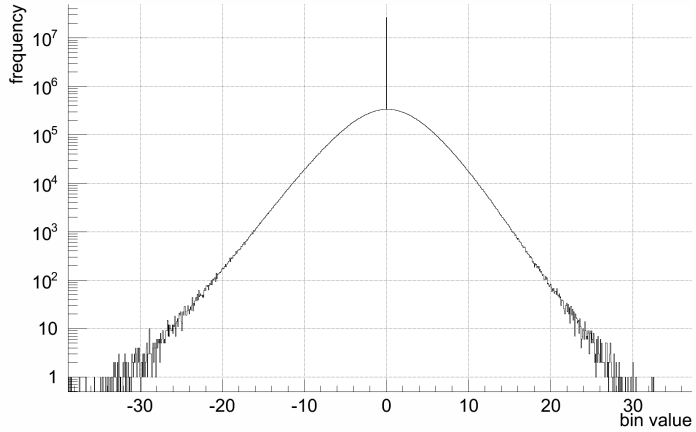

Figure 5.3.: Histogram of difference between measured delayeds and VRR sinogram in logarithmic scale. Most of the bins show values close to zero. The broad distribution of non-zero values is due to noise, as also visible in Figure 5.2(d).

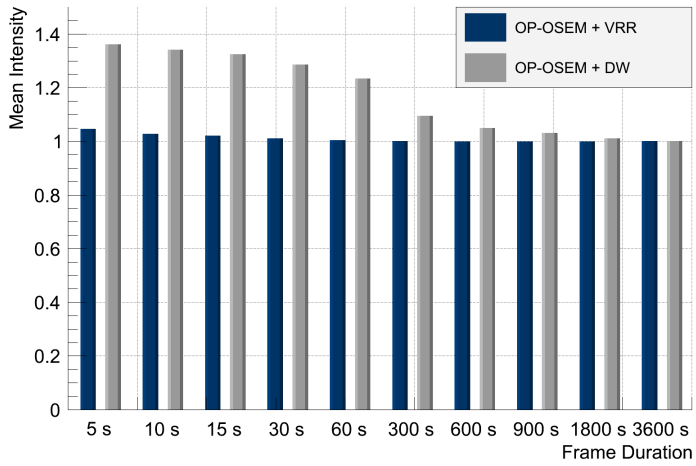

Figure 5.4.: Bias in random corrected images with low count sum. Quantitative comparison in reconstructed images using DW and VRR method.

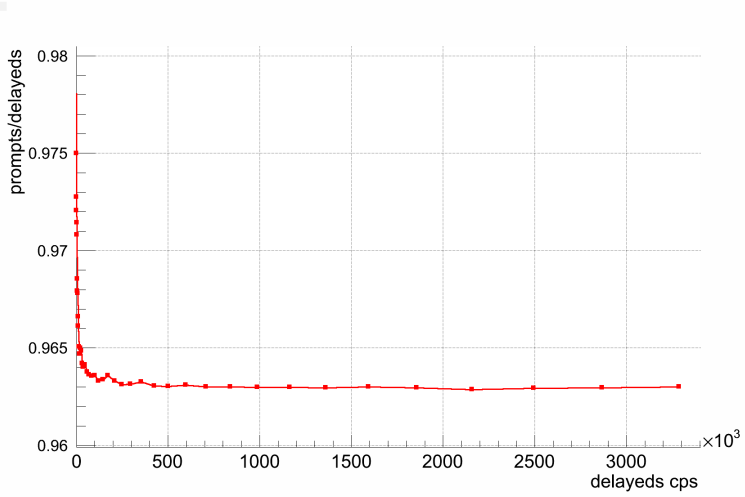

Figure 5.5.: Sensitivity ratio of prompt and delayed window (DW) to random coincidences. The fitted value of $0.96298 \pm 2.26 \cdot 10^{-5}$ is in good agreement with the computed value of 0.96194.

5.2. Attenuation Correction

The correction of emission data in PET for photon attenuation by tissue and device materials within the FOV is mandatory in order to obtain homogeneous and quantitative images. In general, the attenuation of photons depends on the transmission length l and the electron density of the material (e.g. bone, soft tissue, air, plastic) expressed by the linear attenuation coefficient μ. Furthermore, it depends on the photon energy [18]. The intensity $I(l)$ of a photon flux with initial intensity I_0 decreases exponentially with the thickness l of the travelled path through material by

$$I(l) = I_0 \mathrm{e}^{-\int_L \mu(E,l)dl}. \tag{5.4}$$

Two annihilation photons emitted in PET after positron decay may pass different materials and thus may be attenuated with different probabilities. However, the overall attenuation coefficient (AC) within a LOR defined by two detectors d_1 and d_2, with L_1 and L_2 defining the distance from the annihilation point to detector d_1 and d_2, respectively, reads

$$AC_{\mathrm{LOR}} = \mathrm{e}^{\int_{L_1} \mu(l)dl} \, \mathrm{e}^{\int_{L_2} \mu(l)dl} = \mathrm{e}^{\int_{\mathrm{LOR}} \mu(l)dl}. \tag{5.5}$$

Thus, the AC is invariant with respect to the exact origin of annihilation along the

LOR does not effect the attenuation coefficient. As a consequence the attenuation properties of each LOR are independent of the activity distribution within the subject and depend only on the line integral of μ along L. The condition makes a separation of emission and transmission properties possible, unlike in SPECT. This is exploited in PET and PET/CT by measuring the transmission properties of the subject for each LOR with external sources. Thereby, the attenuation correction factor for a specific LOR is defined as

$$AC_{\mathrm{LOR}} = \frac{I_0}{I(l)} = \mathrm{e}^{\int_{\mathrm{LOR}} \mu(l) dl}. \tag{5.6}$$

In conventional PET, the attenuation properties for each detector combination are measured with transmission sources with positron emitters or gamma emitters close to 511 keV. One or multiple rotating radiation sources are placed outside the subject. For sources with energies different from 511 keV the attenuation factors have to be scaled. For PET/CT, the x-ray CT data represent a transmission scan at photon energies significantly lower than 511 keV. The CT image is converted to an attenuation map by a piecewise linear mapping of the CT intensities [18]. Problems here are mis-positioning due to motion, truncation artefacts and the proper scaling of the attenuation coefficients as a function of energy.

5.2.1. Attenuation Correction of Human Tissue

For hybrid MR-PET scanners, the hardware for transmission scans is not available due to the limited space for a rotating transmission source and because moving objects are prone to cause artefacts in the MR images. Consequently, the individual correction factors need to be derived from MR images of the scanned subject. However, the MR images represent proton densities weighted with relaxation times of the excited spin ensembles, rather than electron density. Thus, computing the AC from MR images requires advanced procedures. Up to now, several different approaches exist to assign an attenuation coefficient to each voxel in the PET image space. So far, these procedures have different advantages and disadvantages regarding, for example, accuracy or robustness. Since this extensive topic of ongoing research is beyond the focus of this work, the methods currently discussed in the literature are presented shortly.

One approach is the combination of local pattern recognition and atlas registration to predict pseudo CT images. A knowledge based segmentation approach applied on T_1-weighted MR images examines the tissue membership and position and segments differing regions [40, 10, 11, 89]. Another method focusing on the bone-air

segmentation from MR images applying a dual echo UTE sequence (DUTE) for imaging of the head [48, 20]. With the ultra short echo time, even solid structures as the case of the RF coil, but also the desired bone structure become visible. Also the extraction from attenuation information from emission data is possible [84]. A template-based approach applying a PET transmission scan template by adapting it to the individual subject's head uses warping algorithms [82]. The method avoids scaling of attenuation coefficients as a function of energy, since a transmission template is used. On the other hand, individual anatomical structures of the subject may not be addressed as accurately as with other methods. However, the templates are used in routinely performed human studies with great success and excellent practical usability. Since all of the currently presented procedures have still shortcomings, the development of MR based attenuation correction is still in progress [39, 49]. Maybe the combination of features holds the potential for a more general but practical approach. A prerequisite is the further development and optimisation of MR sequences for bone-air separation.

5.2.2. Attenuation Correction of RF Coil

In hybrid MR-PET imaging, not only the subject itself causes attenuation, but also the RF coils located between the subject and the detector. The attenuation map that needs to be applied to account for the attenuation of the RF coil has to be found only once. It is not subject or scan dependent assuming the accuracy of repositioning within the limits of the detector resolution. For some clinical applications, mostly whole body MR-PET, the attenuation optimised surface coils are neglected, compared to the severe attenuation of the body [98]. However, is has been reported that these coils can cause streak artefacts [59] and the data should be corrected for the effect of these local coils in whole body applications [73].
Especially for the BrainPET, the correction of the solid head coil with its regular structure and its fixed position is a prerequisite for artefact free images.
Besides the exact registration of the coil template, the determination of the correct attenuation coefficients are a prerequisite for obtaining artefact free images. For the correction of the RF coil with its sharp structures, it is crucial to account for the locally varying image resolution. Adaptions for manipulation of a measured coil attenuation map are:

- Find best position of the coil template (CT or HR+)
- Model image resolution appropriately

- Scaling attenuation values

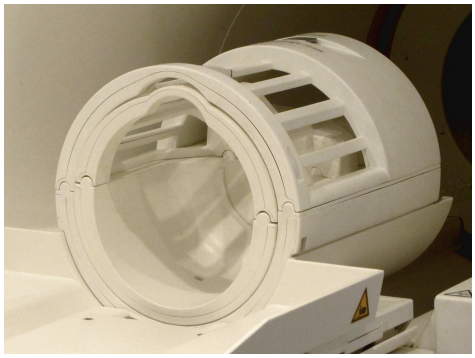

(a) 3T MR headcoil

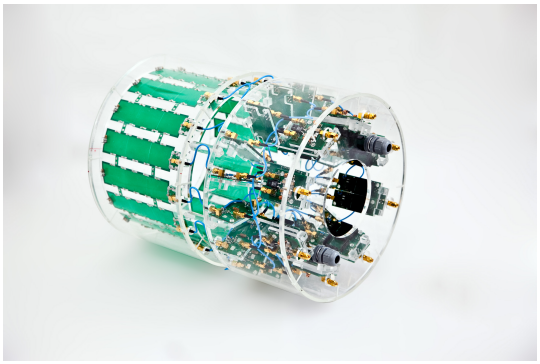

(b) 9.4T MR headcoil

Figure 5.6.: Different shapes and materials for head coils, as applied in the 3T (a) and 9.4T (b) MR-BrainPET scanners.

Two attenuation maps were analysed here for coil correction. One was acquired in a transmission scan with the Siemens HR+ scanner. It has the advantage of the correct photon energy of 511 keV, but the disadvantage of a resolution of about 10 mm at the relevant structure (see Figure 5.7 (c)). The second template was acquired with an x-ray CT, which has a much higher reconstructed image resolution but on the other hand is measured at much lower photon energy (see Figure 5.7 (a)). So both of the templates are not optimal to correct for 511 keV photons at a resolution of 3 to 5 mm for the BrainPET. Several filters and scalings have been applied in order to find the optimal coil template values.
The best performance compared to the standard approach of directly using a template measured with the HR+ scanner was achieved applying the scaled HR+ template by a factor of 1.6. For this, it was possible to further improve the image quality. However, compared to PET measurements without a coil within the FOV, there is still some room for improvement, e.g. considering the Compton scatter in the model for the coil.

5.3. Compton Scatter Correction

Annihilation photons emitted within a subject pass tissue before their detection (Section 2.3.2). By interaction with an electron from the outer shell of the tissue

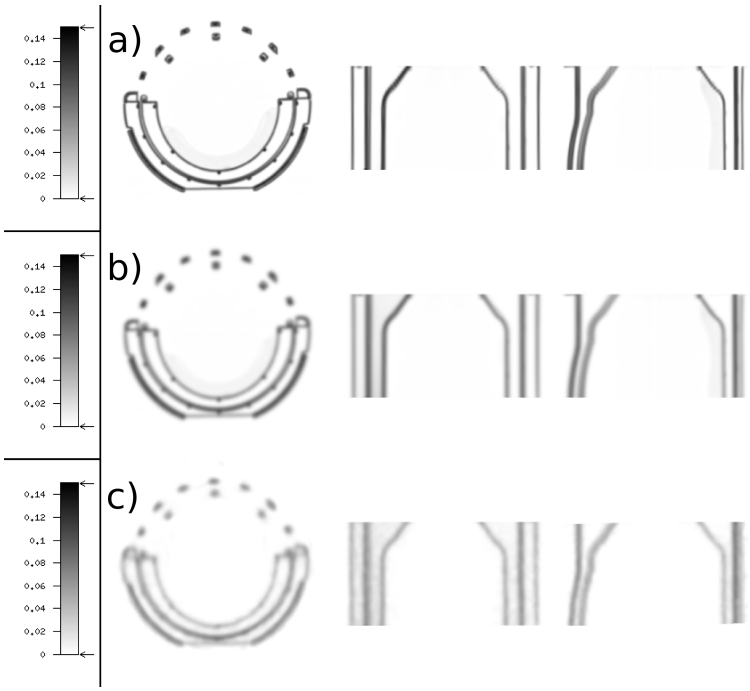

Figure 5.7.: Attenuation maps of RF headcoil in Figure 5.6(a) showing a CT scan (a), the HR+ transmission scan scaled by factor 1.6 (b) and the measured HR+ transmission scan (c).

atoms the photon is deflected and loses energy. The main fraction of the photons are scattered forward with only a slight loss of energy. Photons with a severe change in direction associated with a high loss of energy may be rejected due to the detectors energy discrimination. The effect of Compton scattering is dominant in PET and results in a decreased image contrast. Due to the limited energy resolution of the PET detectors, not all scattered events can be rejected without losing unscattered 511 keV photons. Thus, simulations have to be performed to estimate correction terms. In standard 3D acquisition mode, for which the scatter fraction is 30 to 50 % scatter simulation is challenging. A computationally fast 3D Single Scatter Simulation (SSS) algorithm estimates the expected single scatter coincidence rate within the detector pair where only one of the two coincidence photons is assumed to be scattered. Higher order scatter is less likely to appear, especially in brain scans. The scatter distribution in the scatter volume is computed by the volume integral of a scattering kernel over the scattering medium.
The cross section for the corresponding energies is derived from the Klein-Nishina formula [102, 103]. The detection efficiency is dependent on the angle of incidence as well as on the energy. Therefore the normalisation of true coincidences is not valid for scattered events.

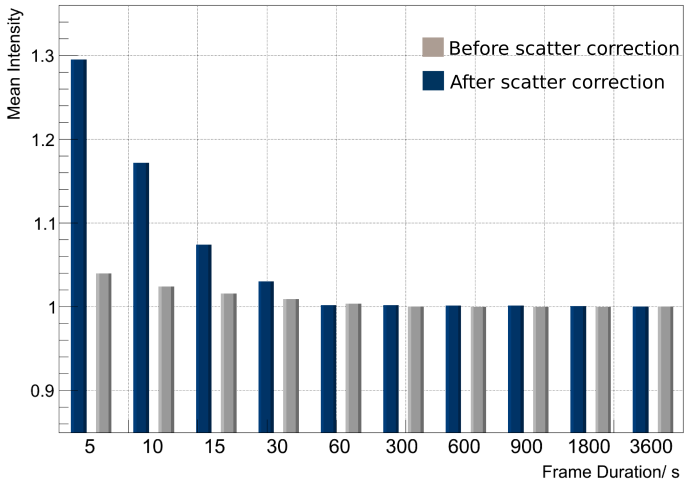

Figure 5.8.: Bias in scatter corrected images with low count sum (blue bars), compared to the images without scatter correction. The plot shows the relative deviation of each series from its 3600 s measurement (grey bars).

In order to assess the robustness of the scatter correction against statistical uncertainties, an experiment was performed to see the quantitative accuracy of the scatter estimation. The cylinder filled with ^{68}Ge is measured in listmode and subdivided into frames of different length. The longest frame contains the counts of 3600 s and the shortest one only 5 s (see Figure 5.8). The data is reconstructed applying two procedures, one without scatter correction (grey bars) and one including scatter correction (blue bars). The reference for each series is the 3600 s measurement. A bias in scatter corrected images with low count sum, compared to the images without scatter correction is up to 29 % [107]. This appears only in very short frames in the cylinder measurement and has not been observed in human studies in this extend. Nevertheless, the correction should be improved in future developments to overcome the quantification error in low count sum frames. The scatter simulation assumes a true emission image as input, which, however, can only be computed with knowledge of the true scatter distribution. Thus, several iterations of reconstruction and scatter simulation are required in order to approach the unbiased scatter distribution and to reconstruct the appropriate emission images. The first emission image, which is not corrected for scatter, shows an overestimation of the activity in the centre of the object and, thus, the scatter based on this image is overestimated in this region. The image subtracted for scatter suffers from an underestimation of activity in the reconstructed image (Figure 5.9, 1st iteration). Subsequently, this image given as an input to the 2nd scatter simulation leads to an underestimation of scatter (Figure 5.9, 2nd iteration). With increasing number of iterations of reconstruction and scatter estimation the oscillation around the true estimation is damped and acceptable values are achieved after 3 to 5 iterations in case of the cylinder as shown in Figure 5.9, red curve.
However, the iterations of the scatter simulations are computationally extensive and time demanding, which is not practical in clinical routine of dynamic acquisitions with multiple frame reconstruction. A shortcut to a true estimation is the computation of a more correct emission image by averaging the overcorrected image from iteration 1 and the undercorrected image from iteration 2 and giving this as the input of the scatter correction [42]. This leads to a more stable solution in the subsequent iterations dampering the oscillations and leading to a faster convergence (see Figure 5.9, black curve).

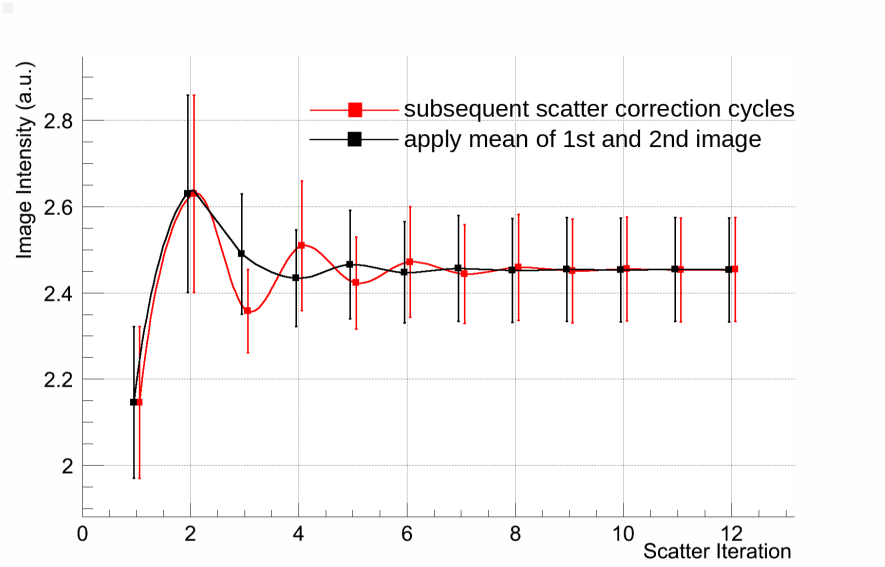

Figure 5.9.: Mean image intensity as function of reconstruction cycle. The values are given as mean and standard deviation of the intensity distribution among the reconstructed cylinder image. The red curve shows the standard procedure using the output of the prior iteration as input for the next one, whereas the black curve shows the outcome, when at iteration 3 the input is computed by averaging output of 1 and 2. (Data points are slightly shifted for better visualisation)

5.4. Normalisation

The thousands of crystals mounted on several rings around the FOV exhibit varying sensitivities. Combining crystals with varying detection efficiencies results in LORs with inhomogeneous detection efficiencies among the detector. In theory, different components of efficiency can be identified and described. The crystal detection efficiency ε_i represents the manufacturing variance whereas the geometric component $g_{i,j}$ describes the different sensitivity of a LOR due to different angles between the crystal surface and LOR. The differences in the geometric component can be seen clearly in Figure 5.10, where direct opposing heads (Figure 5.10(a)) and oblique opposing heads (Figure 5.10(c)) were in coincidence, showing different shading patterns. The procedure to correct for these sensitivity variations is referred to as normalisation. A normalisation factor n for the sensitivity within an LOR or sinogram bin is composed of

$$n_{i,j} = \frac{1}{\varepsilon_i \cdot \varepsilon_j \cdot g_{i,j}}. \tag{5.7}$$

For the correction of all measured channels, an LOR-file or sinogram with a correction value for each channel is provided. Variations with changing countrate may also be considered in a dynamic normalisation n_{dyn}, which accounts for the deadtime d_b of each detector block b and pileup p effect (see Chapter 5.5) [7]

$$n_{dyn,i,j} = \frac{n_{i,j}}{d(b_i) \cdot d(b_j) \cdot p_i \cdot p_j}. \tag{5.8}$$

Computing the normalisation factor for a sinogram bin, the sum of correction values has to be build before inversion, as described in Chapter 5.5.3. In more sophisticated models, true and scattered coincidences have distinct normalisation coefficients [7, 9].
Shortcomings or inaccuracies in the normalisation lead to severe image artefacts. The validity of normalisation is a matter of dailyQC and has to be controlled carefully.
A plane source measurement is applied to acquire the normalisation data for the BrainPET. An homogeneous source is measured in 16 different positions (due to the 32 cassettes of the BrainPET), stepped by an airmotor. The data from the 16 different views is merged into one LOR file, taking the data from LORs most perpendicular to the plane source of every view. In constrast to a cylinder measurement, this method has the advantage that the entire FOV can be covered while keeping the scatter fraction at a minimum.

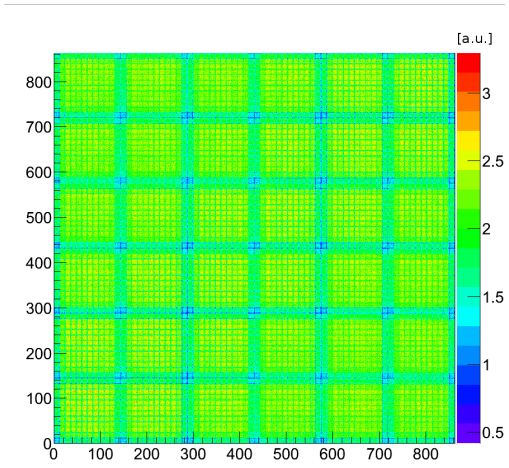

(a) Geometric component g of LORs from directly opposed heads with homogeneous illumination.

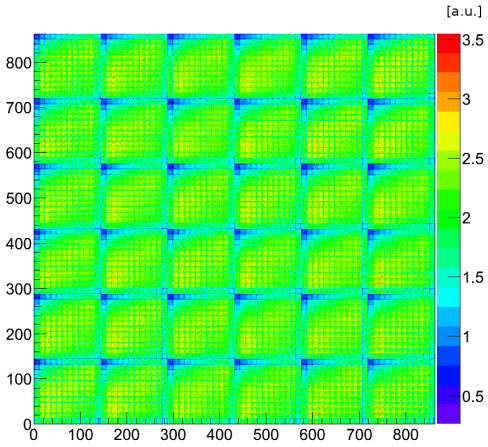

(b) Geometric component g of LORs from oblique opposed heads showing shading pattern.

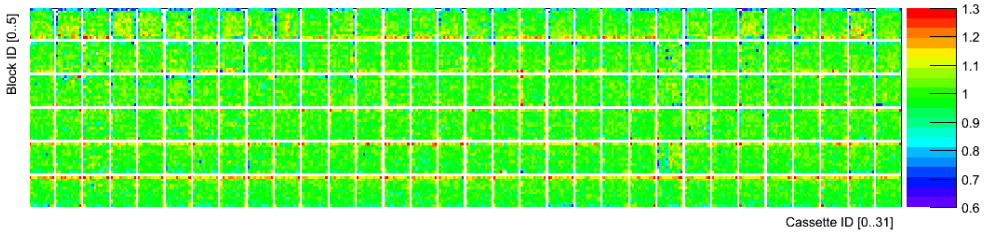

(c) Crystal efficiencies ε extracted from the component based normalisation.

Figure 5.10.: LOR values of head pairs of plane source based normalisation showing 864×864 values. The symmetries are used to extract the geometric component of the component based normalisation (CBN). They are separated from the crystal efficiencies ε.

Practically, two different concepts for processing of the normalisation scan exist, the direct normalisation (DN) and the component based normalisation (CBN). For DN all LORs are illuminated with a homogeneous source and the normalisation factors are assumed proportional to the ratio of expected counts to measured counts in each LOR [69]. Here, the normalisation coefficients $n_{i,j}$ are measured directly and the model is not fully exploited. Due to limited acquisition time normalisations processed with the DN procedure suffer from a high noise level in each channel, which directly propagates into the images.
A more accurate concept is the CBN, which distinguishes between the individual crystal efficiency ε_i and the geometric component $g_(i,j)$. The two components are obtained from the same normalisation scan, however the geometry of the scanner can be exploited. For the extraction of $g_(i,j)$, the symmetry of LORs is used in a way that all LORs with rotational or mirror symmetry are averaged in order to have a noise reduced estimate of the geometric component. The crystal efficiency ε_i can be obtained from the sensitivity of one crystal in all LORs. This also gives a variance reduced estimate for ε_i. With this procedure, the final norm file is computed applying Equation 5.7.
For the evaluation of the DN and CBN, a ^{68}Ge-cylinder phantom with an activity of approximately 50 MBq has been measured for 24 hours within the scanner. Head coils have been removed here to avoid further sources of artefacts. Image reconstruction applying attenuation, random and scatter correction is performed using DN and CBN, respectively. Both images were reconstructed using 2 subsets and 32 iterations (see Figure 5.11). The intensity values in the uncalibrated images are given in arbitrary units (a.u.). To assess the noise level in the images, a ROI was drawn with the size and position of the attenuation template of the cylinder. The coefficient of variance (CoV) as the standard deviation divided by the mean value served as the quantitative measure for noise in the image.
The images reconstructed applying the DN exhibit a higher noise level (CoV of 10.1 %) than the reconstruction with the CBN (CoV 8.9 %). Since the mean intensity values do not show significant differences (3.321 DN, 3.318 CBN) and the image reconstruction time is identical for both methods, the CBN is recommended to be used in the standard procedure. Interestingly, due to a suboptimal setup, the normalisation scan cannot cover adequately the inhomogeneities and the resulting images suffer from artefacts. This is true for DN as well as CBN corrected images. Performing a new setup, these effects have been significantly reduced.

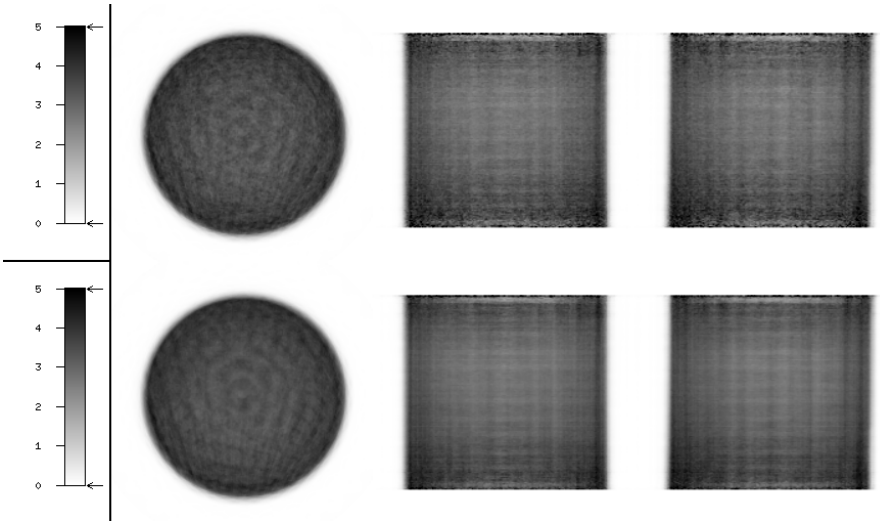

Figure 5.11.: Comparison of direct and component based normalisation in the reconstructed images. The noise level of the CBN is clearly reduced compared to the DN. With reduced noise, image artefacts are clearly visible and may be analysed further and have been reduced by the new setup (Section 4.2.3) as it can be seen in Figure 6.2.

5.5. Dynamic Effects

Photo counting systems, such as PET and SPECT suffer from the reduction of sensitivity at high countrates, since the capability of immediately processing subsequent events is limited. With increasing countrate, this becomes more pronounced. [109, 24]. Scanner designs take care to provide fast detectors and electronics with good capabilities in the high countrate regime [67, 6]. This, however, remains a trade-off between performance and costs. It is known that for commercially available PET scanners the deadtime effect is significant and additionally can vary for different detector blocks among the scanner. As described, the quantitative accuracy has to be achieved at all countrates of interest. For most human scans, the quantification during a high dynamic range of countrates is important, especially for studies which apply ^{11}C or ^{15}O with their short half lifes. Furthermore, deadtime and pulse pileup in PET scanners is influenced by the radioactivity distribution [24]. This justifies the effort of modelling these dynamic effects more accurately than a global scaling of the reconstructed images.
In order to obtain artefact free and quantitative images at a large range of countrates a method is designed which combines the corrections for deadtime and pulse

pileup as a function of unqualified singles on block level (CFD). An exponential correction model has been proposed to describe the deadtime of a PET scanner on block level [24] and adapted by a quadratic correction approach [97]. This has been extended to take into account also the mispositioning of events due to pulse pileup [9].

5.5.1. Global Deadtime Correction

Conducting and evaluating a cylinder phantom decay experiment with a high concentration of ^{18}F dissolved in water (half life of $T_{1/2} = 109\,\text{min}$) shows the global deadtime effect quantitatively (see Figure 5.5.1). The cylinder is axially and transaxially centred within the FOV and measured without MR coils to describe the effect for each detector block avoiding attenuation and scatter of photons on the coils. The measured total coincidence countrate as a function of acquisition time during the decay experiment exhibits increasing deadtime effect at high countrates at beginning of the decay experiment. The ideal countrate is not affected by deadtime. It is obtained by extrapolating the measured countrates from prompt coincidences at the end of the experiment, since deadtime is assumed to be negligible at very low countrates. The behaviour of an ideal scanner is modelled by extrapolation of low countrates with an exponential function, inversely to the radioactive decay.

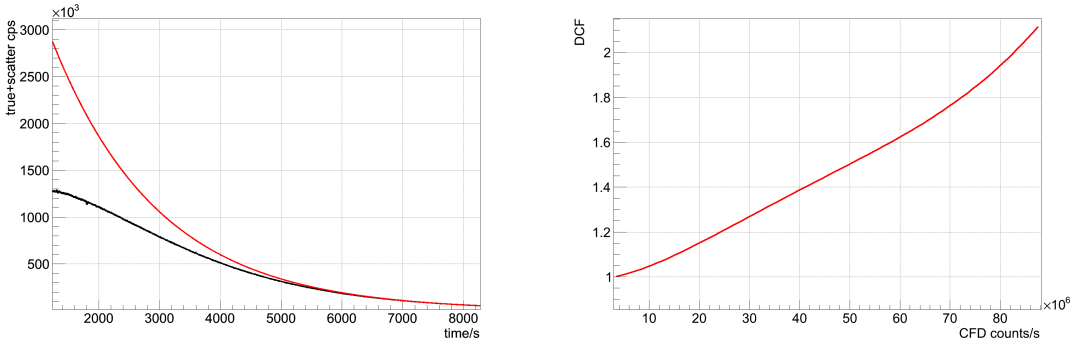

(a) Decay experiment with measured (black) and ideal (red) headcurve.

(b) Deadtime correction factor as function of CFD singles.

Figure 5.12.: From a decay experiment with measured (black) and ideal (red) headcurve the decay correction factors (DCF) can be derived.

The ratio of the two curves represents the deadtime effect for every time point of the

decay experiment. The inverse ratio can be applied as a global deadtime correction factor (gDCF). When the overall CFD countrates serves as a reliable measure for the total activity in the scanner, the gDCF can be expressed as a function of the CFD countrate. This method can now be applied to scale the reconstructed image in order to account for the global effect of deadtime. However, this approximation is only valid at countrates close to the acquisition countrates of the normalisation scan.

5.5.2. Blockbased Deadtime Correction

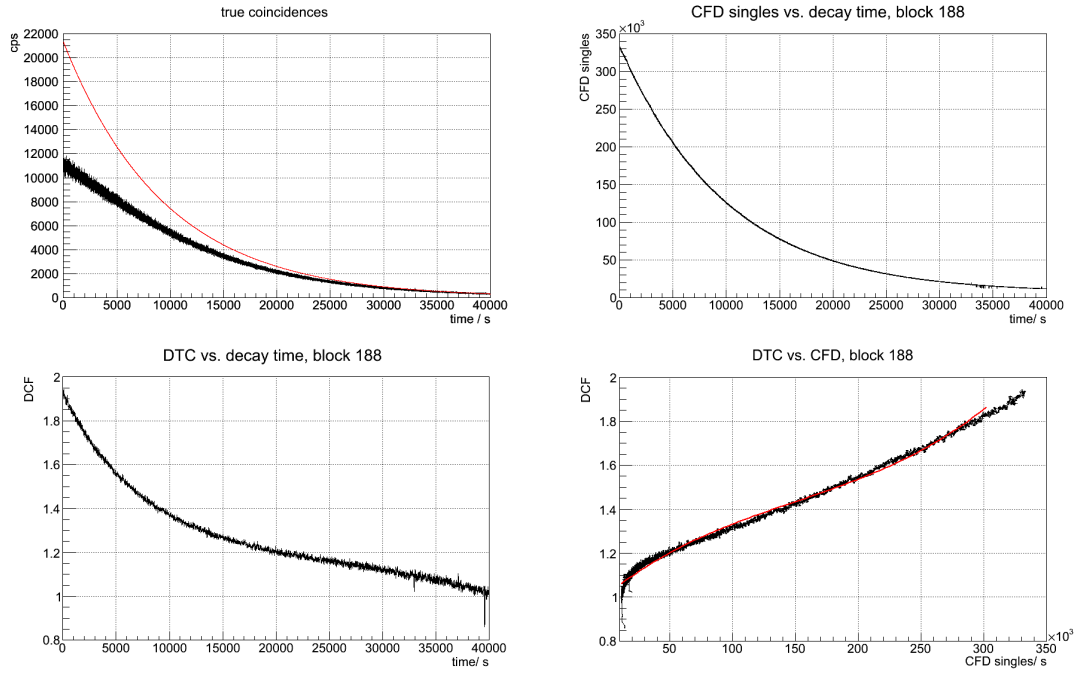

Figure 5.13.: Implementation of the block-based deadtime correction, derived from a decay experiment with a cylinder filled with ^{18}F-water (a). The final correction factor is expressed as a function of the current CFD rate of the single block (d).

When analysing the individual behaviour of different detector blocks during the decay experiment in more detail, it can be seen clearly that different blocks behave differently. The global correction factor is an average value, especially when counts of an off-centre positioned phantom are acquired (see Figure 5.14(a)). The ratio of counts is not constant during the decay experiment for all blocks. In consequence,

deadtime is now modelled for each single block, applying the method for global correction now for each single detector block (Figure 5.13). Finding a stable point of extrapolation at low countrates is more demanding. The assumed exponential decay function is fitted to the part of the measured curve at negligible deadtime to find a more robust value for extrapolation. The deadtime correction factor as a function of the CFD block counter ρ_k is fitted with a polynomial of degree 2 (or optionally degree 3, which is not implemented for the BrainPET) and the fit parameters are extracted. Knowledge of these parameters for every block allows for online computation of deadtime correction values during the framing of arbitrary phantom or human studies according to

$$d_k(\rho_k) = a_{k,0} + a_{k,1}\ \rho_k + a_{k,2}\ \rho_k^2\ \ (+a_{k,3}\ \rho_k^3) \text{ with } k = 1 \ldots 192. \tag{5.9}$$

The implementation of sensitivity correction together with the normalisation in sinogram space is described later in section 5.5.4.

5.5.3. Pileup Correction

In Figure 5.14(c) the remaining effect can be observed with a similar pattern for every detector block. A dynamic correction factor for each crystal ($N_{\text{crys}} = 27648$) cannot be extracted from crystal headcurves, since the acquired countrates per crystal are small and suffer from severe statistical fluctuations at low countrates. A robust extrapolation of these data is not achievable. Thus, the pileup pattern for each block is extracted to describe the shift of crystal efficiencies as a function of countrate. Therefore, detector hitmaps with equal number of counts (i.e. the same number of prompt events) are extracted from the listmode data. To fill maps with the same count sums at decreasing countrates, the frame lengths increase. The data points have the same statistical properties and thus the fit has the same accuracy in every data point. Subsequently, crystal counts on each block are normalised to their block average value to exclude the block deadtime effects, which are already taken into account. The resulting map shows relative crystal counts on block level. As reference for the activity within the FOV again the CFD block counters ρ_k are used. The relative sensitivity for each crystal j is fit with a linear or optionally a polynomial of higher degree and expressed as a function of the CFD countrate of its block. The inverse of the relative sensitivity changes can correct for the mispositioning of counts due to pulse pileup

$$p_j(\rho_k) = b_0 + b_1\ \rho_k\ \ (+b_2\ \rho_k^2). \tag{5.10}$$

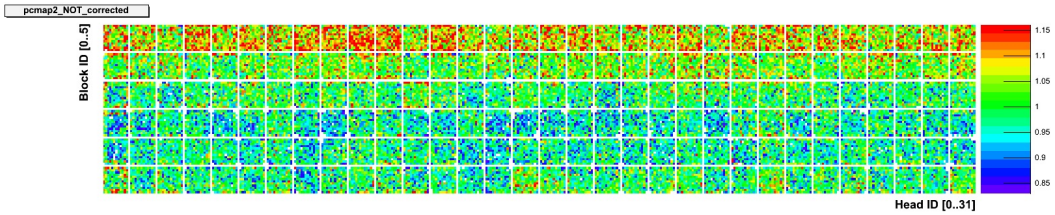

(a) Ratio of detector hitmaps applying global correction factor. The map shows the ratio of number of coincidences for each single crystal at high and low countrate.

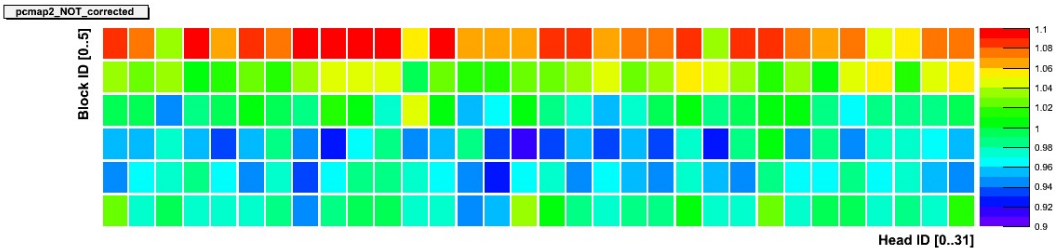

(b) Hitmap of blocks applying a global correction factor as depicted in Figure 5.14(a). For better visualisation of the block effect, the block average counts are computed.

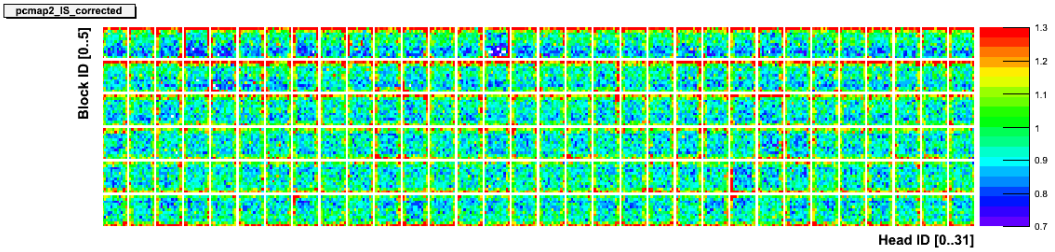

(c) Hitmap of detector after block based deadtime correction. The map is more homogeneous compared to the global correction approach. A remaining pattern similar for all blocks is visible, showing a reduced sensitivity for corner and edge crystals.

Figure 5.14.: Average block pattern with the 12×12 crystal matrix before (a) and after correction for the pileup effect (b). The inhomogeneities have been reduced, especially at the corner and edge crystals.

Again, the implementation of sensitivity correction together with the normalisation in sinogram space is described in section 5.5.4.
The correction of the effect can be seen in the hitmap of Figure 5.15 and as a block average in Figure 5.16. The improvement in homogeneity of the crystal efficiency in the maps Figure 5.14(c) and 5.15 is shown in Figure 5.17. Due to the computation of the ratio of the two hitmaps, the static normalisation factors cancel out in this representation.

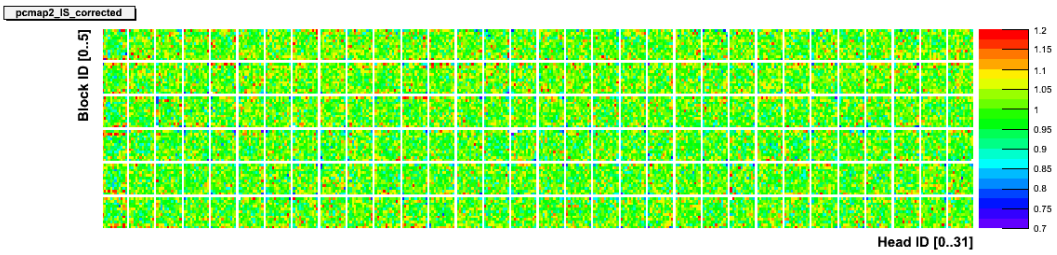

Figure 5.15.: Hitmap after blockbased deadtime and pileup correction. Both, the blockwise variations and the crystal wise shifts are significantly reduced compared to the global correction.

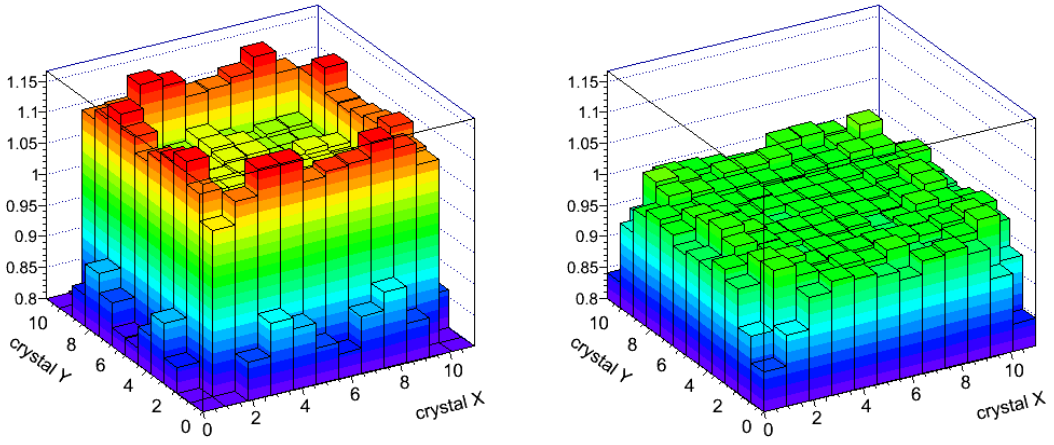

(a) Average block before pileup correction

(b) Average block after pileup correction.

Figure 5.16.: Average block pattern with the 12×12 crystal matrix before (a) and after correction for the pileup effect (b). The inhomogeneities have been reduced, especially at the corner and edge crystals.

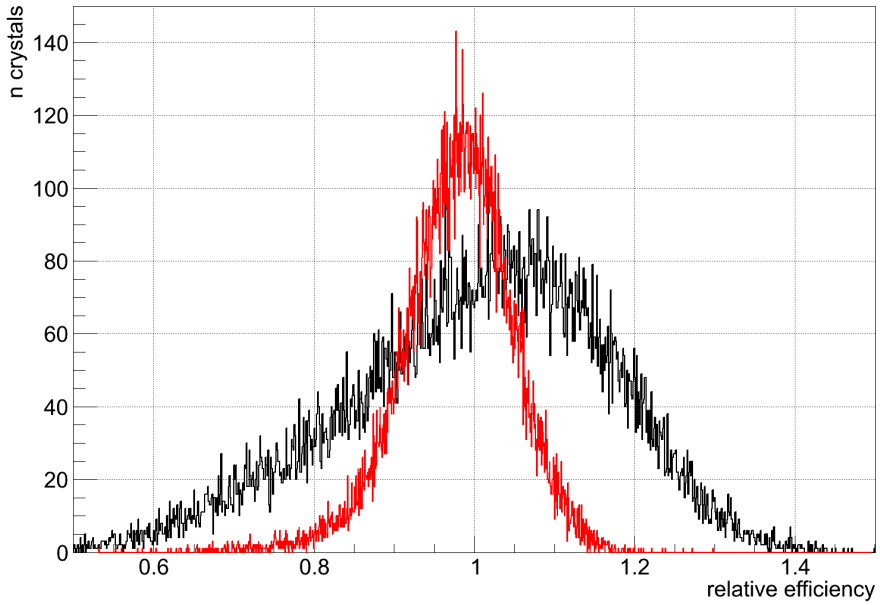

Figure 5.17.: Histogram of relative crystal efficiencies with global correction (black curve) and after blockbased deadtime and pileup correction (red curve).

5.5.4. Implementation of Sensitivity Correction

The primary goal of the combined deadtime and pileup correction is the accurate correction of the global deadtime effect. Fluctuations on block and crystal sensitivity are important to be corrected to eliminate artefacts, but must not degrade the overall quantitative accuracy. Furthermore, the sinogram correction has to be implemented carefully, since averages of sensitivities are merged into a dynamic normalisation, which is discussed in the following. The dynamic sensitivity s_{dyn} of the crystal i during the time frame from t_a to t_e contains the product of block-wise deadtime correction d_{dt} and the pileup correction d_{pu} value

$$s_{dyn,i}(t_a, t_e) = \frac{1}{t_e - t_a} \sum_{t_x=t_a}^{t_e} d_k(\rho_k(t_x)) p_i(\rho_k(t_x)). \tag{5.11}$$

Since the deadtime is not modelled as a linear effect, the average of the deadtime is not equal to the deadtime of the average CFD rate, even though, errors within one frame are small. As described, the dynamic normalisation factor ($n_{dyn}(\rho)$) as function of the block dependent CFD rate (ρ) for one LOR combining the crystals i and j reads

$$n_{dyn,ij}(\rho_k, \rho_l) = \frac{n_{i,j}}{s_{dyn,i}(\rho_k) \cdot s_{dyn,j}(\rho_l)}. \tag{5.12}$$

Here, the crystals are mounted on the block b_k and b_l with the respective deadtime and pileup effects. The static normalisation factor for the channel defined by crystals c_i and c_j is $n_{ij,stat}$ as computed by the CBN. It is important to note that the CFD countrate at which the normalisation factors are acquired has to be considered. However, this is not implemented in the current software version.
As described in Section 2.5.2, it is important to model the sensitivity effects in the normalisation in order to preserve the Poisson nature of the prompts acquisition data. Therefore, OP-OSEM treats the correction factors in the normalisation file separately from the projection data.
In sinogram space the sorting of adjacent LORs into the same sinogram bin has to be considered. This dynamic deadtime and pileup correction factors are combined with the CBN. However one sinogram bin contains the sum of the inverse of up to 12 LORs. It is not equal to the sum of the inverse sensitivity

$$\frac{1}{\sum_{i=0}^{N_{LORs}} s_i} \neq \sum_{i=0}^{N_{LORs}} \frac{1}{s_i}, \tag{5.13}$$

the combination of normalisation factors has to be performed in LOR space rather than in sinogram space in order to compute the correct normalisation factors. From this LOR-file with the countrate dependent sensitivity of each channel, the sorted normalisation sinogram is generated and has to contain the inverse dwell-pattern. The countrate dependent normalisation file is computed as follows:

i) The LOR file with the deadtime and pileup pattern is multiplied with the normalisation CBN LOR file.

ii) The conversion to a frame specific norm sinogram is achieved by cutting extreme values (upper and lower percent), converting to sinogram and scaling to a mean of 1.

iii) The scale factor is multiplied later on to the calibration factor. Since normalised CBN sinograms are assumed to be corrected for dwell, the inverse dwell pattern is inserted to the normalisation file as a double dwell-correction.

5.6. MRI-Interference Correction

Based on the results on how the MR measurement influenced the PET countrate (Section 4.4), an offline correction method was developed, implemented, and tested. It comprises a set of corrections for standard clinical MR sequences provided by the manufacturer and applied in human MR-PET studies in our institute. An overview with more detailed information on MR sequences, including those analysed here can be found in [12]. The average prompts countrate reduction in percent ΔP for standard sequences referenced here are as follows:

- localizer (short overview measurement, 2D gradient echo acquiring three orthogonal slices, TR/TE = 22ms/5ms)
  $\Delta P = -0.81 \pm 0.02$.

- MP-RAGE (T1-weighted anatomical sequence, gradient echo based,
  TR/TE = 2000ms/1.29ms)
  $\Delta P = -0.77 \pm 0.017$.

- UTE (ultra short echo time, T2* weighted image for bone detection,
  3D dual-echo radial centre out projection acquisition,
  TR/TE1/TE2 = 200ms/0.07ms/2.46ms)
  $\Delta P = -1.48 \pm 0.13$.

- EPI (echo planar imaging, applied in fMRI, TR/TE = 1450ms/49ms)
  $\Delta P = -1.03 \pm 0.081$.
- FLAIR (T2 weighted anatomical measurement, 2D spin-echo based
  TR/TE = 9490ms/109ms)
  $\Delta P = -0.32 \pm 0.025$.
- DTI-1 (diffusion tensor imaging; EPI readout with additional (strong)
  diffusion weighting gradients TR/TE = 7900ms/99ms,
  diffusion b-value= 1000s/mm^2)
  $\Delta P = -1.17 \pm 0.092$.
- DTI-2 (see DTI-1, reference scan without diffusion weighting)
  $\Delta P = -0.98 \pm 0.043$.

Based on the evaluation of the influences and the high reproducibility of the effects, a correction method was designed, implemented and evaluated. The method provides a time-dependent, global correction factor for each MR sequence which is stored as a lookup-table (LUT). This LUT is obtained from a phantom study with an [^{18}F]-water filled cylinder (Figure 5.19). The countrate during the MR sequence is approximated by a polynomial or a sine function, depending on the MR sequence. The expected countrate is estimated by extrapolating the adjacent PET countrates without MR acquisition to the time during MR acquisition. Finally, the ratio of expected and measured countrate gives the time dependent correction factor (Figure 5.19). This procedure is performed with the set of clinical MR sequences applied in human studies. The temporal synchronisation of MR sequences and the PET listmode data is achieved by using the MR trigger signal, as applied, for example, in combined EEG and fMRI studies. This signal is sent for each TR with a precision of 10 μs and is passed to the listmode. Thus, a sufficient temporal accuracy of synchronisation is assured. It is possible to correct the listmode data by applying the factors stored in the LUT before sorting. However, in order to preserve the Poisson characteristics of the emission data and to minimise the noise in the reconstructed image, the correction factor is included in the normalisation, similar to detector deadtime [63] for the standard procedure. Performance of the correction method is shown for the two standard sequences, MP-RAGE and UTE, which were applied during the PET data acquisition of a cylinder phantom with 14 cm diameter and filled with ^{18}F diluted in water (see Figure 5.18). The same countrate for true coincidences is shown in Figure 5.20 but now corrected for the

MR influences. In both plots the global slope is due to the decreasing radioactivity of ^{18}F (half life of 109 min).

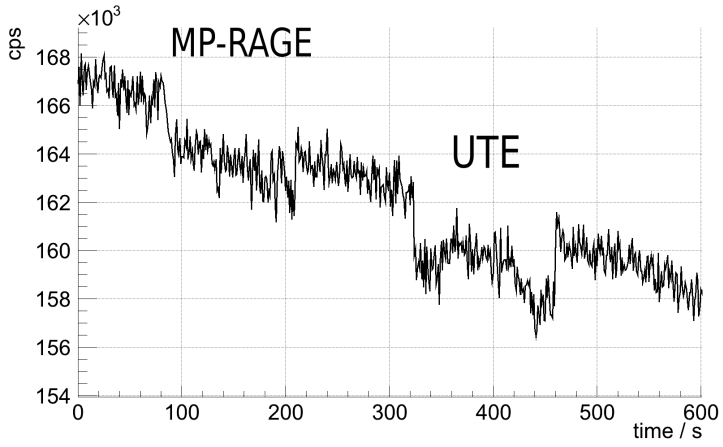

Figure 5.18.: Uncorrected PET headcurve of the ^{18}F-cylinder measurement with simultaneously acquired MP-RAGE (left) and UTE (right) sequences.

5.7. Decay Correction

The labelled molecules injected within the subject's body have a constant number. However, the number of radioactive nuclei, and with them the traceable molecules, are reduced due to the radioactive decay. Therefore, the number of detected molecules to be traced at a specific time of the scan has to be re-weighted, in order to represent the same distribution as if it would have been scanned at an early time of the measurement. This correction is referred to as decay correction. The physical decay is described by an exponential law with a nuclide specific half-life. It follows Equation 2.3 and for correction the inverse exponential function has to be applied.
For frames with the duration Δt with the acquisition start time t_a after start of measurement, the decay correction factor α reads

$$\alpha = \frac{\lambda\, e^{\lambda t_a}\, \Delta t}{1 - e^{-(\lambda\, \Delta t)}}, \tag{5.14}$$

as derived in the Appendix A.

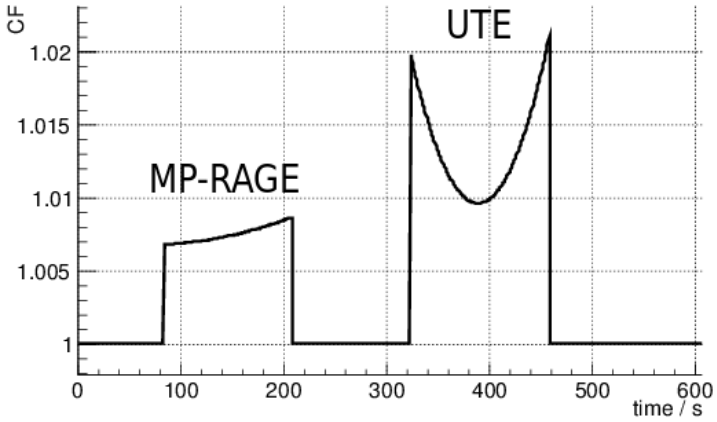

Figure 5.19.: MR correction values for MP-RAGE (left, 80 s – 210 s) and UTE (right, 320 s – 460 s) sequence.

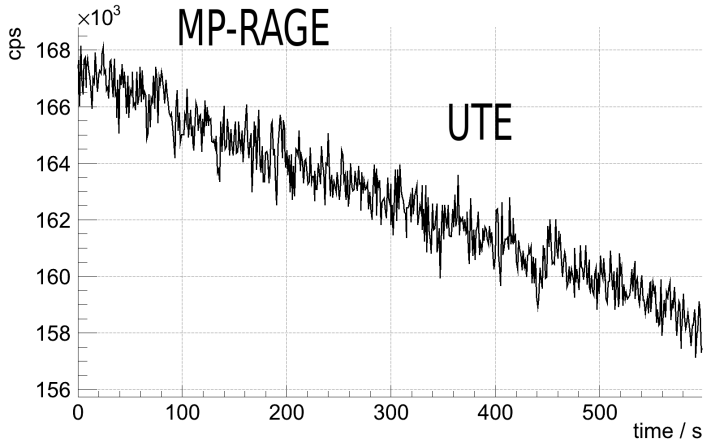

Figure 5.20.: Corrected PET headcurve of the ^{18}F-cylinder measurement with simultaneously acquired MP-RAGE (left) and UTE (right) sequences. The applied correction values are the ones depicted in Figure 5.19.

5.8. Image Reconstruction

Applying the OP-OSEM reconstruction algorithm, the number of iterations and subsets has to be defined. It is known from the literature, that convergence of the OSEM algorithm in the presence of noise is not guaranteed. Reconstructing images with a higher number of subsets is prone to image artefacts, since the solution of the algorithm starts oscillating from iteration to iteration in the presence of systematic uncertainties of the corrections. For a reasonable number of subsets, this effect is rather small, as shown for a cylinder study in Figure 5.21(a) and (b) comparing 1 and 8 subsets. The difference image in Figure 5.21(c) shows minor structural differences. However, in the extreme case of 32 subsets which corresponds to the number of detector cassettes severe image artefacts become visible Figure 5.21(d). Since the data are corrected and reconstructed offline, the extend

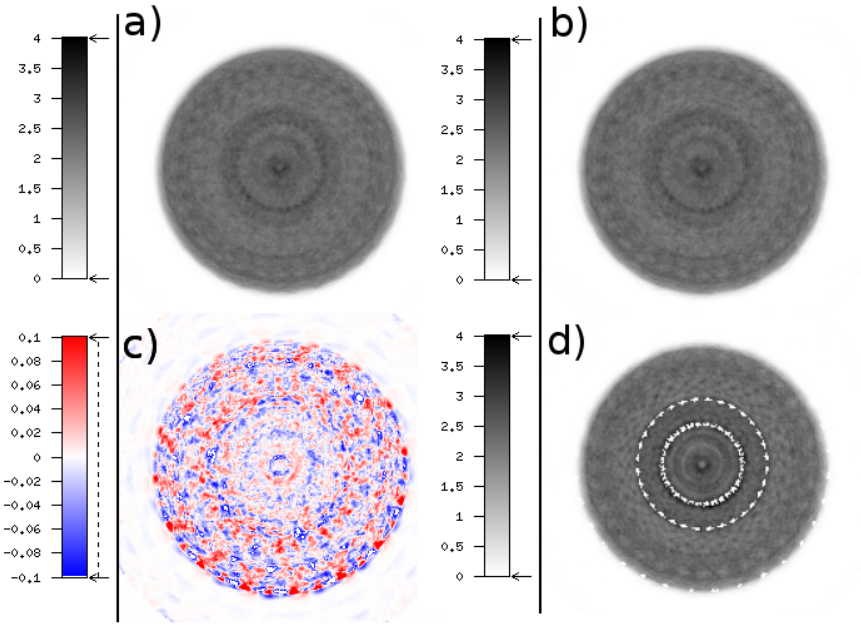

Figure 5.21.: Effect of increasing number of OSEM subsets. The total number of ML-EM iterations is always 128. Image (a) is reconstructed with 1 subset, 128 iterations, image (b) with 8 subsets, 16 iterations. Figure (c) shows the difference image of (a) and (b) indicating minor systematic structures. Image (d) was reconstructed with 32 subsets and 2 iterations. The artefacts are clearly visible.

on reconstruction time for the lower number of subsets is not a critical restriction when image artefacts can be reduced with this approach. Thus, it is recommended to apply not more than 4 subsets. The default value for standard reconstruction is set to 2 subsets. The number of overall ML-EM iterations is crucial in combination with the correction terms such as scatter and random correction and, furthermore, depends on the object itself. This is evaluated in detail in the Chapter 6.

5.9. Image Calibration

Calibration is the procedure of translating the image intensity value with the arbitrary unit of pseudo count per second (cps) into an activity concentration within the subject (Bq/ml or kBq/ml). The calibration is vital to quantify the metabolism within one subject, but also to compare subjects within a longitudinal study or to compare different studies acquired with different scanners.
Therefore, a measurement with an ^{18}F filled cylinder of known activity concentration (verified with a calibrated wellcounter and dose calibrator) is measured and reconstructed with the standard procedure applying all corrections. The image intensity values in a defined ROI are compared to the measured activity concentration with the wellcounter. The values for a series of 9 subsequent calibration measurements acquired over 9 weeks are depicted in Figure 5.22. The verification of the stability of a previously determined calibration factor is one component of quality control and the long term stability of the scanner.
In the example of Figure 5.22 the calibration factor is verified with the above mentioned procedure. The calibration factor is determined to be 0.9901 ± 0.0101 of the nominal value of 72,000 kBq/ml/cps. As consequence, the calibration factor should be adapted from 72,000 kBq/ml/cps to 71,287 kBq/ml/cps even though the error is still in a tolerable range for clinical application.

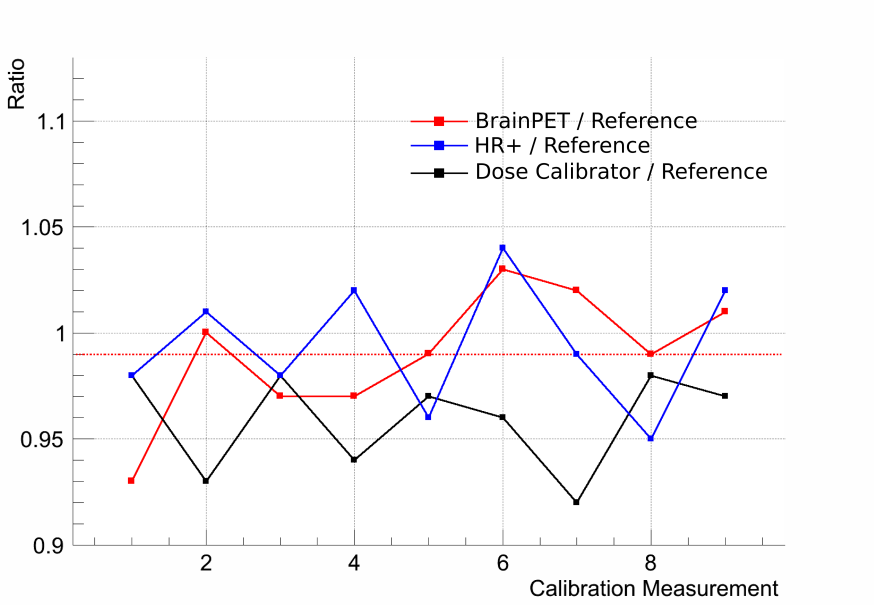

Figure 5.22.: Verification of calibration factor in 9 subsequent measurements acquired over 9 weeks (solid red curve). The uncertainties in comparing activity concentrations is shown by the ratio of wellcounter and dose calibrator values of the same probe (solid black curve). The deviation from the current calibration factor is fitted with χ-square method to the measured data (dashed red line). The blue line shows the verification of the calibration of the HR+ scanner with the same phantom measurements, providing a cross calibration of the scanners.

5.10. Image Reconstruction Framework

To provide a stable clinical environment for human studies, the components for framing, precorrection, image reconstruction and finally calibration have been integrated in a workflow. In the design of the workflow the following aspects have to be optimised:

- Minimal Data Processing and Image Reconstruction Times
- Minimal Computational Burden (Standard Desktop Computer)
- Minimal Disk Space Usage
- Minimal User Interaction
- Optimal Quality Control

After data acquisition and transfer of PET listmode data and MR images to the central data storeage, the listmode data are framed according to the study protocol. Here, the relevant information for each frame is extracted, namely the start time and framelength for decay correction (Equation 5.14) and the CFD countrate for the individual block for deadtime and pileup correction. Furthermore, an LOR file for prompt coincidences and a hitmap for delayed singles (DCMAP) is generated. From the DCMAP, the VRR LOR-file and sinogram are generated. Optionally, a first image is reconstructed (image_n), reconstructing prompts corrected for randoms and normalisation only (OP-OSEM, 4 subsets, 16 iterations). This image can be used for the verification of co-registration of the attenuation map and can serve as a very first quality control. The correction factors of the blockbased deadtime correction and the pileup correction are expressed as a function of CFD countrate and a combined correction is computed for each individual LOR. Since the LORs are histogrammed for the sinogram based reconstruction [41].
The attenuation properties for the subject and the MR RF coil are merged in image space and projection space. Therefore, the mumap from patient's head and of the MR coil are merged and forward projected into sinogram or LOR space for sinogram or LOR reconstruction, respectively. Due to the multiplicative character of normalisation and attenuation, the forward projection of the coil map can also be included in the normalisation sinogram.
With this correction, an image which is corrected for random and attenuation is reconstructed (image_na). After cutting the 200 highest values, which are noise

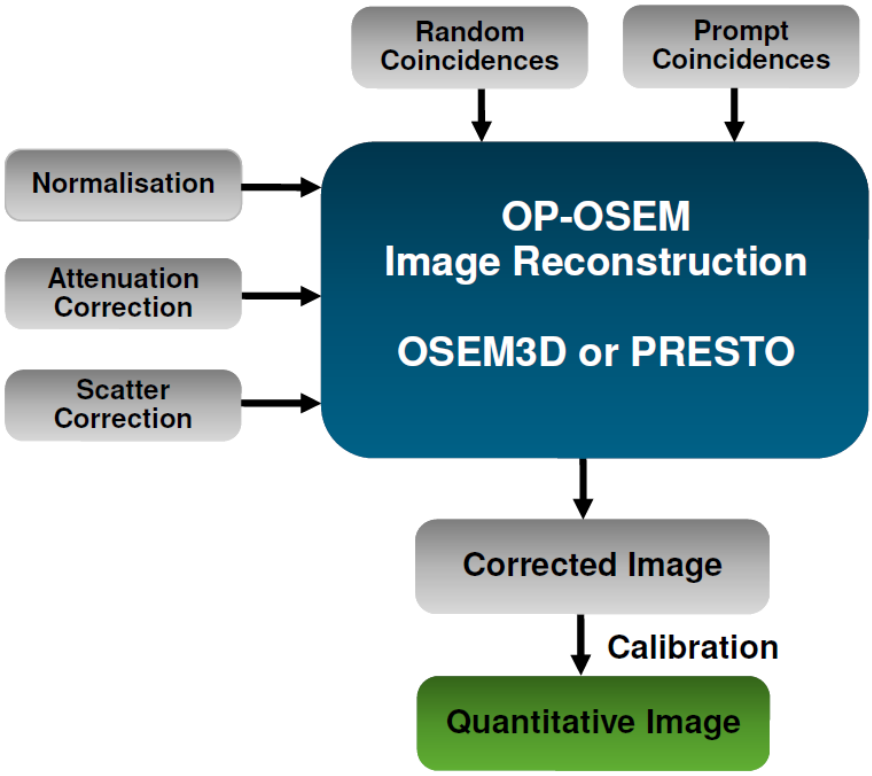

Figure 5.23.: Workflow of the final image reconstruction process. In the presented visualisation, the calibration includes the calibration factor and the correction for global deadtime and decay.

voxels in the most upper and most lower image plane, this image serves as an estimate of the activity distribution for the scatter simulation. The cutting of high values is important for the scatter estimation software.
The subsequent step of scatter simulation [102, 103] results in a scatter sinogram, which is now included in the last image reconstruction step, resulting in a fully corrected image [62]. Here, the OP-OSEM approach is applied, with 2 subsets and 32 iterations, equivalent to 64 ML-EM iterations (see Figure 5.23). After cutting image planes 0 and 152, the global correction factors for radioactive decay of the isotope (Equation 5.14), the global deadtime correction, the normalisation of the framelength and the image calibration factor are applied. These ($\text{image}_{\text{nas}}$) are calibrated in order to represent images in the quantities of Bq/ml. However, for a more reliable estimation of scatter, this estimation has to be performed iteratively 3 times (see Section 5.3). For convenience in file and data handling, the image volumes are converted into the ECAT7 format which is a standard in nuclear medicine besides the upcoming DICOM format. The ECAT image includes valuable header information about the patient, the study and intermediate correction steps during image reconstruction and is capable of storing multiple frame data. With this workflow, a modular and convenient image reconstruction procedure has been implemented, which furthermore allows for quality control on different levels.

6. Evaluation of Quantification for PET Images

Parts of this chapter have been published in [104].

The quantitative accuracy is assessed with phantom and *in vivo* studies. Only the selection of the performed experiments is given here that covers the aspects of corrections comprehensively. It describes the entire reconstruction framework in addition to the verification of its components, given in Chapter 5. The applicaton of phantoms offer the advantage of a defined geometry and the activity distribution is easy to control. Image artefacts and shortcomings of the quantification accuracy are observed with variation of versatile parameters, such as countrate or geometry. Reference probes of the activity concentration are measured for all experiments with a calibrated gamma counter (Wallac Wizard 1480). The results of the phantom studies are discussed in Section 6.1. These results are used to optimise the reconstruction procedure for human studies.
The quantification of human studies is discussed in Section 6.2 applying the entire reconstruction framework. The verification of *in vivo* PET imaging is demanding. In contrast to phantom studies, it is not feasible to obtain the ground truth of the tracer distribution. Thus, combined studies with the Siemens 3T MR-BrainPET and the Siemens HR+ scanners were conducted in order to cross validate the images. Together with the experience gained with extensive phantom studies the results can be validated more accurately.

6.1. Evaluation with Phantom Studies

6.1.1. Dynamic Range

A PET scanner has to be capable of quantitative imaging at high dynamic of countrates. This becomes important when applying tracers with short physical half life compared to the scan time, as for ^{15}O or ^{11}C administered per bolus injection.

These scans usually exhibit a very high dynamic, as observed in perfusion measurements with ^{15}O-labelled water. Depending on the radiotracer and on the study design, the countrate can also be constantly high or constantly low, as observed in ^{18}F-FDG or ^{18}F-FET steady-state scans, respectively. The static and dynamic effects have to be corrected with the presented procedures prior to reconstruction and calibration.

^{18}F Decay Experiment

A decay experiment is designed to assess the quantification accuracy of the dynamic range observed in human measurements. In contrast to the experiments perfomed to derive the parameters for decay correction, the one pesented here apply the entire reconstruction framework with all its corrections. The study accounts besides the deadtime effect also for the reduced activity at later frames, which is already presented in Section 5.3. Consequently, this study provides an independent cross check of the optimised deadtime correction. A cylinder phantom of 14 cm diameter and 20 cm length is filled homogeneously with ^{18}F diluted water. The total activity filled in the phantom was approximately 74 MBq. All determined activity concentrations were corrected for radioactive decay to the start of the PET data acquisition. The exact activity concentration at the start of the PET measurement was determined with 3 weighted probes (500 mg) in a calibrated well-counter and was found to be 18.01 kBq/ml $\pm$ 0.62 %. The cylinder phantom was positioned within the PET FOV axially and transaxially centred within the RF head coil. PET data of the decaying isotope were acquired over 6 half lifes of ^{18}F (dynamic range: $2^6 = 64$) in listmode. The framing and reconstruction were done using the standard reconstruction procedure. The reconstructed images (see Figure 6.1 and Table 6.1) have been evaluated by ROIs of 12 cm diameter and 70 image slices, corresponding to 87.5 mm for each frame.

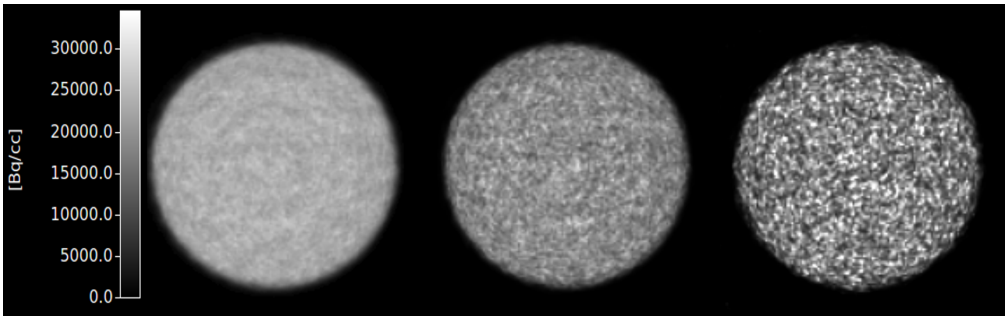

Figure 6.1.: Transaxial view of reconstructed images of the decay experiment. Left image after 1 h, middle image after 5 h, right image after 10 h of the PET acquisition start time. The duration of each frame was 1 h.

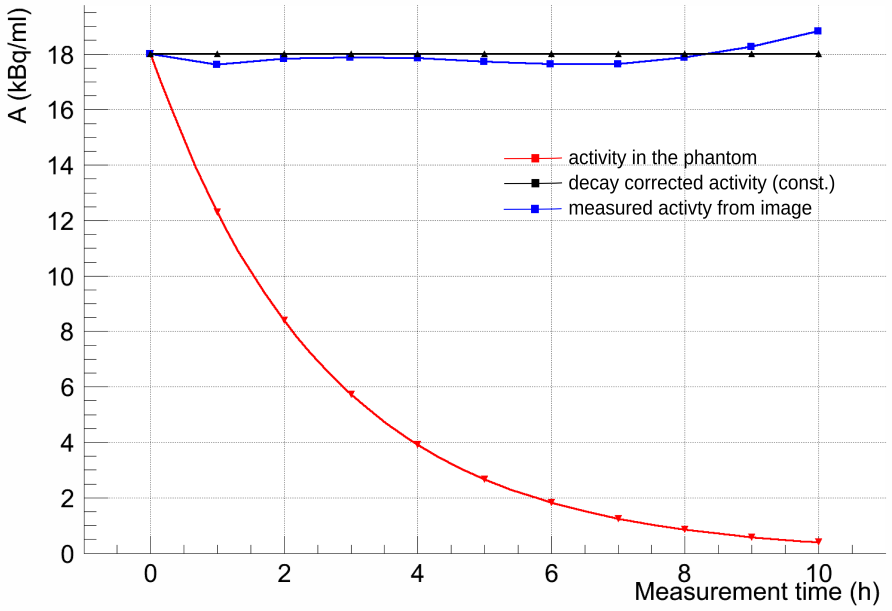

Figure 6.2.: Time-Activity-Curve (TAC) of the decay experiment applying a cylindrical phantom. The red curve shows the actual activity concentration in the phantom, the black curve represents the decay corrected value of the probe (constant) which is also the expected mean value in the ROI of the reconstructed image. The actual mean value in the ROIs is represented by the blue curve.

Frame	expected (kBq/ml)	measured (kBq/ml)	error from expected value (%)
1	18.01	17.99	- 0.1
2	18.01	17.61	- 2.2
3	18.01	17.82	- 1.1
4	18.01	17.87	- 0.8
5	18.01	17.83	- 1.0
6	18.01	17.62	- 2.1
7	18.01	17.63	- 2.3
8	18.01	17.86	- 0.8
9	18.01	18.24	+ 1.3
10	18.01	18.80	+ 4.4

Table 6.1.: Decay experiment with a homogeneously filled cylinder (^{18}F-labelled water). All values are corrected for the radioactive decay of the isotope to the start of the PET scan.

The error in mean value between well-counter and reconstructed image ranged from -2.2 % for an early frame to +4.4 % for a late frame as visualised in Figure 6.2. The standard deviation of the distributed values (given as CoV) ranged from 7.9% for the highest count sum up to 35.2% for the lowest count sum. The tendency of increased mean values in the last four frames with low overall count sum has also been observed in other experiments. It is consistent with the findings in Section 5.3 and issue of further investigation.

^{18}F-^{11}C Decay Experiment

The accuracy of quantification in reconstructed images was further investigated with a combined ^{18}F-^{11}C phantom study. The phantom consisted of two concentrically arranged cylinders with different diameters. The inner cylinder was filled with an activity concentration of 84.54 kBq/ml of ^{11}C diluted water, whereas the outer cylinder was filled with 7.31 kBq/ml of ^{18}F diluted water at the start of the PET measurement. A measurement with an acquisition time corresponding to 5 half-lifes of ^{11}C was performed. After acquisition, 10 frames of 10 min length each (1/2 half life of ^{11}C) were reconstructed and the ROIs according to Figure 6.3 were evaluated.

(a) Picture of a cylinder phantom transaxially centred within the MR head coil.

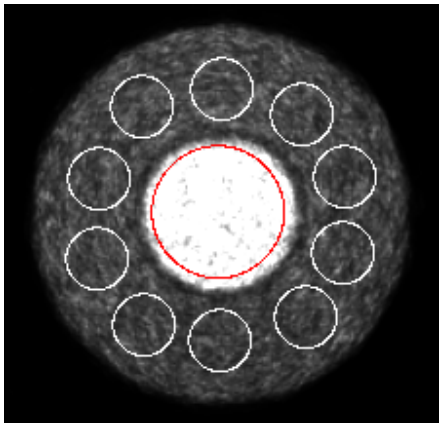

(b) Reconstructed image of the ^{18}F-^{11}C decay experiment including the ROIs.

Figure 6.3.: Setup of the decay experiment (a) applying the two isotopes ^{11}C and ^{18}F in the cylinder phantom with two compartments (b).

This phantom study is especially challenging for the scatter correction with respect to the varying ratios of activity concentration within the compartments. The decay correction for each compartment together with the calibration was applied after reconstruction. The expected decay curves of ^{11}C and ^{18}F were obtained from the reconstructed images. The residual error ranged from -2.4 % to 4.7 % in the ^{11}C-region and up to 2.6 % in the ^{18}F-region. The quantitative values obtained from the ROIs of the ^{18}F-region and the ^{11}C-region for each frame are depicted in Figure 6.4 (a) and (b), respectively.

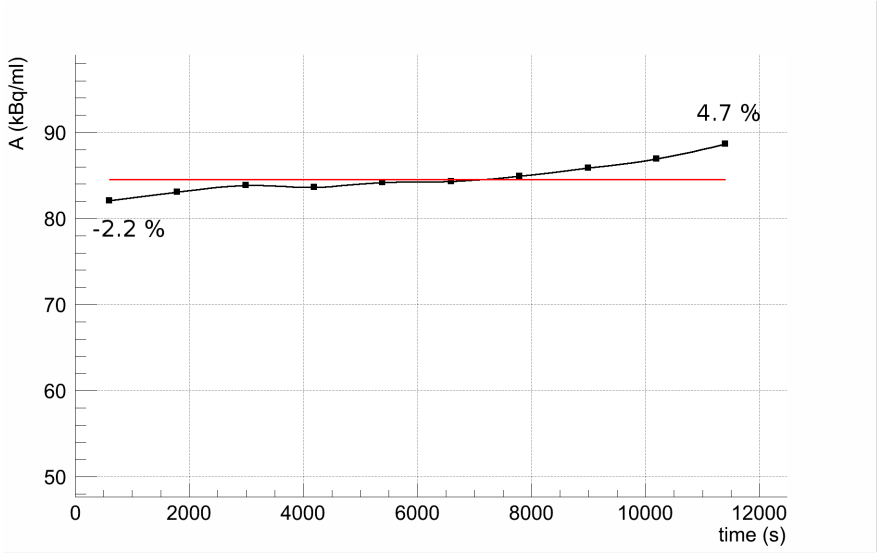

(a) ^{11}C compartment

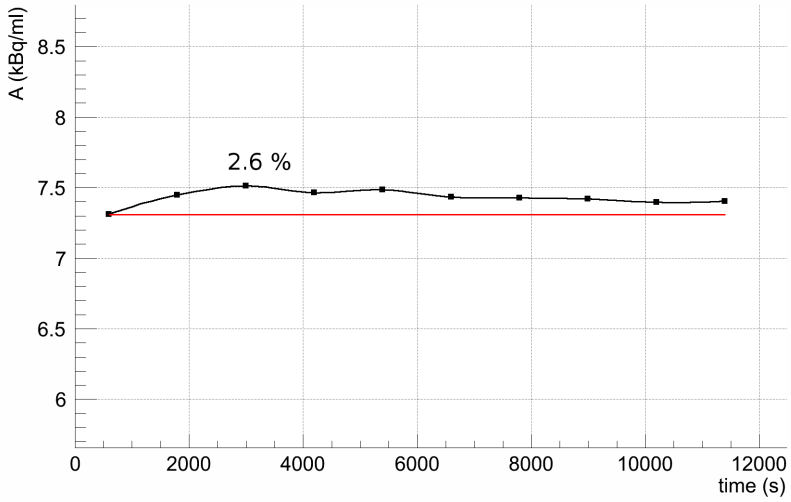

(b) ^{18}F compartment

Figure 6.4.: Time activity curves of the the two isotopes ^{11}C (a) and ^{18}F (b) in the cylinder phantom with two compartments after appropriate decay correction.

6.1.2. Contrast and Convergence

A phantom study to analyse the image contrast and the quality of the correction was performed with the two-chamber phantom (see Figure 6.5(a)). It mimics the

(a) Picture of the two chamber phantom.

(b) Two chamber phantom reconstructed with 200 ML-EM iterations.

Figure 6.5.: Study applying the two-chamber phantom to assess the contrast and convergence properties of the reconstruction process.

transaxial view of the human brain segmented into grey matter (GM) and white matter (WM). The aim of this study is to assess the contrast recovery in the reconstructed image depending on the data corrections. Especially the convergence of the image reconstruction depends on the contributing additive errors, such as scatter and random fractions (see Section 2.5.2). In [^{18}F]-desoxyglucose brain studies of healthy volunteers, a GM/WM ratio of approximately 4:1 should be observed. Thus, the two chambers were filled with 83.5 kBq/ml $\pm$0.48 % in the GM compartment and with 20.1 kBq/ml $\pm$ 1.06 % in the WM compartment, determined by 3 probes for each compartment, measured with the well-counter. This results in a GM/WM ratio of 4.15:1 for the presented experiment. In human FDG brain studies, a total activity of approximately 350 MBq of FDG is injected, resulting in activity concentrations of approximately 40 kBq/ml in the GM and approximately 10 kBq/ml in the WM compartment, which is about half the concentration as in

the presented phantom study. Consequently, a higher random rate is expected here, which results in a later convergence of the OP-OSEM algorithm compared to an FDG scan.
The images are reconstructed with the standard procedure. The contrast is described as a function of ML-EM iterations and of the iterations of scatter corrections. The evaluated GM/WM ratio in the reconstructed images are depicted in Figure 6.6. Consistent with the findings in Chapter 5, the best performance is found when applying 3 iterations of the scatter correction. A default value of 200 ML-EM iterations (equivalent to 2 subsets with 100 iterations or 4 subsets with 50 iterations) is recommended to obtain converged images.

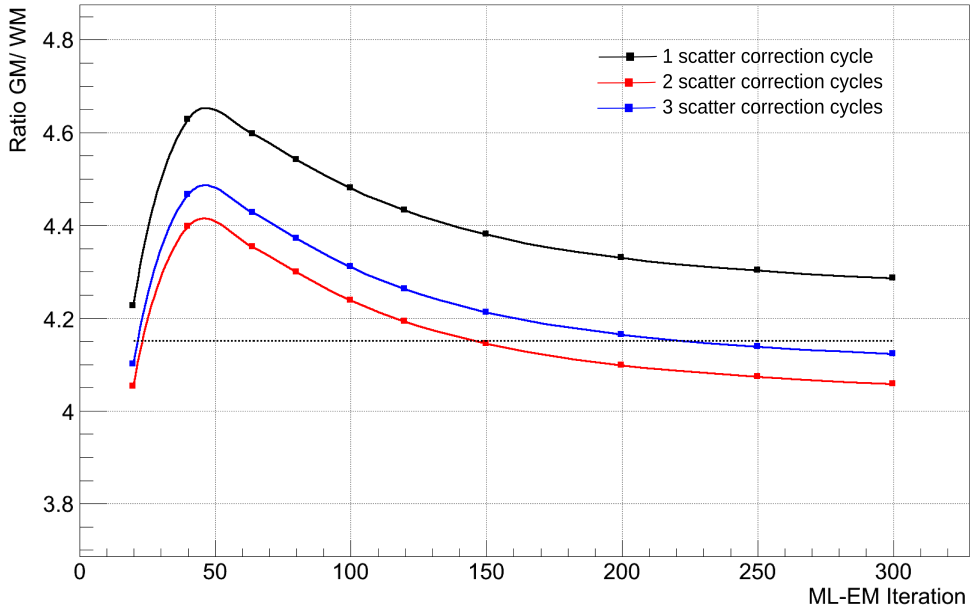

Figure 6.6.: Contrast of GM/WM in the reconstructed image applying 1, 2 and 3 iterations of the scatter correction (red, black and blue curve, respectively). The two-chamber phantom with the determined ratio of 4.15:1 between GM and WM compartment (dashed line) is approached best at 200 ML-EM iterations applying 3 iterations of the scatter correction (blue curve).

6.1.3. Long Term Stability

Monitoring the stability is important for a PET scanner, since the results of studies have to be comparable over a long period of time. This includes the detection of immediate detector element failures, as well as slow drifts in crystal and block efficiencies. Also the verification of the currently used normalisation and calibration factor is an issue of quality control. A set of regularly performed measurements is defined in the dailyQC in order to assess the current status of the scanner [105]. diameter and length, positioned axially and transaxially centred within the PET FOV. The RF head coils were not located within the scanner. The phantom was measured for 10 minutes on each working day. The measurement is corrected for decay of the radioisotope and deadtime. Prompt and delayed coincidences were evaluated to examine the temporal behaviour of each crystal. Deviations from a reference taken at the day of the last normalisation scan are documented.
Looking at the mean count values of the crystals acquired in each dailyQC measurement (see Figure 6.7), only minor fluctuations were observed. The variation in the individual crystal counts, which are due to the unequal crystal sensitivity, are given as the standard deviation for each measurement. Also, these values are sufficiently constant. From an experiment with longer acquisition time, the sensitivity has been extracted and is depicted in Figure 6.8. The sensitivity of corner and edge crystals (red curve) has been compared to the one of more central crystals on a block (black curve). As expected, the corner and edge crystal exhibit a reduced sensitivity compared to the central crystals.
The evaluation of the temporal behaviour of crystal efficiencies during 34 weeks is crucial in regards to validity of the normalisation. Here, the majority of the crystals were found to be stable (see Figure 6.9). Looking at single blocks, an increase in standard deviation was found to be more severe for corner and edge crystals, characterised by red marked crystals on the map. However, these fluctuations were measured during 34 weeks. They are much smaller for periods of 4 weeks and are accounted for by a monthly normalisation scan. Secondly, the data presented are acquired with a suboptimal setup, described in Section 4.2.3, to indicate the higher fluctuations of corner and edge crystals. With the findings presented here, it is stated that the BrainPET scanner is sufficiently stable for clinical studies.

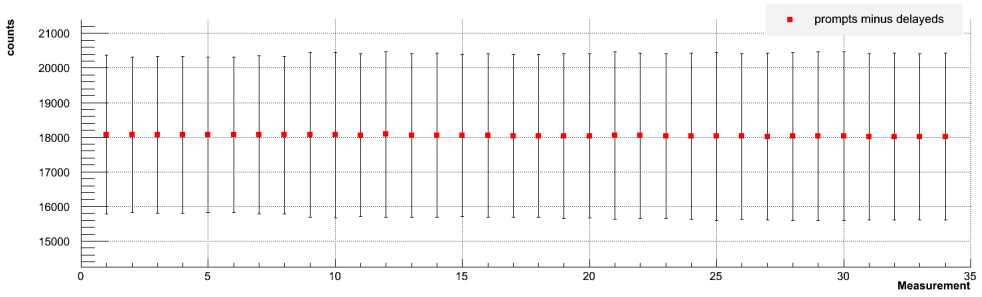

Figure 6.7.: Evaluation of the mean count sum (true + scattered events) detected by the crystal during the dailyQC scans and the standard deviation of these values, due to the non-uniform crystal efficiencies. The data were acquired over 34 weeks.

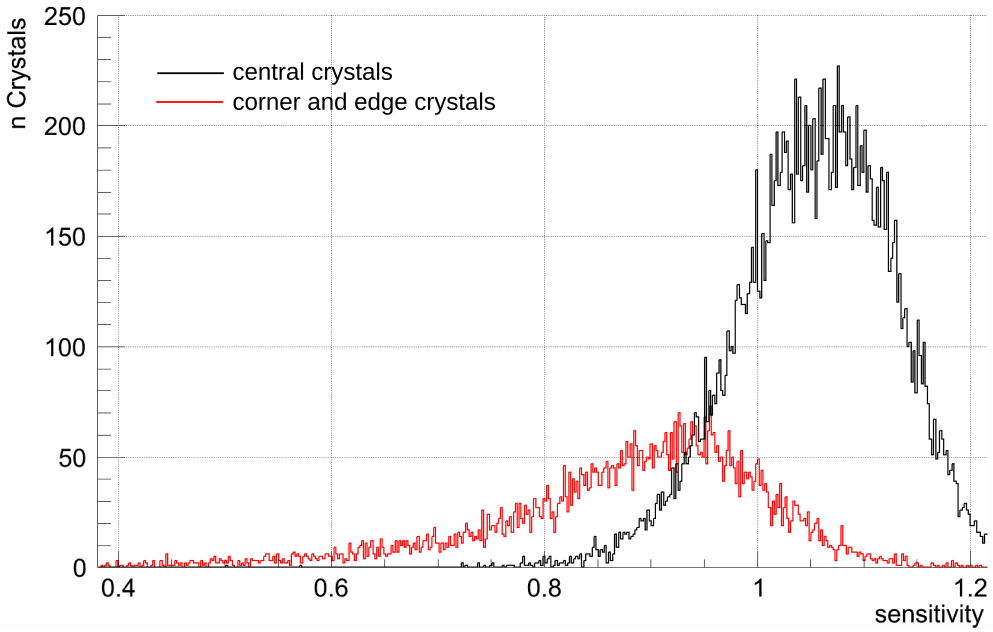

Figure 6.8.: Distribution of sensitivity of corner and edge crystals (red curve) compared to centred crystals of the detector blocks (black curve).

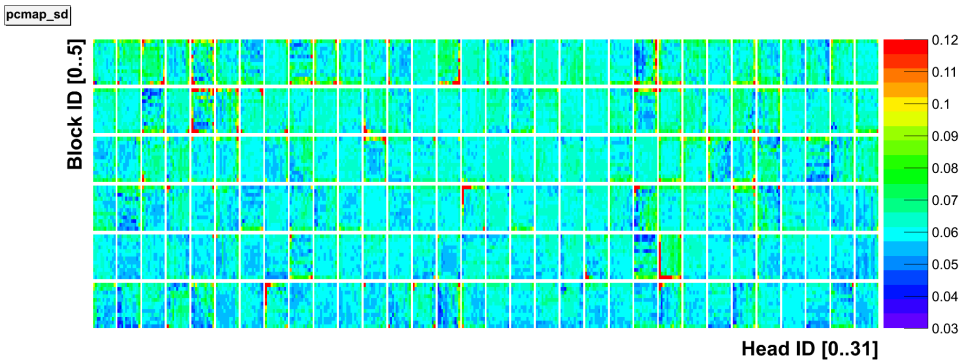

Figure 6.9.: Temporal variations of crystal sensitivities evaluating dailyQC measurements before the latest setup optimisation. Corner and edge crystals show higher variances than central crystals. The data is given as color encoded standard deviation from the mean value, assuming a Gaussian distribution of sensitivities. Again, the data were acquired over a period of 34 weeks.

6.2. Human MR-PET Studies

With the results obtained from the detailed phantom studies together with the long term stability it can be concluded that the PET scans in simultaneous human MR-PET studies provide excellent image quality and accurate quantification. A large variety of PET tracers has been measured together with simultaneous MRI using the 3T MR-BrainPET. Four human scans applying different tracers are discussed in the following. Depending on the application, radiotracer and radioisotope different aspects of corrections become prominent. The improvements observed by the evaluation of phantom studies also improve the accuracy of human MR-PET studies and are indicated for the presented applications. The medical or biological interpretation of the studies is beyond the focus of this work.

6.2.1. [^{18}F]-FET-PET/MRI Studies

The ^{18}F-labelled amino acid O-2-[^{18}F]-Fluroethyl-L-tyrosine (FET) is a PET tracer often applied for brain tumour studies. With a high uptake in cerebral gliomas and low uptake in inflamatory cells and the cortex (see Figure 6.10), the tracer is more specific than the widely used FDG [54]. Besides the spatial distribution, the time response of the tracer is important since it allows, for example, the distinction between local brain metastasis recurrence and radionecrosis with high accuracy [29].

From a technical perspective, two cases have been observed when evaluating the performance of the correction procedures for FET-PET scans with the BrainPET. Scans with high FET uptake in the brain show mostly an uncompromised image quality. However, in some cases with low uptake, which coincides with minimal uptake in the assumed tumor region, artefacts have been observed. It was found that shortcomings in the scatter estimation can lead to severe tracer underestimation in some cases. This has been observed at scans performed with the suboptimal detector setup and when only one scatter iteration has been performed [72]. A sub-optimal setup which cannot be compensated completely with a current normalisation scan, and the overestimation of scatter by applying only one scatter iteration, this can lead to major image artefacts. In order to retrieve the data set, the data has been recoverd partly by using 3 scatter iterations (see Figure 6.11). In order to prevent further scans from this kind of shortcoming, the setup has been optimised, as shown in Chapter 4.2.3. In addition, the 3 iteration cycles of scatter correction is highly recommended also in the case of FET-PET scans.

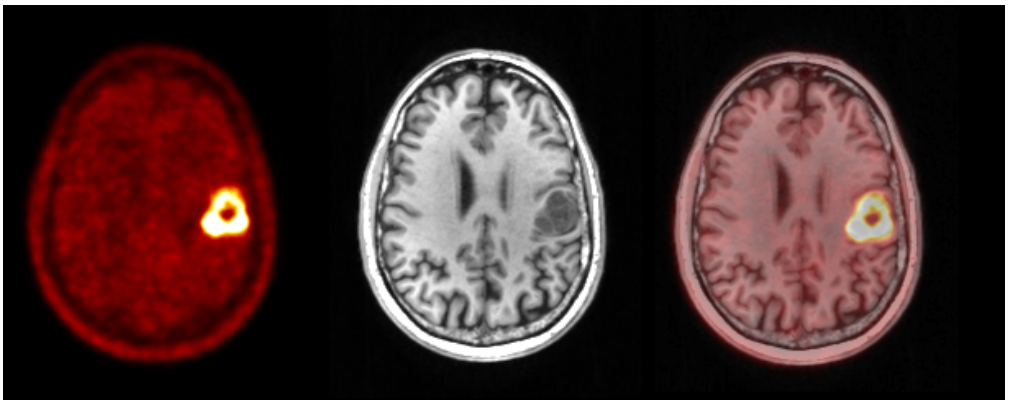

Figure 6.10.: The [^{18}F]-FET-PET image (left) of a human brain showing the uptake of the ^{18}F-labelled amino acid in the brain tumor and low uptake in the cortex. The middle image shows the anatomical T1 weighted MP-RAGE image. The right image shows the fused PET and MRI scans. The MR image provides the complementary anatomical information to the metabolic activity in the PET image.

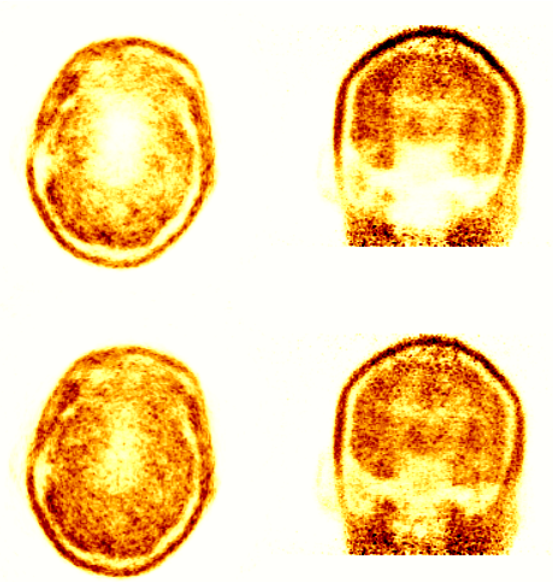

Figure 6.11.: FET patient study. When no enhanced uptake was observed in assumed tumor tissue, the overestimation of the scatter becomes obvious. This results in a profound underestimation of the activity (upper row). After 3 iteration cycles of scatter correction, this effect has been reduced (lower row).

In order to assess the quantitative determination of the time response of the tracer a study is presented, where a patient with glioma has volunteered to be scanned in the MR-BrainPET before his diagnostic scan in the Siemens HR+ scanner. The patient was injected 224 MBq of FET in the MR-BrainPET and the data were acquired from the moment of injection for 55 min. The listmode data were subdivided into 16 frames. After the scan the patient moved to the Siemens HR+ scanner, where further 4 × 5 min of PET data were acquired for diagnostic. The time-activity-curves (TAC) of both scans have been compared. Here, the regions of tumor, cortex and whole brain were evaluated for both scans. The HR+ images were decay corrected to the start of the BrainPET scan. It shows that the HR+ images are in good agreement with the BrainPET images (Figures 6.12 and 6.13) in terms of absolute quantification. The stronger fluctuations in the tumour regions are related to the statistical uncertainties in the much smaller ROI and also due to possible misalignment caused by patient movement.

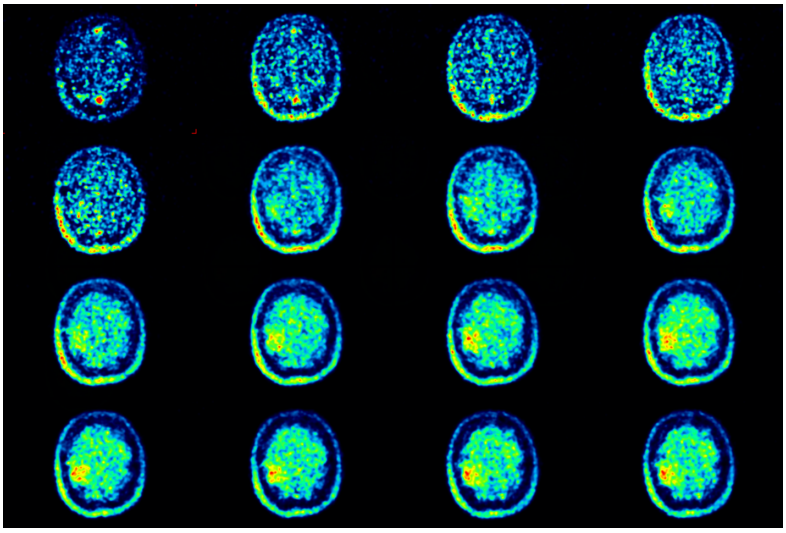

Figure 6.12.: The data of 50 min acquisition are framed and reconstructed with a duration 5 s at the beginning (after injection) up to 5 min towards the end of the acqusition. The enhancement of FET tracer in the tumour is much higher than in the healthy brain tissue.

Besides the high accuracy found in the phantom scans, the cross calibration can be confirmed in *in vivo* MR-PET studies.

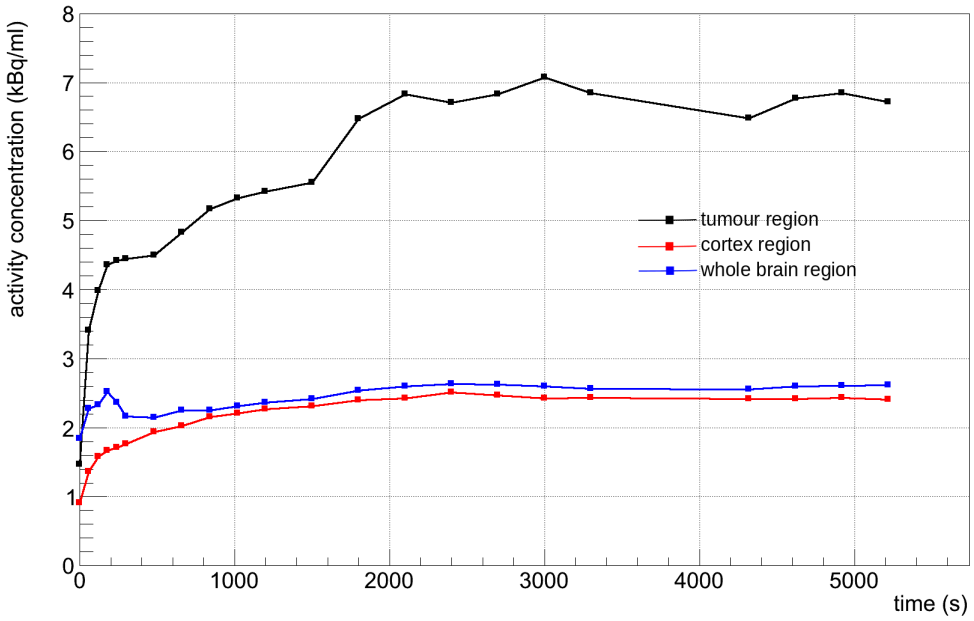

Figure 6.13.: FET time activity curve of the reconstructed time frames acquired with the BrainPET (first 18 data points) and HR+ (last 4 data points). Blue curve shows the data in the arterial ROI (80 voxel), red the cortex ROI (14000 voxel) and black curve shows the tumor ROI (180 voxel). The statistical fluctuations and uncertainties due to patient motion increase with decreasing ROI size.

6.2.2. [^{18}F]-FDG-PET/MRI Studies

The PET tracer [^{18}F]-Flurdesoxyglucose (2-Fluor-2-desoxy-D-glucose, FDG) is the mostly applied PET tracer. It is a glucose analogue and used to visualise the local glucose metabolism, i.e. tracer uptake and phosphorylation by the living cells. After injection the FDG is transported into the cells. The successive phosphorylation prevents the molecule to be released from the cell. However, due to the replacement of the hydroxyl group (OH) by the ^{18}F-atom, it cannot be metabolised further. The FDG molecule is trapped in the glucose consuming cell and the positron emitting tracer enhances over time. This mechanism is referred to as metabolic trapping. FDG images represent the glucose consumption rate as depicted in Figure 6.14, showing the reconstructed acquisition data of 20 – 50 min post injection. The patient suffering from Alzheimers desease (AD) was scanned in the 3T MR-BrainPET and subsequently in the Siemens HR+ scanner. Comparing the images of these two scanners, the better delineation of the cortex which is achieved with the BrainPET can be clearly seen.
The ratio FDG uptake in GM and WM is usually in a ratio of approximately 4:1 and should be reflected in the image. Compared to whole body scanners, the high resolution of the BrainPET allows for a high delineation of the cortex and other glucose consuming stuctures in the brain. The uptake of FDG in the human brain leads to moderate countrates of approximately 300 – 400 kcps (trues + scatter) with a decelerated convergence of the ML-EM algorithm compared to FET-PET. For the countrates achieved in human FDG studies, the correction procedures perform well. Also the dynamic range of the studies was well covered by the dynamic correction for deadtime as analysed in detailed phantom studies before.
The images depicted in Figure 6.15 indicate the image quality in the FDG scan applying 3 iterations of scatter correction. Especially the higher number of ML-EM iterations (128 compared to 64) lead to a higher contrast and thus to a better separation of GM and WM. The vertical streak artefacts, present in early studies, have been reduced by an improved setup and the adaption of the coil template (more obvious in Figure 6.17). The quantitative combined BrainPET/HR+ study is assessed in Figure 6.16. Again, the data of BrainPET and HR+ are qualitatively and also quantitatively in good agreement, indicating the *in vivo* comparability of the data sets.

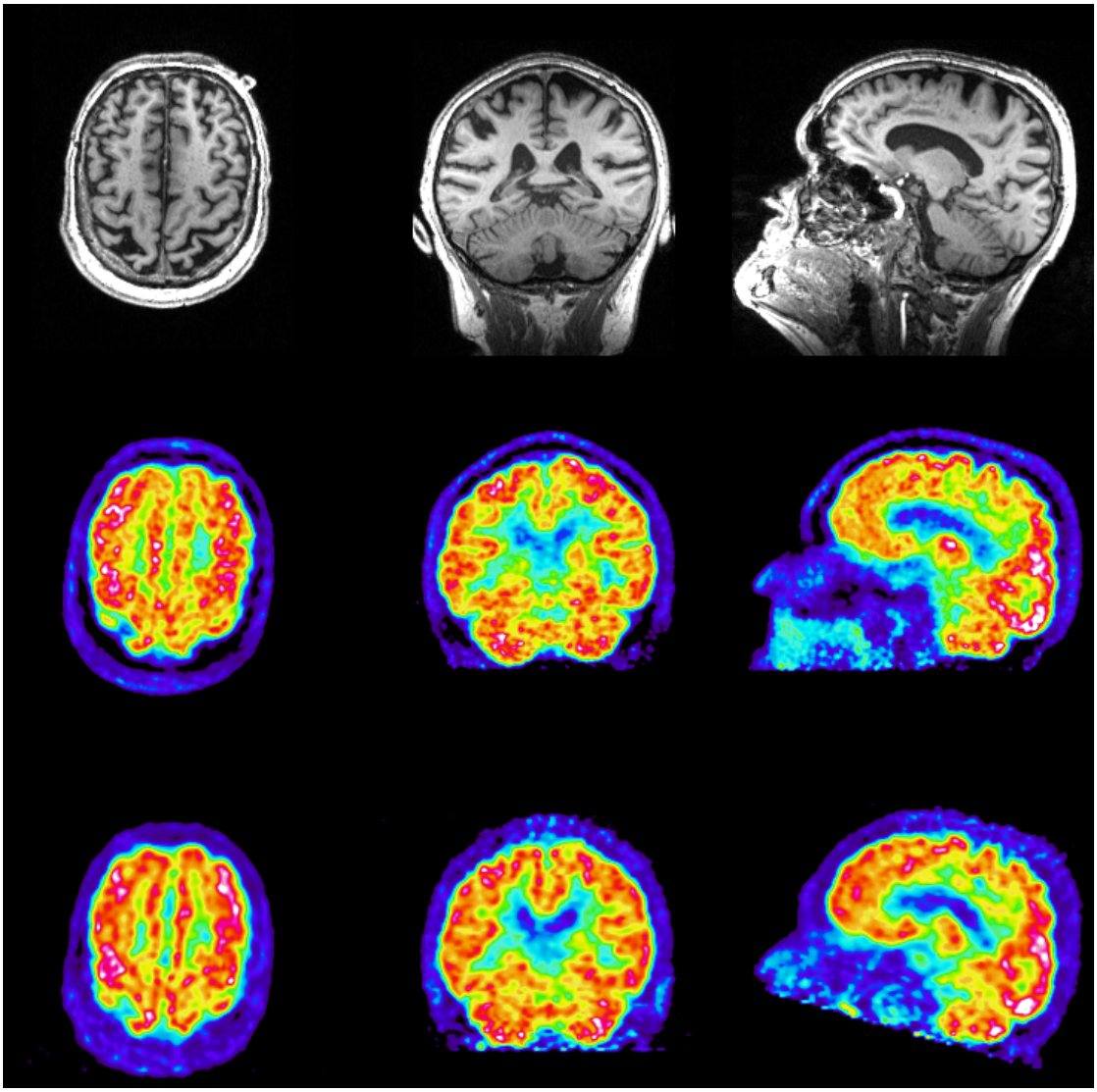

Figure 6.14.: The first row shows anatomical MP-RAGE image. The middle row shows the glucose consumption in the [^{18}F]-FDG-PET images acquired with the BrainPET. For comparison, the same patient was scanned in the HR+ scanner (lower row).

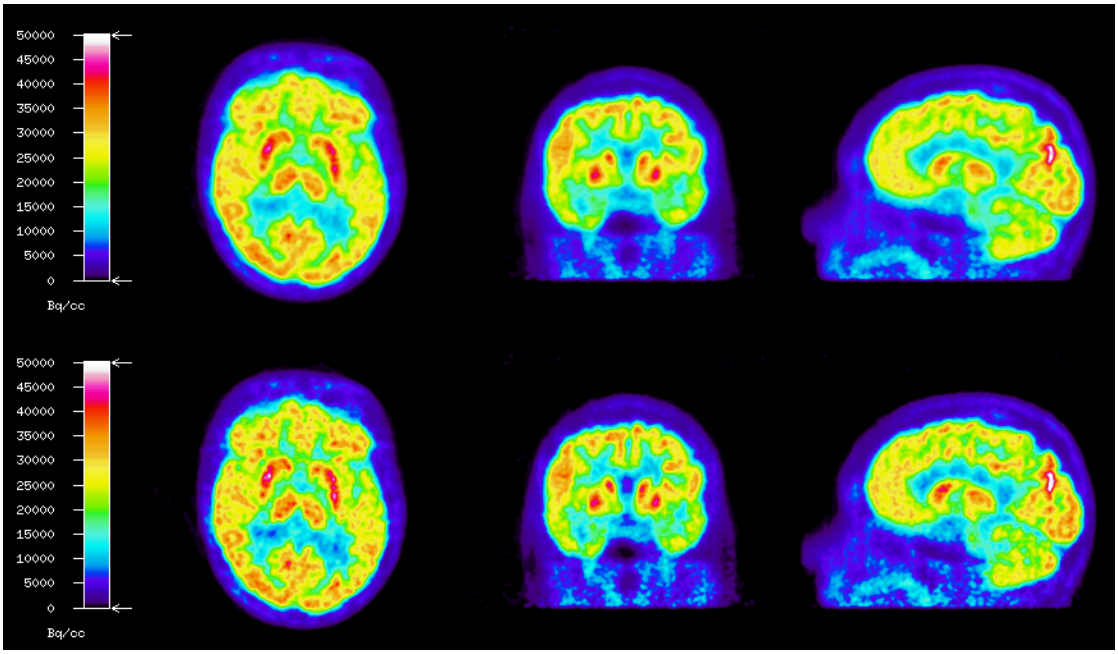

Figure 6.15.: Human ^{18}F-FDG study: Comparison of standard reconstruction procedure with 64 ML-EM iterations (upper row) and 128 ML-EM iterations (lower row). The latter one leads to a higher image contrast and to a sharper separation between GM and WM.

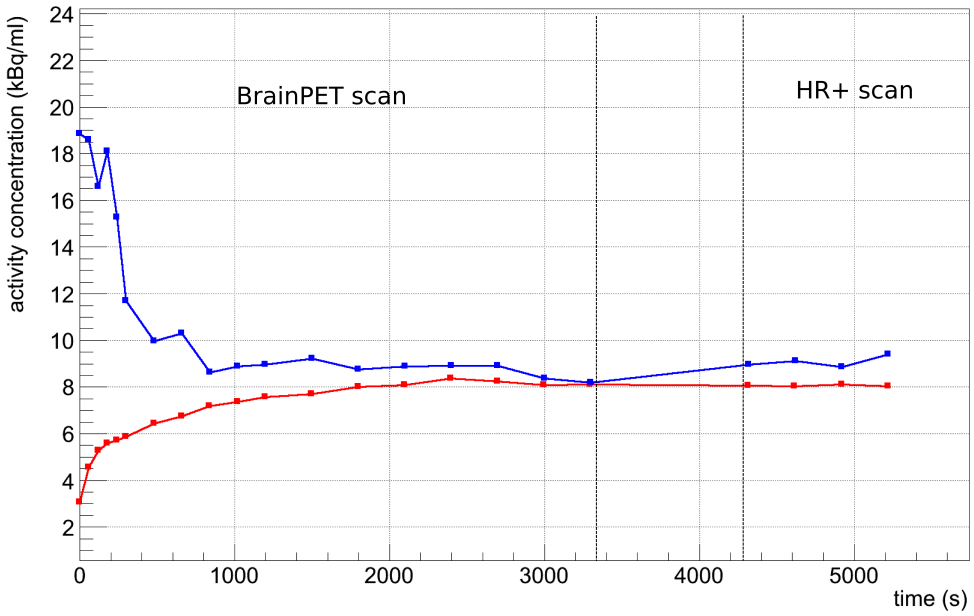

Figure 6.16.: FDG time activity curve of the reconstructed time frames acquired with the BrainPET (first 18 data points) and HR+ (last 4 data points). The curves show the arterial input function (AIF, blue curve) and the whole brain region (red). The higher level of the AIF curve in the HR+ measurement is likely due to the higher partial volume effect on the HR+ scanner.

6.2.3. [^{11}C]-Flumazenil-PET/MRI Studies

The radiotracer [^{11}C]-Flumazenil is applied in PET to study benzodiazepine receptors. In epileptic patients the attention is payed on focal abnormalities. Local reduction in flumazenil binding was found to be correlated with the side and size of seizure onset [33, 83].
In order to make precise statements on focal abnormalities in [^{11}C]-Flumazenil-PET it is of importance to have images without artefacts and with high resolution. With the achieved improvements of this work, an excellent image quality is provided (see Figure 6.17). Since structual abnormalities, such as hippocampal atrophy were reported [83], simultaneous MRI combined with the high resolution of the BrainPET may be advantageous. However, this has to be proven and exploited by further detailed human studies.

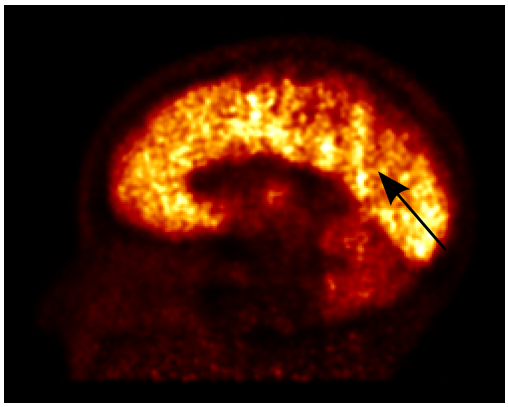

(a) Sagittal view of human ^{11}C-Flumazenil-PET scan. Vertical streak artefacts are clearly visible, as indicated by the arrow.

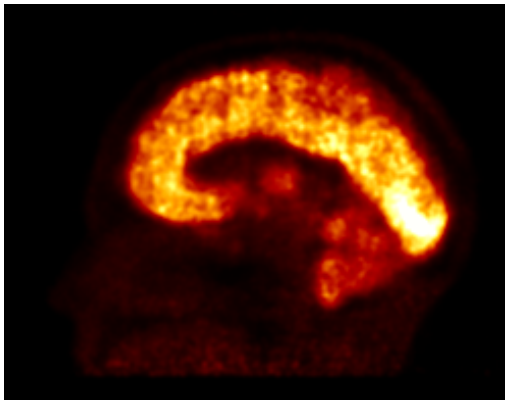

(b) Sagittal view of human ^{11}C-flumazenil-PET scan. Vertical streak artefacts have been significantly reduced.

Figure 6.17.: Flumazenil PET with and without streak artefacts. The two scans show two different subjects to address also the enhancement of an optimal setup and attenuation template of the applied RF head coil.

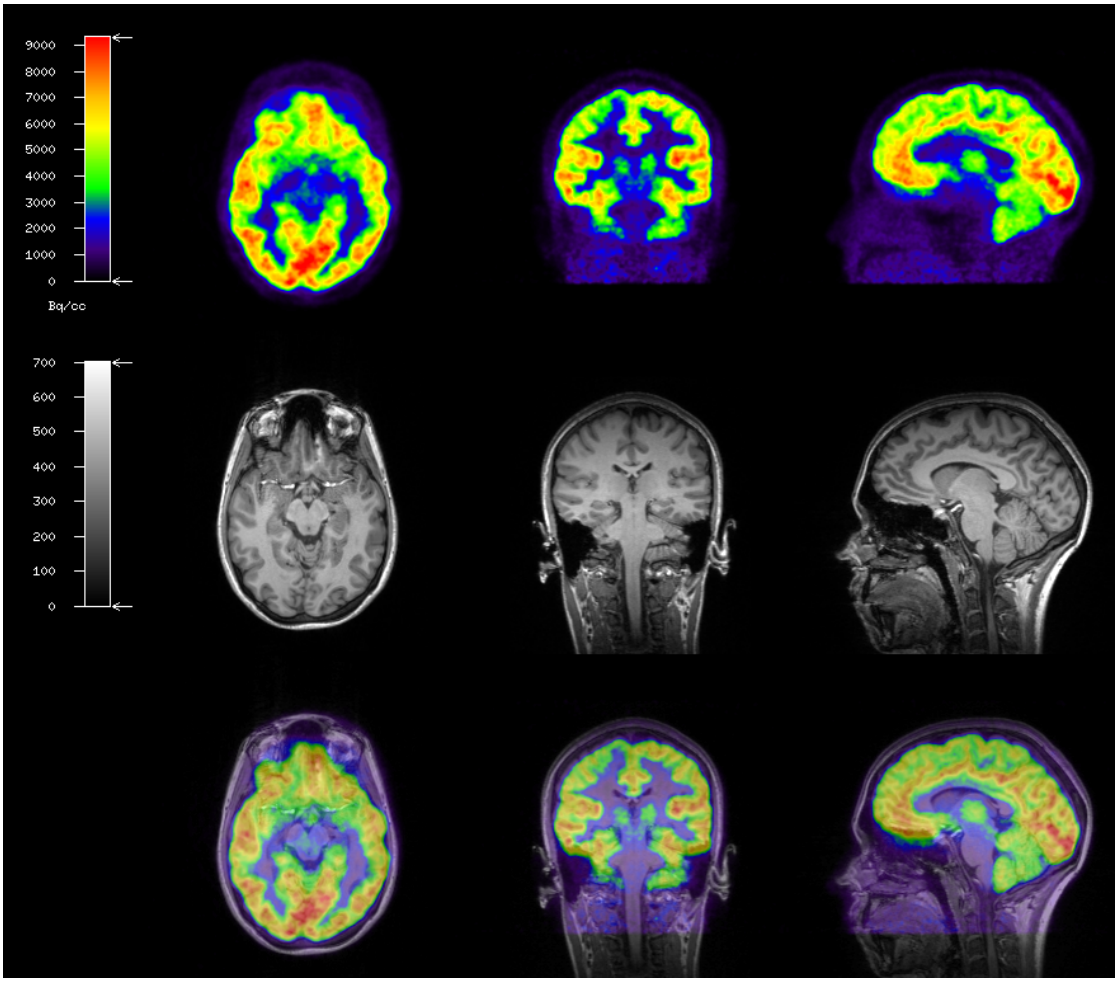

Figure 6.18.: The [^{11}C]-Flumazenil-PET images (first row) show the uptake of the ^{11}C-labelled epilepsy tracer. The second row shows the anatomical MP-RAGE image. The third row shows the fused PET and MR image.

6.2.4. [^{15}O]-Water-PET Study

Several methods are suitable for quantitative measurements of regional cerebral blood flow (rCBF) applying PET or MRI including CO_2^{11} PET [52]. However, the most often used PET tracer is labelled water ($H_2^{15}O$) [35, 5]. With the very short half life of only 120 s the relatively high activity can be administered to the subject and still results in a low radiation dose. Due to the high permeability of the blood brain barrier for water combined with the high perfusion of the human brain, a high activity concentration is achieved in the volume of interest. This results in a very high countrate for the PET scanner leading to a high deadtime and a high random coincidence rate. Consequently, the correction of these effects in water studies is demanding.

The acquisition time in the presented PET study is 180 s. In order to assess the time response of the tracer, the acquired listmode data are subdivided into 28 frames, with minimal length of 3 s at the beginning and maximal length of 10 s towards the end of the acquisition. In Section 5.3 it was shown that the quantitative error (positive bias) can increase significantly, when applying a framing scheme with high temporal resolution. This leads to short frames with high statistical uncertainties. In order to analyse the error due to the high number of frames, the sum of the 28 reconstructed images is compared to the reconstructed sum of counts. It turns out that the mean value in a large cortical ROI in the sum of the 28 images is 14.50 kBq/ml whereas in the same ROI of the reconstructed sum of counts is 13.43 kBq/ml (applying 32 iterations with 2 subsets). So, the reconstructed sum of counts is in good agreement with the sum of the reconstructed single images. However, due to the remarkable random fraction, the convergence of the OP-OSEM algorithm is rather slow, and thus a higher number of iteration shows a contrast enhancement at costs of higher noise in the image. In order to exploit the image resolution of the scanner, the parameters 64 iterations with 2 subsets were applied. The comparision is given in Figure 6.19(a). The example of the TAC showing the time response of the whole brain region is given in Figure 6.19(b).

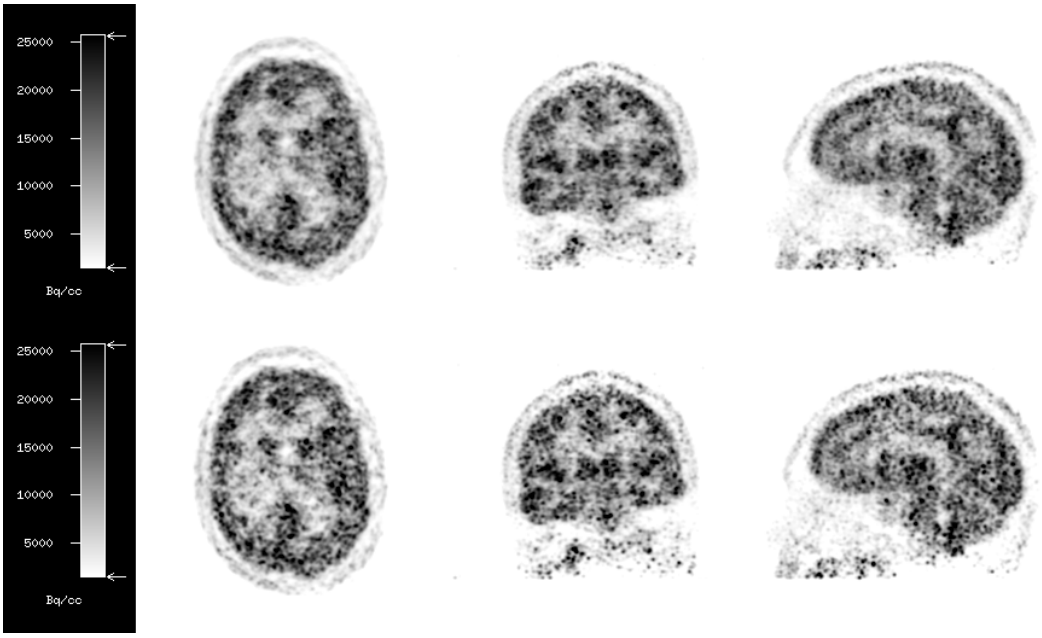

(a) ^{15}O-Water PET Study (180 s acquisition time). Upper row: standard procedure with 64 ML-EM iterations, lower row: procedure with 128 ML-EM iterations. Besides the reduced background outside the human head, also a significant contrast enhancement between GM and WM can be observed.

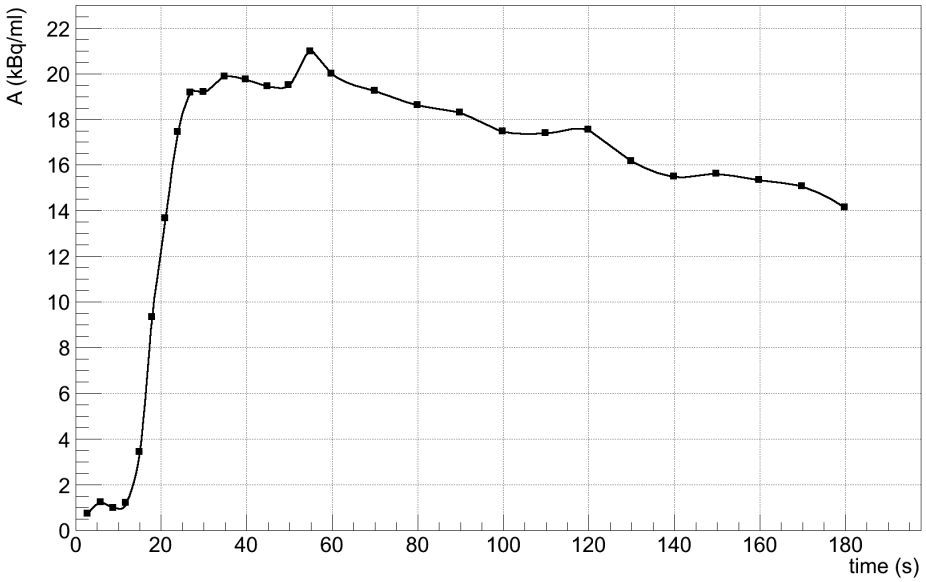

(b) Time activity curve of the 180 s scan, subdivided into 28 frames of different length.

Figure 6.19.: Reconstructed images (a) and TAC of a whole-brain (WB) region in a dynamic ^{15}O-Water PET Study (b).

6.2.5. Summary

A higher number than the current standard of 64 ML-EM iterations has to be selected to assure convergence of the reconstruction. This holds especially in studies with high random and scatter fraction. This is less important for FET-PET, since images converge early and high iteration numbers will increase the noise. In water-PET studies, the high number of ML-EM iterations is crucial to assure the contrast and exploit the high image resolution of the BrainPET. This has been derived from in the phantom studies and transfers to the human PET measurements. The versatile PET tracers acquired simultaneously to MR sequences show an excellent image quality together with an accurate quantification.

7. Discussion

Hybrid imaging of MRI and PET has been realised for the first time for human applications with the MR-BrainPET scanners [30, 88]. A variety of MR contrasts and parameters can be acquired simultaneously to high resolution PET images [16, 37]. Two hybrid MR-BrainPET scanners have been installed in the Forschungszentrum Jülich, one combining the BrainPET with a Siemens 3T Tim Trio MR scanner and one with a newly developed 9.4T MR scanner [91].
The APD based block detector technology applied by the BrainPET was expected to be critical regarding stability and temperature dependency [81], especially due to the air cooling of the detectors with the low thermal capacity of air. It has been confirmed in long term studies with ^{68}Ge-cylinder phantoms that the detector and the crystal efficiencies are adequately stable over time. The adaptive air cooling and a monthly normalisation measurement together with weekly calibration scans were found to guarantee a stable configuration for PET imaging with the MR-BrainPET scanners.
Characteristics such as sensitivity, countrate performance and image resolution are inherent to a PET scanner and have been assessed first. Statistical uncertainties, intrinsic to a counting experiment such as PET, can be reduced by increasing the sensitivity. For the BrainPET the line source sensitivity was found to be 0.6 % in the transaxial centre and 0.9 % for a transaxial offset of 10 cm. For point sources, the peak sensitivity was detected at the centre of the FOV with 6.7 % (5.3 % at 10 cm radial offset) which is beneficial compared e.g. to the sensitivity of the Siemens HRRT (4.7 % for a point source [50]). However, for highly specific tracers with low overall uptake or for very short frames the number of acquired counts can still be small. This leads to increased noise in the reconstructed radioactivity distribution, and the less reliable basis has to be considered for the mandatory data corrections. The high intrinsic resolution of the BrainPET scanner, and the choice of appropriate image reconstruction software such as an LOR-based reconstruction software allow for a more accurate quantification, even of small structures [86]. The reconstructed image resolution of the BrainPET was found to be 2.79 mm radially (2.66 mm tangentially and 3.36 mm axially) at the centre of the FOV, re-

constructed with an implementation of the FBP algorithm [99] according to the NEMA standard [4]. Limited resolution leads to a degradation of activity concentration in small structures, compromising for example the estimation of activity in small vessels [113]. This partial volume effect is inherent to PET scanners and corrections are available [28]. Physically, the resolution is not only limited by the selected crystal size and the material applied in detector design, but also the effect of the positron range and acollinearity of the two emitted gamma photons after annihilation. The former effect can induce uncertainties in particular for emissions in or near locations with very small cross section for positron interaction, such as the lung. Here, the application of a strong magnetic field as present in the 9.4T MR-BrainPET can reduce the positron range perpendicular to the static magnetic field vector and improve image resolution for isotopes with high positron energy [36].

The exact quantification of PET images with hybrid MR-PET scanners is a complex task with versatile sources of errors [19]. Uncertainties in the determination of activity concentrations can be caused by either physical effects, such as Compton scattering and photon attenuation, or imperfections in the measurement process and data processing, such as detector deadtime and pulse pile-up. The inhomogeneity of crystal efficiencies is corrected by the normalisation. The application of a DN or CBN procedure assures the compensation of varying crystal efficiencies among the detector elements [7]. The CBN provides a noise reduced correction compared to a DN. Since there is no difference in image reconstruction time between both approaches, the CBN is applied here. It is widely accepted that VR on randoms improves quantification and SNR, which is especially important in frames with low count sum. The evaluation of the implemented VRR algorithm [17] reveals excellent performance at all levels of count sums, reducing the positive bias at low statistics frames. Furthermore, deadtime properties of the measurement and also linearity regarding the count sum within the frames are preserved by the VRR algorithm.

PET is regarded as a quantitative modality, not least due to the accurate formulation of the attenuation correction. The separation of photon emission and transmission properties for image reconstruction allows for a post processing correction of the beam attenuation. However, the over- or underestimation caused by imperfect attenuation information can result in severe image artefacts, which are not only due to an erroneous assignment of attenuation values to tissue and materials, but also due to mispositioning of the attenuation map or motion artefacts during the measurement of subject and RF coil. Deriving attenuation properties

from MR images is an issue of ongoing research and development. For attenuation of the human head, several approaches exist [20, 39, 40, 48]. A template based AC is applied in Jülich, since it is robust and requires minimal user interaction [82]. In MR-PET applications the photon attenuation and Compton scattering caused by the RF coils of the MRI scanner have also to be taken into account. Regarding the birdcage coil not only the sensitivity reduction is an issue, but also the degradation in image quality due its small, but transaxially symmetric structures. The applied RF coil design and material is optimised regarding photon attenuation and scattering. An accurately performed correction is crucial in order to avoid longitudinal streak artefacts in the image. This has been improved significantly by adapting the attenuation map of the coil (see Section 5.2).
The Compton scatter correction is a prerequisite for 3D acquisition with scatter fractions of up to 30 – 50 % in one LOR [102]. Since the scatter simulation requires an attenuation map of the subject, the outcome of the simulation is also sensitive to the accuracy of the attenuation data. Furthermore, scatter simulation requires an emission image as input for the computation. However, a first estimate suffers from activity overestimation, since it still includes the scattered events. In a second iteration, the image suffers from underestimation, but with reduced bias. Consequently, the scatter correction shows a higher accuracy, if applied in more than two iterations, as also shown in Section 5.3 and [42]. Mostly due to the longer reconstruction times of this approach, it is not yet a clinical standard and also in our standard reconstruction procedure it is only available optionally. The statistical noise in the acquired sinogram data as well as in the emission image can lead to an erroneous estimate of the scatter fraction and thus to larger errors in the final quantitative image.
The dynamic behaviour of efficiencies caused by the deadtime of the detector blocks and the subsequent electronics together with the pulse pileup at high countrates is accounted by a combined deadtime and pileup correction. It is capable of improving the image homogeneity compared to the global deadtime correction approach. The dynamic behaviour of single crystals has also been investigated and a correction procedure has been implemented and assessed. Despite the first promising results the establishment of the method requires further investigation regarding image quality and stability to be applied in the standard reconstruction. Also the consideration of the applied radiopharmaceutical, its physical half life and also the biological course and the injected dose play an important role in this regard.
Besides the well established corrections for PET, the new aspect of mutual interference in simultaneous MR-PET imaging has been taken into account. The

effect of MRI on the PET countrate has been quantified to be less than 2 % for the 3T MR-BrainPET and can be neglegted in most clinical studies. However, it can be corrected with the implemented procedure [104]. All the correction procedures are combined and implemented in a user friendly framework, which allows the reconstruction of acquired data to calibrated images in the ECAT7 format.
Versatile phantom studies have been performed, applying the radioisotopes ^{11}C, ^{15}O, ^{18}F, ^{45}Ti, ^{68}Ge/^{68}Ga, ^{68}Ga and ^{120}I, in order to evaluate and optimise the correction methods and to guarantee the overall quantification of the reconstructed images. Mainly two experiments can be highlighted which are capable to reflect the quantitative accuracy. Firstly, a decay experiment applying a homogeneously filled cylinder with ^{18}F-diluted water was conducted. The acquired and reconstructed images of 10 frames, traversing a high dynamic range of activity concentrations covering all clinical situations in terms of count rate were evaluated. The quantification error here has been found to vary between -2.2 % for high countrate frames and 4.4 % in very low countrate frames (see Section 6.1.1). The issue of bias in low statistic frames has already been reported for the Siemens HRRT scanner [77]. Secondly, a two chamber phantom study has been performed, where the ratio of activities (here: 4.15:1) is reliably recovered in the reconstructed image. The study showed that a high number of iterations is necessary in order to approach convergence of the OP-OSEM algorithm. As already seen for cylinder measurements, the three iterations of scatter correction are also advantageous in regards of contrast recovery in the study with the two chamber phantom (see Section 6.1.2).
Finally, the *in vivo* quantification of PET images applying the various methods developed and improved in this thesis was assessed. Quantitative imaging of different PET tracers, namely ^{18}F-FDG and ^{18}F-FET, have been cross validated with the commercial Siemens ECAT HR+ scanner. Furthermore, ^{11}C-Flumazenil and ^{15}O-water studies were conducted, each with specific physiological and physical course and fate, leading to various challenges in quantification and image quality. The images have been evaluated regarding artefacts and the performance of the critical corrections, e.g. random and deadtime for the ^{15}O-water scans. The phantom study results are confirmed by the outcome of the *in vivo* studies, where the quantitative evaluation of the BrainPET data is in good agreement with the Siemens ECAT HR+ data. Compared to clinical PET/CT scanners, the BrainPET component shows superior image resolution. The image quality of the BrainPET is comparable to images of the high resolution HRRT scanner, but the MR-BrainPET scanners offer now the additional information of simultaneously performed MRI protocols.

8. Summary

8.1. Conclusion

In this work the quantification of PET imaging with the hybrid MR-BrainPET scanners has been realised and evaluated. The mandatory correction procedures have been developed and implemented. Especially, the properties and accuracy of manufacturer provided component based normalisation and Compton scatter correction procedure have been analysed. Besides, the new aspect of interference of MRI on PET imaging during simultaneous MR-PET studies has been intensively investigated. Even though for most studies these effects are negligible, for neuroreceptor PET studies they become important. Thus, a correction for the found effects has been implemented and can be applied optionally in the reconstruction framework. Furthermore, the dynamic sensitivity effects at varying countrates have been compensated, including deadtime and pileup correction. Also the photon attenuation caused by the RF coil of the MR component has been taken into account. The template based attenuation correction, together with the other procedures, has been integrated in a reconstruction framework in order to obtain calibrated images from acquired listmode data with minimal user interaction. Calibration of the system is achieved evaluating a sequence of calibration phantom scans which are compared to gamma counter probes and to PET measurements acquired with a Siemens ECAT HR+ scanner. The main performance parameters of the scanner hardware and the developed software components were determined applying the NEMA standard. Additional measurements to evaluate countrate properties, image resolution, sensitivity and the overall quantification were performed. The reconstruction framework is applicable in phantom studies as well as in human MR-PET studies in our institute. Versatile phantom studies with different geometries, radioisotopes and countrates have been performed in order to further optimise correction procedures and finally assess the quantitative accuracy. With daily applied quality control measurements, the long term stability was demonstrated.
Finally, human studies applying quantitative PET imaging in simultaneous MR-

PET studies were performed and evaluated. Versatile PET radiotracers, such as ^{18}F-FDG, ^{18}F-FET, ^{11}C-Flumazenil and ^{15}O-Water were applied, each with specific physiological and physical properties, leading to various challenges in quantification and image quality. It can be concluded that quantification of the high resolution PET images acquired with the MR-BrainPET scanner has been realised.
With the state of the art accuracy in quantification and the high resolution of the PET scanner combined with simultaneous MRI, the 3T MR-BrainPET and in the near future also the 9.4T MR-BrainPET scanners are outstanding devices for neuroimaging.

8.2. Outlook

Even though quantification of PET images has been achieved in a robust workflow, several improvements are viable. One is the improvement of the Compton scatter correction procedure to allow for a more robust scatter estimation even in frames with low statistics. Related to the scatter correction, the vital topic of MR based attenuation correction, which is even more demanding at whole body MR-PET, has to be further investigated. Improving MR sequences for bone detection would allow for an even more robust separation between bone, air and tissue. The RF coil design may be further optimised regarding the attenuation properties and geometry and it should be included in the scatter correction. However, the manufacturer provided scatter correction does not allow such a modification.
The design of future PET components in MR-PET scanners should take care of reducing the gap structure between adjacent detector blocks in order to avoid the challenging scatter behaviour. Besides the geometry, the shielding and filtering of the analogue PET signals should be improved in order to further reduce the residual signal induction of switching gradients during simultaneous MR-PET studies. Also, an alternative motion detection procedure, either with a camera system or MR navigator sequences may be applied. Finally, the co-registration of acquired volumes in MRI and PET, especially accounting for possible image distortions in different MRI sequences should be further investigated and improved. The preclinical and clinical task of developing dedicated MR-PET protocols to exploit the full potential of the new powerful multi-modal tool will contribute to the further acceptance of MR-PET in neuroscience and clinical applications in the near future.

Bibliography

[1] National Electrical Manufacturers Association (NEMA) Standards Publication NU 2-1994. 1994.

[2] National Electrical Manufacturers Association (NEMA) Standards Publication NU 2-2001. 2001.

[3] Timing Calibration in PET Using a Time Alignment Probe. *IEEE, Trans. Nucl. Sci.*, 53(5):2660–2665, 2006.

[4] National Electrical Manufacturers Association (NEMA) Standards Publication NU 2-2007. 2007.

[5] Optimization of methods for quantification of rCBF using high-resolution 15-O H2O PET images. *Phys. Med. Biol.*, 57:2251–2271, 2012.

[6] B. Atkins, D. Pressley, M. Lenox, B. Swann, D. Newport, and S. Siegel. A Data Acquisition, Event Processing and Coincidence Determination Module for a Distributed Parallel Processing Architecture for PET and SPECT Imaging. *Nuclear Science Symposium Conference Record*, 4:2439 – 2442, 2006.

[7] R. Badawi and P. Marsden. Developments in component-based normalization for 3D PET. *Phys. Med. Biol*, 44(2):571–94, 1999.

[8] R. Badawi, M. Miller, D. Bailey, and P. Marsden. Randoms variance reduction in 3D PET. *Imaging*, 941, 1999.

[9] B. Bai and Q. Li. Model-based normalization for iterative 3D PET image reconstruction. *Phys. Med. Biol*, 47:2773 – 2784, 2002.

[10] Y. Berker, J. Franke, A. Salomon, M. Palmowski, H. Donker, Y. Temur, F. Mottaghy, C. Kuhl, D. Izquierdo-Garcia, Z. Fayad, F. Kiessling, and V. Schulz. MRI-based attenuation correction for hybrid PET/MRI systems:

a 4-class tissue segmentation technique using a combined ultrashort-echo-time/Dixon MRI sequence. *J. Nucl. Med.*, 53:796–804, 2012.

[11] Y. Berker, A. Salomon, F. Kiessling, and V. Schulz. Lung Attenuation Coefficient Estimation Using Maximum Likelihood Reconstruction of Attenuation and Activity for PET/MR Attenuation Correction. pages 2282–4, 2012.

[12] M. Bernstein, K. King, and J. Zhou, editors. *Handbook of MRI Pulse Sequences*. Academic Press, 2004.

[13] T. Beyer, D. Townsend, and T. Brun. A combined PET/CT scanner for clinical oncology. *J. Nucl. Med.*, 41:1369–1379, 2000.

[14] F. Bloch. Nuclear induction. *Phys. Rev.*, 70:460 – 473, 1946.

[15] J. Blumhagen, R. Ladebeck, M. Fenchel, and K. Scheffler. MR-based field-of-view extension in MR/PET: B0 homogenization using gradient enhancement (HUGE). *Magnetic Resonance in Medicine*, 2012.

[16] A. Boss, S. Bisdas, A. Kolb, M. Hofmann, U. Ernemann, C. Claussen, C. Pfannenberg, B. Pichler, M. Reimold, and L. Stegger. Hybrid PET/MRI of intracranial masses: initial experiences and comparison to PET/CT. *J Nucl Med*, 51(8):1198–1205, 2010.

[17] L. Byars, M. Sibomana, Z. Burbar, J. Jones, V. Panin, W. Barker, J. Liow, R. Carson, and C. Michel. Variance Reduction on Randoms from Delayed Coincidence Histograms for the HRRT. *IEEE Nuclear Science Symposium Conference Record, 2005*, pages 2622–2626, 2005.

[18] J. Carney, D. Townsend, V. Rappoport, and B. Bendriem. Method for transforming CT images for attenuation correction in PET/CT imaging. *Med Phys.*, 33(4):976–983, 2006.

[19] R. Carson. *Positron Emission Tomography*, chapter Tracer Kinetic Modeling in PET. Springer Science + Business Media, 2005.

[20] C. Catana, A. van der Kouwe, T. Benner, C. Michel, M. Hamm, M. Fenchel, B. Fischl, B. Rosen, M. Schmand, and G. Sorensen. Toward Implementing an MRI-Based PET Attenuation-Correction Method for Neurologic Studies on the MR-PET Brain Prototype. *J. Nucl. Med.*, 51(9):1431–8, 2010.

[21] C. Catana, Y. Wu, M. Judenhofer, J. Qi, B. Pichler, and S. Cherry. Simultaneous acquisition of multislice PET and MR images: Initial results with a MR-compatible PET scanner. *J. Nucl. Med.*, 47(12):1968–1976, 2006.

[22] S. Cherry, J. Sorenson, and M. Phelps, editors. *Physics in Nuclear Medicine*. Elsevier Science, 2003.

[23] N. da Silva, H. Herzog, C. Weirich, L. Tellmann, E. Rota Kops, H. Hautzel, and P. Almeida. Image-Derived Input Funcion Obtained in a 3TMR-BrainPET. *NIMA*, 2012.

[24] M. Daube-Witherspoon and R. Carson. Unified deadtime correction model for PET. *IEEE Trans. Med. Imag.*, 10:267–275, 1991.

[25] Hevesy G. de. The absorption and translocation of lead by plants. *Biochem. J.*, 17(439), 1923.

[26] G. de Hevesy and F. Paneth. Die Löslichkeit des Bleisulfids und Bleichromats. *Zeit. Anorg. Chem.*, 82(323), 1913.

[27] P. Dueppenbecker, J. Wehner, W. Renz, S. Lodomez, D. Truhn, P. Marsden, and V. Schulz. Gradient Transparent RF Housing for Simultaneous PET / MRI Using Carbon Fiber Composites. *IEEE NSS/MIC Conference Record*, pages 3478–80, 2012.

[28] K. Erlandsson, I. Buvat, P. Pretorius, B. Thomas, and B. Hutton. A review of partial volume correction techniques for emission tomography and their applications in neurology, cardiology and oncology. *Phys Med Biol.*, 57(21):119–159, 2012.

[29] N. Galdiks, G. Stoffels, C Filss, M. Piroth, M. Sabel, M. Ruge, H. Herzog, N.J. Shah, G. Fink, H. Coenen, and KJ. Langen. Role of O-(2-18F-Fluroethyl)-L-Tyrosine PET dor Differentiation of Local Recurrent Brain Metastasis from Radiation Necrosis. *J. Nucl. Med.*, 9(59):1367 – 1374, 2012.

[30] R. Grazioso, N. Zhang, J. Corbeil, M. Schmand, R. Ladebeck, M. Vester, G. Schnur, W. Renz, and Fischer H. APD-basedPET detector for simultaneous PET/MR imaging. *Nuclear Instruments and Methods in Physics Research Section A*, 569(2):301 – 305, 2006.

[31] M. Haake, W. Brown, M. Thompson, and R. Venkatesan, editors. *Magnetic Resonance Imaging - Physical Principles an Sequence Design*. John Wiley and Sons, 1999.

[32] B. Hammer, N. Christensen, and B. Heil. Use of a magnetic field to increase the spatial resolution of positron emission tomography. *Med. Phys.*, 21:1917 – 20.

[33] A. Hammers. *Neuromethods: Molecular Imaging in the Neurosciences*, chapter Epilepsy, pages 377 – 395. Springer Science + Business Media, 2012.

[34] B. Hasegawa, E. Gingold, S. Reilly, S. Liew, and C. Cann. Description of a simultaneous emission-transmission CT system. *Proc. SPIE*, 1231:50–60, 1990.

[35] H. Herzog. Basic Ideas and Principles for Quantifying Regional Blood Flow with Nuclear Medical Techniques. *Nuklearmedizin/Nuclear Medicine*, 181(5):181–185, 1996.

[36] H. Herzog, H. Iida, C. Weirich, L. Tellmann, J. Kaffanke, S. Spellerberg, L. Caldeira, E. Rota Kops, and N.J. Shah. Influence from high and ultra-high magnetic field on positron range measured with a 9.4TMR-BrainPET. *IEEE Nuclear Science Symposium Conference Record*, pages 3410 – 3413, 2010.

[37] H. Herzog, K. Langen, C. Weirich, E. Rota Kops, J. Kaffanke, L. Tellmann, J. Scheins, I. Neuner, G. Stoffels, K. Fischer, L. Caldeira, H. Coenen, and N.J. Shah. High resolution BrainPET combined with simultaneous MRI. *Nuklearmedizin*, pages 1–9, 2011.

[38] H. Herzog and J. van den Hoff. Combined PET/MR systems: an overview and comparison of currently available options. *Q J Nucl Med Mol Imaging*, 56(6):247–267, 2012.

[39] M. Hofmann, B. Pichler, B. Schölkopf, and T. Beyer. Towards quantitative PET/MRI: a review of MR-based attenuation correction techniques. *European journal of nuclear medicine and molecular imaging*, 36 Suppl 1:S93–104, 2009.

[40] M. Hofmann, F. Steinke, V. Scheel, G. Charpiat, J. Brady, and B. Pichler. MR-based PET Attenuation Correction – Method and Validation. *Medical Physics*, pages 4–5.

[41] I. Hong, S. Chung, H. Kim, Y. Kim, Y. Son, and Cho Z. Ultra fast symmetry and SIMD-based projection-backprojection (SSP) algorithm for 3-D PET image reconstruction. *IEEE Trans. Med. Imag.*, 26(6):789–803, 2007.

[42] I. Hong, M. Conti, and Z. Burbar. A method to reduce bias in Iterative Scatter Correction estimate for PET. *IEEE Nuclear Science Symposium, Abstract*, 2012.

[43] H. Hudson and R. Larkin. Accelerated image reconstruction using ordered subsets of projection data. *IEEE Trans. Med. Imag.*, 13(4):601–9, January 1994.

[44] H. Iida, I. Kanno, S. Miura, M. Murakami, K. Takahashi, and K. Uemura. A simulation study to reduce positron annihilation spread distributions using a strong magnetic field in positron emission tomography. *IEEE Trans. Nucl. Sci.*, 33:597–600, 1986.

[45] S. James, Y. Yang, Y. Wu, R. Farrell, P. Dokhale, KS. Shah, and SR. Cherry. Experimental characterization and system simulations of depth of interaction PET detectors using 0.5 mm and 0.7 mm LSO arrays. *Phys Med Biol.*, 54(14):4605 – 4619, 2009.

[46] D. Kadrmas. LOR-OSEM: Statistical PET reconstruction from raw line-of-response histograms. *Phys.Med. Biol.*, 49:4731–4744, 2004.

[47] J. Karp, S. Surti, M. Daube-Witherspoon, and G. Muehllehner. Benefit of time-of-flight PET: experimental and clinical results. *J Nucl. Med.*, 3(49):462 – 470, 2008.

[48] V. Keereman, Y. Fierens, T. Broux, Y. De Deene, M. Lonneux, and Vandenberghe S. MRI-based attenuation correction for PET/MRI using ultrashort echo time sequences. *J. Nucl. Med.*, 51(5):812–820, 2010.

[49] V. Keereman, P. Mollet, Y. Berker, V. Schulz, and S. Vandenberghe. Challenges and current methods for attenuation correction in PET/MR. *MAGMA*, 26:81–98, 2013.

[50] C. Knöß. *Evaluation and Optimization of the High Resolution Research Tomograph (HRRT).*

[51] A. Kolb, H. Wehrl, M. Hofmann, M. Judenhofer, L. Eriksson, R. Ladebeck, M. Lichy, L. Byars, C. Michel, HP. Schlemmer, M. Schmand, C. Claussen, V. Sossi, and B. Pichler. Technical performance evaluation of a human brain PET/MRI system. *European radiology*, 22(8):1776–88, August 2012.

[52] A. Lammertsma, R. Frackowiak, J. Hoffman, S. Huang, I. Weinberg, M. Dahlbom, N. MacDonald, E. Hoffman, J. Mazziotta, and J. Heather. The C-15 O2 build-up technique to measure regional cerebral blood flow and volume of distribution of water. *J Cereb Blood Flow Metab.*, 9(4):461–470, 1989.

[53] K. Lange and R. Carson. EM reconstructionn algorithms for emission and transmission tomography. *J. Comput. Assist. Tomogr.*, 8:306–316, 1984.

[54] KJ. Langen, K. Hamacher, M. Weckesser, F. Floeth, G. Stoffels, D. Bauer, HH. Cienen, and D. Pauleit. O-2-[18F]fluroethyl-L-tyrosine: uptake mechanisms and clinical applications. *Nuclear Medicine and Biology*, 33:287 – 294, 2006.

[55] P. Lauterbur. Image formation by induced local interactions: Examples employing nuclear magnetic resonance. *Nature*, (242):190 – 191, 1973.

[56] T. Lewellen. Time-of-flight PET. *Semin Nucl Med.*, (28):268 – 275, 1998.

[57] P. Lohmann. Stability and Performance Evaluation of an MR-compatible BrainPET. *Master Thesis*, 2012.

[58] A. Lucas, R. Hawkes, R. Ansorge, G. Williams, R. Nutt, J. Clark, T. Fryer, and T. Carpenter. Development of a combined microPET-MR system. *Technol. Cancer Res. Treat.*, 5(4):337–341, 2006.

[59] L. MacDonald, S. Kohlmyer, C. Liu, T. Lewellen, and Kinahan P. Effects of MR surface coils on PET quantification. *Med Phys.*, (6):2948–2956, 2011.

[60] C. Melcher. Scintillation crystals for PET. *J. Nucl. Med.*, 41(6):1051–1055, jun 2000.

[61] C. Melcher, M. Spurrier, L. Eriksson, M. Eriksson, M. Schmand, G. Givens, R. Terry, T. Homant, and R. Nutt. Advances in the scintillation performance of LSO:Ce single crystals. *IEEE Trans. Nucl. Sci.*, 50(4):762–766, 2003.

[62] C. Michel, M. Schmand, X. Liu, and W.D. Heiss. Reconstruction Strategies for the HRRT. *IEEE Medical Imaging Conference Record*, 2(15):207–212, 2000.

[63] C. Michel, M. Sibomana, A. Boi, X. Bernard, M. Lonneux, M. Defrise, C. Comtat, P. Kinahan, and D. Townsend. Preserving Poisson characteristics of PET data with weighted OSEM reconstruction. *1998 IEEE Nuclear Science Symposium Conference Record.*, pages 1323–1329, 1999.

[64] W. Moses and S. Derenzo. Empirical observation of performance degradation in positron emission tomographs utilizing block detectors. *J. Nucl. Med.*, 34:101, 1993.

[65] J. Mourik, M. Lubberink, A. Schuitemaker, N. Tolboom, B. van Berckel, A. Lammertsma, and B. Boellaard. Image-derived input functions for PET brain studies. *European Journal of Nuclear Medicine and Molecular Imaging*, 36(3):463 – 471, 2009.

[66] I. Neuner, J. Kaffanke, KJ Langen, Elena Rota Kops, L. Tellmann, G. Stoffels, C. Weirich, C. Filss, J. Scheins, H. Herzog, and N.J. Shah. Multimodal imaging utilising integrated MR-PET for human brain tumour assessment. *European radiology*, 2012.

[67] D. Newport, S. Siegel, B. Swann, B. Atkins, A. McFarland, D. Pressley, M. Lenox, and R. Nutt. QuickSilver: A Flexible, Extensible, and High-Speed Architecture for Multi-Modality Imaging. *Nuclear Science Symposium Conference Record*, 4:2333 – 2334, 2006.

[68] D. Nishimura, editor. *Principles of Magnetic Resonance Imaging.* Department of Electrical Engineering, Stanford University, 1994.

[69] T. Oakes, V. Sossi, and T. Ruth. Normalization in 3D PET: comparison of detector efficiencies obtained from uniform planar and cylindrical sources. *1997 IEEE Nuclear Science Symposium Conference Record*, pages 1625–1629.

[70] S. Ogawa, T. Lee, A. Kay, and Tank D. Brain magnetic resonance imaging with contrast dependent on blood oxigenation. *Proc Natl Acad Sci.*, 87:9868 – 9872, 1990.

[71] Z. Ortuno, P. Guerra-Gutierrez, J. Rubio, G. Kontaxakis, and A. Santos. 3D-OSEM iterative image reconstruction for high-resolution PET using pre-calculated system matrix. *Nucl. Instrum. Methods Phys. Res.*

[72] S. Park, S. Soaahuthekal, S. Junnarkar, J. Pratte, S. Stoll, C. Woody, D. Schlyer, and P. Vaska. Digital Coincidence Processing for the RatCAP Conscious Rat Brain PET Scanner. *IEEE Trans. Nucl. Sci.*, 55(1):510 – 514, 2008.

[73] D. Paulus, H. Braun, B. Aklan, and H. Quick. Simultaneous PET/MR imaging: MR-based attenuation correction of local radiofrequency surface coils. *Med Phys.*, (7):4306–4315, 2012.

[74] B. Pichler, M. Judenhofer, C. Catana, J. Walton, M. Kneilling, R. Nutt, S. Siegel, C. Claussen, and S. Cherry. Performance test of an LSO-APD detector in a 7-T MRI scanner for simultaneous PET/ MRI. *J. Nucl. Med.*, 47(4):639–647, 2006.

[75] B. Pichler, B. Swann, J. Rochelle, R. Nutt, S. Cherry, and S. Siegel. Lutetium oxyorthosilicate block detector readout by avalanche photodiode arrays for high resolution animal pet. *Phys. Med. Biol.*, 49:4305, 2004.

[76] M. Piel and F. Roesch. *Neuromethods: Molecular Imaging in the Neurosciences*, chapter Radiopharmaceutical Chemestry. Springer Verlag, 2012.

[77] B. Planeta-Wilson, J. Yan, T. Mulnix, and R. Carson. Quantitative Accuracy of HRRT List-mode Reconstructions: Effect of Low Statistics. *IEEE Nucl Sci Symp Conf Rec*, pages 5121–5124, 2008.

[78] E. Purcell, H. Torrey, and R. Pound. Resonance absorption by nuclear magnetic moments in a solid. *Phys. Rev.*, 69:37 – 38, 1946.

[79] R. Raylman, B. Hammer, and N. Christensen. Combined MRI- PET scanner: A Monte Carlo evaluation of the improvements in PET re- solution due to the effects of a static homogeneous magnetic field. *IEEE Trans. Nucl. Sci.*, 43(4):2406 –2412, 1996.

[80] D. Rickey, R. Gordon, and W. Huda. On lifting the inherent limitations of positron emission tomography by using magnetic fields (MagPET). *Automedica*, 14:355–369, 1992.

[81] E. Roncali and S. Cherry. Application of silicon photomultipliers to positron emission tomography. *Ann Biomed Eng.*, (4):1358–1377, 2011.

[82] E. Rota Kops and H. Herzog. Template based Attenuation Correction for PET in MR-PET Scanners. *IEEE Nuclear Science Symposium Conference Record*, pages 3786–3789, 2008.

[83] P. Ryvlin, S. Bouvard, D. Le Bars, G. De Lamere, M.C. Gregoire, P. Kahane, J. Froment, and F. Mauguiere. Clinical utility of flumazenil-PET versus F-18 Fluorodeoxyglucose-PET and MRI in refractory partial epilepsy. *Brain*, 121:2067–2081, 1998.

[84] A. Salomon, A. Goedicke, B. Schweizer, T. Aach, and V. Schulz. Simultaneous reconstruction of activity and attenuation for PET/MR. *IEEE Trans. Med. Imaging*, 30:804–13, 2011.

[85] D. Schaart, H. van Dam, S. Seifert, R. Vinke, P. Dendooven, H. Löhner, and F. Beekman. A novel, SiPM-array-based, monolithic scintillator detector for PET. *Phys. Med. Biol*, 54(11):3501–12, 2009.

[86] J. Scheins, H. Herzog, and N.J. Shah. Fully-3D PET image reconstruction using scanner-independent, adaptive projection data and highly rotation-symmetric voxel assemblies. *IEEE Trans. Med. Imag.*, 30(3):879–92, 2011.

[87] J. Scheins, M. Ullisch, L. Tellmann, C. Weirich, E. Rota Kops, H. Herzog, and N.J. Shah. PET motion correction in LOR space using scanner-independent, adaptive projection data for image reconstruction with PRESTO. *Nuclear Science Symposium and Medical Imaging Conference (NSS/MIC)*, pages 4099 – 4101, 2011.

[88] H. Schlemmer, B. Pichler, M. Schmand, Z. Burbar, C. Michel, R. Ladebeck, K. Jattke, D. Townsend, C. Nahmias, P. Jacob, W. Heiss, and C. Claussen. Simultaneous MR/PET imaging of the human brain: feasibility study. *Radiology*, 3(248):1028–1035, 2008.

[89] V. Schulz, I. Torres-Espallardo, S. Renisch, Z. Hu, N. Ojha, P. Börnert, M. Perkuhn, T. Niendorf, W. Schäfer, H. Brockmann, T. Krohn, A. Buhl,

R. Günther, F. Mottaghy, and G. Krombach. Automatic, three-segment, MR-based attenuation correction for whole-body PET/MR data. *Eur. J. Nucl. Med. Mol. Imaging*, 38:138–52, 2011.

[90] V. Schulz, B. Weisslerl, P. Gebhardl, T. So, C. Lerche, M. Ritzert, V. Mlotok, C. Piemonte, B. Goldschmidt, S. Vandenberghe, A. Salomon, T. Schaeifter, and P. Marsden. SiPM based preclinical PET / MR Insert for a human 3 T MR : first imaging experiments. *IEEE NSS/MIC Conference Record*, pages 4467–9, 2011.

[91] N.J. Shah, A.M. Oros-Peusquens, J. Arrubla, K. Zhang, T. Warbrick, J. Mauler, K. Vahedipour, S. Romanzetti, J. Felder, A. Celik, E. Rota-Kops, H. Iida, K.J. Langen, H. Herzog, and I. Neuner. Advances in multimodal neuroimaging: Hybrid MR-PET and MR-PET-EEG at 3T and 9.4T., Epub ahead of print. *J Magn Reson.*, 2012.

[92] Y. Shao, S. Cherry, K. Farahani, and K. Meadors. Simultaneous PET and MR imaging. *Phys. Med. Biol*, 42:1965–1970.

[93] L. Shepp and Y. Vardi. Maximum Likelihood Reconstruction for Emission Tomography. *IEEE Trans. Med. Imag.*, 1(2):113–122, 1982.

[94] R. Smith and J. Karp. A practical method for random subtraction in volume imaging PET from detector singles countrate measurements. *IEEE Trans. Nucl. Sci.*, 43(3):1981–1987, 2009.

[95] D. Sowby, editor. *Radionuclide Transformations, Energy and Intensity of Emissions, Annals of the IRCP*, volume 13. Pergamon Press Oxford, New York, Frankfurt, 1983.

[96] C. Stearns, D. McDaniel, S. Kohlmyer, P. Arul, B. Geiser, and V. Shanmugam. Random Coincidence Estimation from Single Event Rates on the Discovery ST PET/CT Scanner. *IEEE Nuclear Science Symposium Conference Record*, 2003.

[97] Y. Tai, A. Chatziioannou, M. Dahlbom, and E. Hoffman. Investigation on deadtime characteristics for simultaneous emission-transmission data acquisition in PET. *IEEE Trans. Nucl. Sci.*, (45):2200–2204, 1998.

[98] L. Tellmann, H. Quick, A. Bockisch, H. Herzog, and T. Beyer. The effect of MR surface coils on PET quantification in whole-body PET/MR: results from a pseudo-PET/MR phantom study. *Med Phys.*, (5):2795–2805, 2011.

[99] K. Thielemans, C. Tsoumpas, S. Mustafovic, T. Beisel, P. Aguiar, N. Dikaios, and M. Jacobson. STIR: Software for Tomographic Image Reconstruction Release 2. *Phys. Med. Biol*, 4(57):867–883, 2012.

[100] D. Townsend. Positron Emission Tomography/Computed Tomography. *Semin Nucl Med.*, 38(3):152–166, 2008.

[101] F. van Velden, R. Kloet, B. van Berckel, S. Wolfensberger, A. Lammertsma, and R. Boellaard. Comparison of 3D-OP-OSEM and 3D-FBP reconstruction algorithms for High-Resolution Research Tomograph studies: effects of randoms estimation methods. 2008.

[102] C. Watson. New, Faster, Image-Based Scatter Correction for 3D PET. *IEEE Trans. Nucl. Sci.*, 47:1587–1594, 2000.

[103] C. Watson. Extension of Single Scatter Simulation to Scatter Correction of Time-of-Flight PET. *IEEE Trans. Nucl. Sci.*, 54(5):1679–1686, 2007.

[104] C. Weirich, D. Brenner, J. Scheins, E. Besancon, L. Tellmann, H. Herzog, and N.J. Shah. Analysis and Correction of Count Rate Reduction During Simultaneous MR-PET Measurements With the BrainPET Scanner. *IEEE Trans. Med. Imag.*, 31(7):1372–80, 2012.

[105] C. Weirich, A. Daun, J. Scheins, L. Tellmann, H. Herzog, and N.J. Shah. Long term quantitative stability of the MR compatible BrainPET insert. *Nuclear Science Symposium and Medical Imaging Conference (NSS/MIC)*, pages 3308–3310, 2011.

[106] C. Weirich and H. Herzog. *Neuromethods: Molecular Imaging in the Neurosciences*, chapter Instrumentation and Physical Principles, pages 1 – 22. Springer Science + Business Media, 2012.

[107] C. Weirich, J. Scheins, P. Lohmann, L. Tellmann, L. Byars, C. Michel, E. Rota Kops, D. Brenner, H. Herzog, and N.J. Shah. Quantitative PET imaging with the 3T MR-BrainPET. *Nuclear Instruments and Methods in Physics Research – A*, 702:26 – 28, 2012.

[108] B. Weissler, P. Gebhardt, P. Diippenbecker, A. Salomon, D. Schug, C. Lerche, D. Wirtz, W. Renz, K. Schumacher, B. Zwaans, P. Marsden, F. Kiessling, and V. Schulz. Design concept of worlds first preclinical PET / MR insert with fully digital silicon photomultiplier technology. *IEEE NSS/MIC Conference Record*, pages 2113–6, 2012.

[109] S. Yamamoto, M. Amano, S. Miura, H. Iida, and I. Kanno. Deadtime correction method using random coincidence for PET. *J. Nucl. Med.*, 27(12):1925–8, 1986.

[110] S. Yamamoto, M. Imaizumi, T. Watabe, H. Watabe, Y. Kanai, E. Shimosegawa, and J. Hatazawa. Development of a si-pm-based high-resolution pet system for small animals. *Phys. Med. Biol.*, 55:5817, 2010.

[111] D. Yu and J. Fessler. Mean and variance of single photon counting with deadtime. *Phys. Med. Biol*, 45(7):2043–56, jul 2000.

[112] H. Zaidi and A. Del Guerra. An outlook on future design of hybrid PET/MRI systems. *Medical physics*, 38(10):5667–89, 2011.

[113] P. Zanotti-Fregonara, K. Chen, J. Liow, M. Fujita, and R. Innis. Image-derived input function for brain PET studies: many challenges and few opportunities. *J Cereb Blood Flow Metab.*, 31(10):1986–1998, 2011.

A. Decay Correction for Frames

With the assumption of an ideal scanner without saturation effects, the number of measured counts C is directly proportional to the number of radioactive decays. A correction for radioactive decay during the study has to condider two components. One is the radioactive decay from the start of measurement t_0 to the start of the frame t_a and furthermore, the decay during data acquisition from start of the frame t_a to the end of the frame t_e. The radio activity concentrations given at the respective moments are denoted $a(t)$ and the factor s describes the sensitivity of the scanner. The ideal number of acquired counts within a time frame neglecting radioactive decay is given by

$$C_1 = s\ a(t_0)\ (t_e - t_a) \tag{A.1}$$

The actually measured number of counts in that frame is

$$C_2 = s\ a(t_0) \int_{t_a}^{t_e} e^{-\lambda\tau} d\tau \tag{A.2}$$

The decay correction value α is described by the ratio of C_1 and C_2:

$$\alpha = \frac{C_1}{C_2} = \frac{t_e - t_a}{\int_{t_a}^{t_e} e^{-\lambda\tau} d\tau} \tag{A.3}$$

$$= \frac{t_e - t_a}{-\frac{1}{\lambda}(e^{-\lambda t_e} - e^{-\lambda t_a})} \tag{A.4}$$

$$= \frac{\lambda\ e^{\lambda t_a}\ (t_e - t_a)}{e^{\lambda t_a}\ (e^{-\lambda t_a} - e^{-\lambda t_e})} = \frac{\lambda\ e^{\lambda t_a}\ (t_e - t_a)}{1 - e^{-\lambda(t_e - t_a)}} \tag{A.5}$$

with the framelength $t_e - t_a = \Delta t$:

$$\alpha = \frac{\lambda\ e^{\lambda t_a}\ \Delta t}{1 - e^{-\lambda\ \Delta t}} \tag{A.6}$$

Acronyms

ACF Attenuation Correction Factor

APD Avalanche Photodiode

ASIC Application Specific Integrated Circuit

BF Branching Factor

BGO Bismuth Germinate

CBN Component Based Normalisation

CFD Constant Fraction Discriminator

CLU Crystal Lookup Table

CNR Contrast-to-Noise Ratio

CoV Coefficient of Variance

CSI Chemical Shift Imaging

CT X-ray Computed Tomography

DCF Decay Correction Factor

DCMAP Delayeds Coincidence MAP

DN Direct Normalisation

DTC Deadtime Correction

DTI Diffusion Tensor Imaging

DW Delayed Window

ELU Energy Lookup Table

EPI Echo Planar Imaging

FBP Filtered Backprojection

FDG Flurdesoxyglucose

FET Fluroethyltyrosine

FID Free Induction Decay

FLAIR Fluid Attenuated Inversion Recovery

fMRI functional MRI

FOV Field of View

FWHM Full Width Half Maximum

GM Grey Matter

HRRT High Resolution Research Tomograph

IDIF Image Derived Input Function

LLD Lower Level Discriminator

LOR Line of Response

LSO Lutetium Oxy-Orthosilicate

LYSO Lutetium Yttrium Oxy-Orthosilicate

ML-EM Maximum Likelihood Expectation Maximisation

MP-RAGE Magnetisation Preparation - Rapid Gradient Echo

MR-AC MR-based Attenuation Correction

MRI Magnetic Resonance Imaging

MRS Magnetic Resonance Spectroscopy

NEC Noise Equivalent Countrate

NMR Nuclear Magnetic Resonance

OP Ordinary Poisson

OSEM Ordered Subsets Expectation Maximisation

PCMAP Prompts Coincidence MAP

PET Positron Emission Tomography

PDE Photon Detection Efficiency

PMT Photomultiplier

QC Quality Control

QE Quantum Efficiency

RF Radio Frequency

ROI Region of Interest

SAR Speciffic Absorption Rate

SiPM Silicon Photomultiplier

SNR Signal-to-Noise Ratio

SPECT Single Photon Emission Computed Tomography

SSS Single Scatter Simulation

TAC Time Activity Curve

TCMAP Trues Coincidence MAP

TLU Time Lookup Table

TOF Time of Flight

UHF Ultra High Field

ULD Upper Level Discriminator

UTE Ultra short Echo Time

VRR Variance Reduced Randoms

WB Whole Brain

WM White Matter

XYE X- and Y-coordinate and Energy

Acknowledgements

It would not have been possible to write this thesis without the help and support of many people, to only some of whom it is possible to give particular mention here.
I would like to thank my supervisor, Prof. Dr. N. Jon Shah, for providing me with the opportunity to complete this PhD thesis in his Institute. He has supported me while giving me the scientific freedom to elaborate this work.
My special gratitude is dedicated to Prof. Dr.-Ing. Hans Herzog for the opportunity to work in his group and for his unreserved guidance and generous support and encouragement during my PhD time and for sharing his vast experience and knowledge.
Furthermore, I would like to thank Prof. Dr. Achim Stahl and Prof. Dr.-Ing. Dirk Heberling for their time, their interest and for their willingness to review this thesis.
Special thank is dedicated to Dr. Jürgen Scheins for the helpful discussions and his constuctive criticism and to Lutz Tellmann for assistance in the lab, with the scanners, preparing of experiments and generally for his time. I further appreciate the help and discussions with Dr. Elena Rota Kops and Prof. Dr. Uwe Pietrzyk.
I truely appreciate the support and help and the uncounted mugs of coffee with my past and present fellow students Daniel Brenner, Michaela Gaens, Philipp Lohmann, Liliana Caldeira among a long list of others.
My gratitude also goes to *the Ladies* Conny Frey, Elisabeth Theelen and Suzanne Schaden for help and assistance during phantom studies, filling phantoms and handling the radioactive substances. I also thank Markus Lang and Sebastan Kühn for providing the radioisotopes when ever needed. Besides, the people from the INM-4 have contributed immensely to my personal and professional time in Jülich.
Also the continous support I received from Larry Byars and Christian Michel was always appreciated during my PhD time and during my stay in Knoxville.
During my carreer and during this thesis I am grateful for the time I spent with my friends in Trier, Stuttgart and some other places and for the way they supported me and made me have a great time whenever we met.

My greatest supporter during all this time was Giulia. I appreciate her faithful support and patience so much.
Ganz besonders möchte ich meinen Eltern und meinen Geschwistern danken, die mich stets untersützt und mir die Freiheit gegeben haben meinen Weg zu gehen.